UNIVERSITY OF OKLAHOMA

GRADUATE COLLEGE

MBE GROWTH AND CHARACTERIZATION OF Pb-SALT SEMICONDUCTORS FOR MID-INFRARED DETECTOR AND LASER APPLICATION

A DISSERTATION

SUBMITTED TO THE GRADUATE FACULTY

in partial fulfillment of the requirements for the

Degree of

DOCTOR OF PHILOSOPHY

By

DONGHUI LI
Norman, Oklahoma
2009

Downloaded from SHAREOK. Persistent Handle URL: https://hdl.handle.net/11244/318915

MBE GROWTH AND CHARACTERIZATION OF Pb-SALT SEMICONDUCTORS FOR MID-INFRARED DETECTOR AND LASER APPLICATION

A DISSERTATION APPROVED FOR THE
SCHOOL OF ELECTRICAL AND COMPUTER ENGINEERING

BY

Dr. Zhisheng Shi

Dr. Patrick J. McCann

Dr. James J. Sluss

Dr. Hong Liu

Dr. George B. Richter-Addo

© Copyright by DONGHUI LI 2009
All Rights Reserved.

ACKNOWLEDGEMENTS

First of all, I would like to express my most sincere gratitude to my advisor, Dr Zhisheng Shi, for his valuable guidance, encouragements, technical and financial support throughout this work. I extend heartfelt thanks to Dr. Patrick J. McCann, Dr. James J. Sluss, Dr. Hong Liu and Dr. George B. Richter-Addo for serving on my doctoral advisory committee and for their advice and help.

Secondly, I would also like to acknowledge and thank Dr. Fanghai Zhao, and Dr. Jiangang Ma, for helping in my experiments and their valuable assistance and support. I also thank my other colleagues Shaibal Mukherjee, Binbin Weng, and Guangzhe Yu for their assistance and co-operation during this research work.

Thirdly, I am extremely grateful to Ms. Lynn Hall, the ECE graduate program assistant, for her genuine concern and kindness and to all other ECE faculty, staff, classmates and friends who helped me in numerous ways.

Finally, it is my family to whom I dedicate this work. This work would not have been possible without the continuous support and encouragement of my parents, daughters and wife.

TABLE OF CONTENTS

Title Page……. I
Signature Page……..……...… II
Copyright Page…… III
Acknowledgements...…… IV
Table of Contents…….…. V
List of Tables ……... VIII
List of Figures...……..... IX
Abstract……...……...… XIV

Chapter One: Introduction to Properties and MBE Growth of IV-VI Semiconductors ……..…….. 1
1.1 Introduction to IV-VI Semiconductor…….... 2
1.1.1 General Properties of IV- VI Materials…… 2
1.1.1.1 Bonding and crystal structure…… 3
1.1.1.2 Energy band structure……. 4
1.1.1.3 Band gap engineering……. 9
1.1.1.4 Dielectric properties and refractive indices……. 12
1.2 IV–VI Molecular Beam Epitaxy (MBE)…… 13
1.3 Applications of IV-VI Semiconductors …… 16
1.3.1 Midinfrared Detectors…… 16
1.3.2 Midinfrared Lasers…… 18
1.3.3 Quantum Dots……. 19
1.4 Thesis Overview…….. 21
1.5 References …….. 22

Chapter Two: Growth Pits of Pb-Salt Epilayers Grown on Silicon Substrates……..…….. 27
2.1 Defects in Semiconductors……. 28
2.1.1 Threading Dislocation in IV-VI Materials…… 29

2.1.2 Growth Pits in II-VI Semiconductors…… 33
2.2 Investigation of Growth Pits in IV-VI…… 36
2.2.1 Samples Preparation…….. 36
2.2.2 Composition of Micro-Cuboids……. 38
2.2.3 Multiple Growth Pits……. 39
2.2.4 Origin of Growth pits.....……. 40
2.2.5 Conclusions on Growth Pits……... 41
2.3 References……..... 43

Chapter Three: A Novel In-situ Surface Treatment during MBE Growth of PbSe on CaF_2/Si(111) Heterostructure…….. 45
3.1 Introduction of Surface Treatment on II-VI …….. 46
3.1.1 N-plasma Si Surface Treatment…… 47
3.1.2 Improvement by Surface Treatment…….. 48
3.1.3 Growth Model…… 49
3.2 *In-Situ* Treatment on IV-VI …… 50
3.2.1 Motivation of research…… 50
3.2.2 Traditional growth of Pb-salt on Si…… 50
3.2.3 Design of Experimental Procedure…… 52
3.2.4 *In-situ* Surface Treatment Procedure……. 54
3.2.5 Results and Discussion……. 56
3.2.6 Water-resist …….. 59
3.2.7 Conclusions of *In-situ* Surface Treatment……. 60
3.3 References ……. 61

Chapter Four: Single Element Mid-Infrared PbSnSe Detector on CaF_2/Si (111)..... 63
4.1 Narrow Band-gap Mid-Infrared Photodetectors……..... 64
4.1.1 Introduction of Narrow Gap Detectors……. 64
4.1.2 Theory of Infrared Photodetectors…… 67
4.1.3 IV-VI Photovoltaic Infrared Devices…… 73
4.1.4 Comparison of IV-VI with Other Narrow-gap Detectors……. 73
4.2 PbSnSe Single-element Detectors on Si…… 75

4.2.1 Design and Growth of Detector Structure……. 75
4.3 References…….. 80

Chapter Five: Edge-Emitting Lead Salt Mid-Infrared Laser Structure on BaF_2 [110] Substrate……..….. 82
5.1 Midinfrared diode lasers……..…….. 83
5.2 Lead-Chalcogenide Diode lasers…….. 85
5.2.1 Properties of Lead Salt Diode Lasers…… 85
5.2.2 Application of Pb-Salt Lasers…… 89
5.2.3 Trends of IV-VI Lasers……. 91
5.3 Edge-Emitting Lasers on BaF_2 (110) …… 93
5.3.1 Motivation of This Research……. 94
5.3.2 Experimental Procedure…… 98
5.3.2.1 Substrates preparation…… 98
5.3.2.2 MBE Growth…….. 101
5.3.2.3 Processing after Growth……..… 102
5.3.3 Results and Discussion ……. 104
5.3.4 Summary of Transferring Technology…….. 106
5.4 References……. 106

Chapter Six: Summary and Future Work…… 110
6.1 Summary …… 111
6.2 Recommendations for Future Work …….. 112
6.3 Conclusion ……. 113
6.4 References…….. 113

LIST OF TABLES

Table I: Some properties of IV–VI materials versus MCT…… 16

Table II: Properties of semiconductor materials related to surface treatment at 300.....…… 53

Table III: Some physical properties of narrow gap semiconductors…… 66

Table IV: Some material properties of narrow-gap semiconductors for IR sensor application…….. 66

LIST OF FIGURES

Figure 1.1: The band gap of typical IV-VI materials as a function of the lattice periodicity length (upper abscissa) or of the relative lattice misfit to Si (lower abscissa). For comparison also data for Si, Ge and some III-V and II-VI compounds are shown……. 3

Figure 1.2: Comparison of typical IV-VI and III-V band structures…… 5

Figure 1.3: Constant energy surfaces of PbSe. Aside of the band edge minima at the L-points (open half-ellipsoids), the Σ-pockets are also shown, since they must be considered in connection with hot carriers…..... 5

Figure 1.4: Band structure of PbSe calculated by non-local empirical pseudopotential methods.……..…… 6

Figure 1.5: Refractive index of various III–V, II–VI, IV–VI, group IV semiconductors and selected fluorides and oxides plotted versus lattice constant…….. 13

Figure 2.1: Schematic drawing of the arrangement of the {100} <110> glide system for the NaCl type PbSe (111) layers on Si(111). (a) Perspective drawing; (b) arrangement of possible *a*/2<110>-type Burgers vectors; dashed lines: Burgers vectors which are inclined to the interface and therefore belong to glissile dislocations…… 29

Figure 2.2: Distribution of etch pits on rectangular PbSe (111) islands on Si(111) before (a) and after (b) a thermal cycle to 300 ^{0}C. The crystallographic orientation is plotted pointing into the same directions as in Fig. 2.1……..….. 30

Figure 2.3: Etch-pit density in PbSe (111) on Si(111) vs. thickness *d* of the layers (points). A $1/d^2$ dependence is indicated by the dashed line……. 31

Figure 2.4: (a) Defects which appear to be voids inside hillocks. (b)Defect complexes where the hillocks appear to be associated with void edges……..…… 33

Figure 2.5: Cross-sectional and three dimensional SEM microphotographs of void defects nucleated at various stages of MBE growth: at the growth

interface, (a) in the middle of the growth run, (b) near the end of the growth run…….. 34
Figure 2.6: Cross-sectional SEM microphotograph of void defects which "closed" before the end of the growth. These voids will be completely hidden and not apparent from the top surface…… 35
Figure 2.7: Dislocation etching of a MBE epilayer containing "hidden" voids. (a) Dislocation nests are not apparent on the top surface, (b) but become apparent upon removal of half of the film……. 35
Figure 2.8: Nomarski micrograph of an as-grown PbSe epilayer on Silicon substrate…….. 37
Figure 2.9: SEM image of PbSe epilayer grown on a Si (111) substrate…… 38
Figure 2.10: Plan view of enlarged SEM image of the circled part in Fig. 2.9. 38
Figure 2.11: 60^0 oblique view of enlarged SEM image of the circled part in Fig. 10 ……. 39
Figure 2.12: 3-D of SEM image of Micro-cuboid ……. 39
Figure 2.13: A typical EDXA spectrum of micro-cuboids……. 40
Figure 2.14: SEM image of a ~5 μm growth pit with a 60° oblique view formed by A cluster of single micro-cuboids……. 40
Figure 2.15: Cross-sectional SEM image of a cleaved sample which clearly shows that the "roots" of the micro-cuboid are located near the middle of the epilayer……..…. 41
Figure 2.16: SEM image of crater after the surface was blown by nitrogen gas. 41
Figure 3.1: RHEED patterns of N-plasma treated Si(111) substrate……. 47
Figure 3.2: RHEED patterns of Growth of 8 ML ZnSe on an untreated Si(111) substrate…….…….. 47
Figure 3.3: RHEED patterns of 30 ML of ZnSe grown by conventional MBE directly on an untreated Si(111) substrate……...……. 48
Figure 3.4: Atomic force microscopy images of 30 ML of ZnSe grown by conventional MBE directly on a treated Si substrate…… 48
Figure 3.5: RHEED patterns of 8 ML and (f) 30 ML of ZnSe grown by pulsed MBE on an N-plasma treated Si(111)…… 48
Figure 3.6: 30 ML of ZnSe grown by pulsed MBE on an N-plasma treated Si substrate…… 49

Figure 3.7: Schematic picture of a possible atomic arrangement of the Si surface after the N-plasma treatment……..….. 49
Figure 3.8: Schematic picture of a possible atomic arrangement in the early stages of the ZnSe growth……..…… 49
Figure 3.9: Schematic of layer by layer growth of the in-situ surface treatment. 53
Figure 3.10: RHEED pattern (20 kV) from a clean Si (111) surface at 770°C with the streaky (7x7) surface reconstruction along [112] incidence……..… 54
Figure 3.11: RHEED image in the [112] azimuth (a) during growth of the CaF_2 layer at a temperature of 770^0C and (b) during growth of the SrF_2 layer at a temperature of 530^0C……..…….. 55
Figure 3.12: RHEED image in the [112] azimuth during exposure of the SrF_2 /CaF_2 layer in selenium flux at a temperature of 530^0C…..... 56
Figure 3.13: RHEED image in the [112] azimuth during growth of the PbSe layer at a temperature of 375^0C…… 56
Figure 3.14: Nomarski images of growth pits (a) in traditional growth: 1352 cm^{-2} (size <5μm) and 383 cm^{-2} (size >5μm) and (b) pits in optimized growth: 454cm^{-2} (size <5μm) and 167 cm^{-2} (size >5μm)……..……. 57
Figure 3.15: SEM images of etch pits (a) in traditional growth (PbSe on CaF_2/Si) and (b) in optimized growth (after *in-situ* surface treatment), both in etchant for 5 minuets at 75 ^{0}C……..…… 58
Figure 3.16: Nomarski images of surface: (a) as-grown sample Si38608 (b) Samples Si38608 in DI water for 24 hours……. 59
Figure 4.1: Comparison of the D* of various commercially available infrared detectors when operated at the indicated temperature. Chopping frequency is 1000 Hz for all detectors except the thermopile (10 Hz), thermocouple (10 Hz), thermistor bolometer (10 Hz), Golay cell (10 Hz) and pyroelectric detector (10 Hz). Each detector is assumed to view a hemispherical surround at a temperature of 300 K. Theoretical curves for the background-limited D* for ideal photovoltaic and photoconductive detectors and thermal detectors are also shown…….. 65
Figure 4.2: Schematic of 3-D heterostructure photodetector…… 68

Figure 4.3: Schematic representation of some of the mechanisms by which dark current is generated in a reverse biased p-n junction……..… 71
Figure 4.4: The dependence of the R_oA product on doping concentration for one-sided abrupt HgCdTe, PbSnTe and PbSnSe photodiodes at 77 K (Eg ~ 0.1 eV)……..…. 72
Figure 4.5: schematic of designed PbSnSe infrared detector structure on CaF_2/Si(111)……. 76
Figure 4.6: SEM image of P-N junction after wet etch. The etched surface is comparable to the unetched one…… 76
Figure 4.7: Nomarski images of Etched mesa structures and wire-bonding on P- and N contacts……. 77
Figure 4.8: Nomarski image of comb structure of detector after electroplating of gold for Ohmic contact……. 77
Figure 4.9: Nomarski image of partially enlarged comb structure after gold electroplating (see Fig 4.8)……..…. 78
Figure 4.10: I-V characteristics of P-N junction made by improved PbSe epilayer on CaF_2/Si (111) heterostructure (N-type doped by Bi~2.0 x 10^{18} cm^{-3})……. 78
Figure 4.11: Designed PbSnSe monolithic FPAs on silicon for mid-infrared detection in the future……. 79
Figure 5.1: Schematic illustration of a double-heterostructure semiconductor laser……..… 83
Figure 5.2: Diagram illustrating carrier confinement and waveguiding in a double heterostructure (a) Energy-band diagram at high forward bias; (b) refractive-index distribution; (c) light intensity distribution. *E*c and *E*v: The edges of the conduction and valence bands. *V*: Applied voltage. *d*: Active-layer thickness (~0.1 μm). Γ: Confinement factor……..……. 84
Figure 5.3: Energy band gap of PbSnSe at room temperature……... 86
Figure 5.4: Temperature dependant emission wavelengths of PbSe/PbSrSe QW structures…….…... 87
Figure 5.5: The refractive index of lead-salt materials…… 88
Figure 5.6: The gain curve reaches threshold at a single point as the current is increased from zero. In this position, its half-width is of the

order of the multimode wavelength band width (a few 10 cm^{-1}). The unsaturated gain, which reduced in maximum to a curve touching g_{th} at the mode positions (here symbolized by a flat line), would be much higher than g_{th} (broken line)…… 92
Figure 5.7: Calculated peak gain for [111], [100] and [110] QW structure at different injected carrier concentrations at 300 K. The free carrier absorption (solid line) is shown as well……..…... 95
Figure 5.8: Laser light output per facet versus injection current (L-I) at several heat-sink temperatures. Inset: Laser spectrum at 158 K…… 96
Figure 5.9: SEM image of the surface of unpolished {110} BaF_2 wafer from a commercial vendor…….. 98
Figure 5.10: Nomarski image of substrate surface after 17 min polishing with CMP-I…… 100
Figure 5.11: Nomarski image of polished substrate surface after 25 minutes polishing with CMP-II……. 100
Figure 5.12: SEM image of the substrate surface polished with CMP-II…… 101
Figure 5.13: SEM image of the substrate surface polished with CMP-III…….. 101
Figure 5.14: Schematic of cross-section of copper pattern on the laser structure by electroplating…… 102
Figure 5.15: Schematic of top-view of Cu pattern…….. 102
Figure 5.16: Laser structure with gold and copper electroplating layers and BaF_2 substrate……. 103
Figure 5.17: Final laser structure with passivation and protection layers…… 103
Figure 5.18: RHEED image in the [112] azimuth during growth of the PbSrSe layer at a temperature of 375^0C…… 104
Figure 5.19: Photoluminescence spectra at room temperature of laser sample right after growth, plating copper and removing BaF_2……. 105
Figure 5.20: SEM image of cleaved epilayer with gold and copper support layers……...… 106

ABSTRACT

IV-VI semiconductors grown by molecular beam epitaxy (MBE) on various substrates are extensively attractive for mid-infrared optoelectronic device application. The main goal of this research is to improve device performance by lowering defects densities in the epitaxial layers during MBE growth of Pb-salt materials on a lattice-mismatched substrate. Most of the work is based on MBE growth of monocrystalline PbSe on Si (111) substrates. Details of experiments are described and supported by reflection high-energy electron diffraction (RHEED) patterns. The effect of the *in-situ* surface treatment methods with a motivation of improving electrical and morphological properties of epilayers is demonstrated.

A detailed study on surface morphologies and chemical composition of growth pits and dislocations in PbSe epilayers is provided. Various growth defects are investigated by scanning electron microscopy (SEM) and energy-dispersive x-ray analysis (EDXA). Through a series of experimental studies, it has been confirmed that the vast majority of growth pits within PbSe epilayers contains either single or multiple PbSe microcrystals with a distinct cuboid shape.

Lead salt mid-infrared optoelectronic devices are fabricated on various substrates. Several other research works include: (1) Edge-emitting infrared lasers on BaF_2 (110) substrates. A method of substrate transfer from a BaF_2 substrate to a copper heat-sink is developed. Pulsed photoluminescence (PL) measurements are conducted with help of Fourier transform infrared (FTIR) spectroscopy method during every single step of device processing. (2) Mid-infrared detectors on silicon (111) substrates. Single-element PbSnSe infrared detectors have been made on CaF_2 /Si (111) heterostructures; I-V measurement is accomplished on these detectors.

Key words: Molecular beam epitaxy, Pb-salts, *in-situ* surface treatment, defects, Mid-infrared optoelectronic devices**.**

Chapter One

Introduction to Properties and MBE Growth of IV-VI Semiconductors

1.1 Introduction to IV-VI Semiconductors

IV–VI lead salt semiconductor devices can be traced back to the 1874 when the first rectification was observed with natural galena (PbS) by F. Brann et al.[1]. From that point forward, narrow band gap IV–VI lead salt semiconductors like PbTe, PbSe, and PbS and their ternary and quaternary alloys such as PbSnSe, PbSnTe, PbSrSe, and PbSnSeTe have been widely used in various solid state midinfrared devices, such as light emitting devices (LEDs), laser diodes (LDs), detectors, and thermoelectric generators[2] [3]. Due to their two orders of magnitude lower non-radiative Auger recombination rates as compared to those of III-V and II-VI narrow band gap semiconductors, IV-VI semiconductors optoelectronic devices such as detectors and lasers are considered to be the best candidates for room-temperature operation. Moreover, the high permittivity of lead salt materials will effectively shield electric charges from defects, which in turn yields superior and fault-tolerant devices[4]. IV-VI semiconductors present one of the rare naturally occurring semiconductors and the name "lead salts" for the IV-VI semiconductors is in common use in infrared optoelectronics[5] [6] [7].

1.1.1 General Properties of IV- VI Materials

The binaries PbS, PbTe, and PbSe (ordered by their band gap equivalent wavelengths), and typical mixed crystals of this material family like the ternaries PbSnTe, PbSnSe, PbCdSe, PbSSe cover a band gap range from 50meV to 500meV, with a corresponding wavelength range of roughly 3μm to 30μm. **Fig. 1.1** gives an overview by showing the relation of the band gap of some mixed crystals on the lattice periodicity length. These crystals have rock-salt structure. Ternaries with Eu, Mn, and Gd are of further interest, since they result in semimagnetic materials[8].

Quaternary material is grown for strain and stress engineering. While these materials are the most widely investigated ones due to their possible use in infrared devices, others like SnSe have also been used for early quantum structures[9].

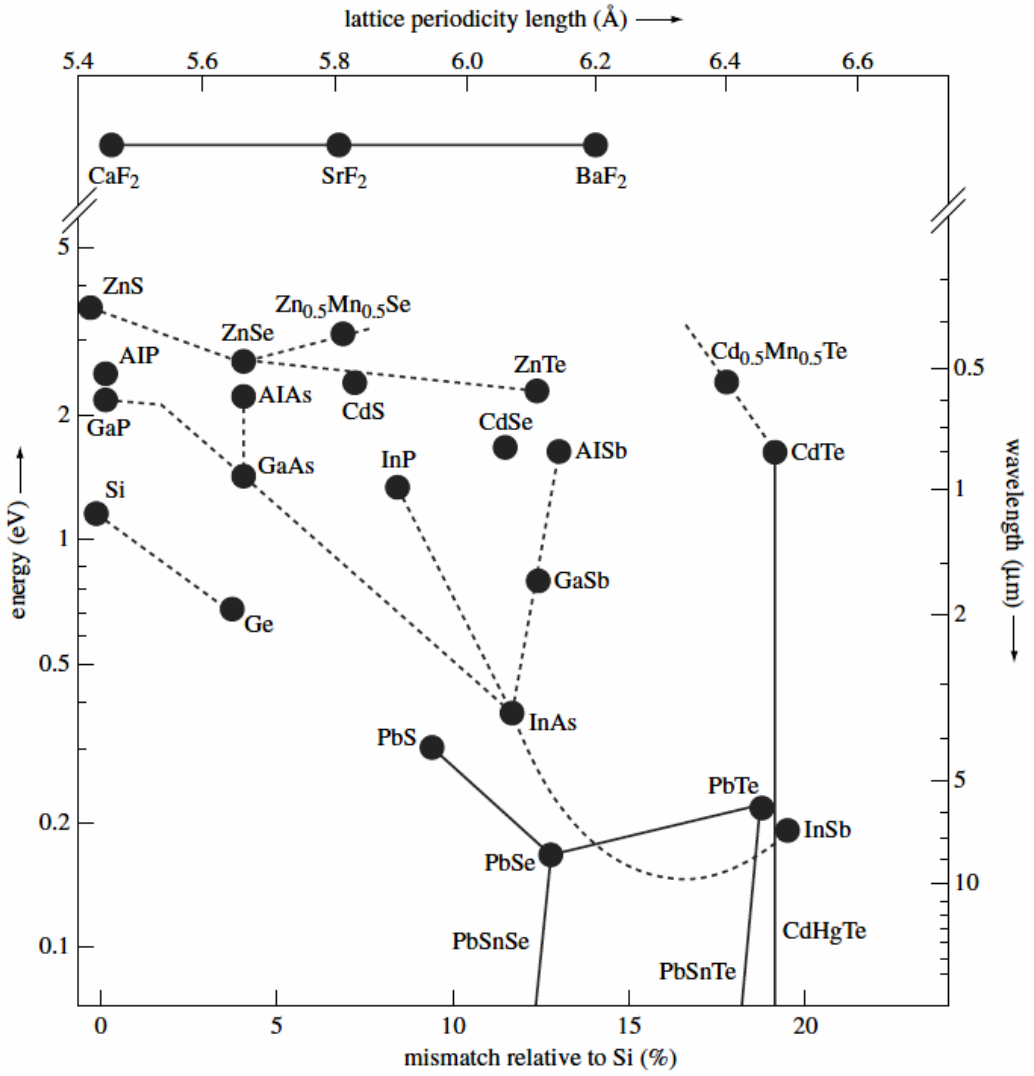

Fig. 1.1 The band gap of typical IV-VI materials as a function of the lattice periodicity length (upper abscissa) or of the relative lattice misfit to Si (lower abscissa). For comparison also data for Si, Ge and some III-V and II-VI compounds are shown. Adapted from Zogg *et al.* (1989)

1.1.1.1 Bonding and crystal structure

In contrast to the tetrahedrally-coordinated group IV semiconductors like diamond, silicon, germanium, and the III–V (GaAs, AlAs, InAs, etc.) or II–VI semiconductors

(ZnTe, CdTe, etc.), in the IV–VI compounds, there are 10 instead of 8 bonding electrons per atom pair. The six electrons per atom pair promote hybridization with the bonds orbitals nearly at 90° angles, resulting in a 6-fold coordination of the atoms in the crystal lattice. As a consequence, the IV–VI compounds predominantly crystallize in the rock-salt structure. As a result, many physical and electronic properties of the IV–VI semiconductors differ strongly from that of the tetrahedrally bonded semiconductors. In addition, the lead salt compounds are mechanically much softer than their tetrahedrally bonded counterparts. This easy plastic deformability has significant implications for device fabrication processes.

1.1.1.2 Energy band structure

The direct band gap minimum of IV-VI semiconductors is fourfold and located at the L-points (on the (111) axes and on the Brillouin zone surface), in contrast to the Γ-point (in the center of the Brillouin zone) minima of the technically more common semiconductors. For comparison, parts of the band structures of PbSe and GaAs are shown in Fig. 1.2. The conduction and valence bands of PbSe are quite similar, so that electrons and holes have comparable masses. These masses, however, differ along the (111) axes and perpendicular to them, giving ellipsoidal energy surfaces for technically relevant carrier concentrations. The order of magnitude of the corresponding mass anisotropies ranges from 10 for PbTe to 1 for PbS. As a typical example, the constant energy surfaces of PbSe are shown in Fig. 1.3 and band structure in Fig. 1.4.

In contrast to the majority of technically important semiconductors, the lead salt band gap widens with temperature. This is explained qualitatively by a structural transition close to zero Kelvin, which “softens” the relevant energies. This fact must

be considered when interpreting experimental optoelectronic data. It leads for instance to absorption of radiation originating from electrically or optically pumped regions embedded in non-pumped material. This is due to the relative blue shift of the active region band gap by localized heating via pumping losses, which pushes the emission energy into band-to-band absorption of the cladding.

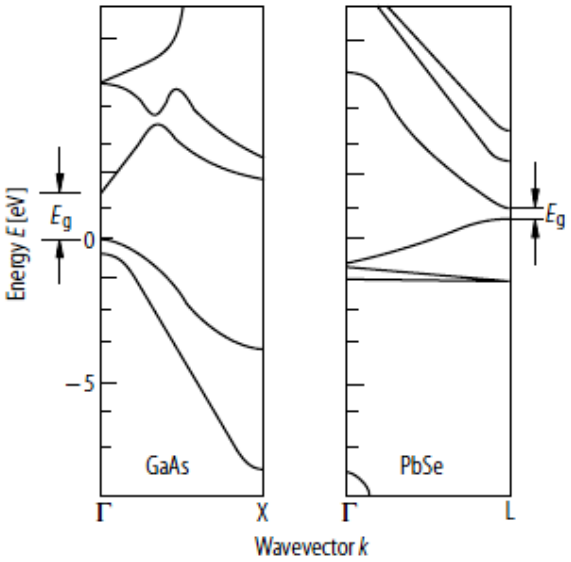

Fig. 1.2 Comparison of typical IV-VI and III-V band structures. From Tacke *et al.*

The wavelength dependence of the refractive index is of typical semiconductor behavior. The refractive index increases with decreasing wavelength within the band gap spectral range with a maximum close to the optical band edge. The temperature behavior corresponds to that of typical semiconductors, but the temperature-induced change is negative relative to the usual, in accordance with the different energy shift of the gap with temperature. The refractive index n is quite high and around $n = 5$, the static dielectric constant is of the order of 1000 giving rise to large depletion lengths. For PbTe and carrier concentrations of the

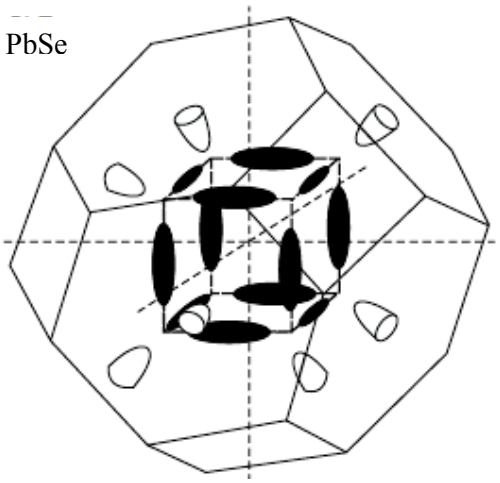

Fig. 1.3 Constant energy surfaces of PbSe. Aside of the band edge minima at the L-points (open half-ellipsoids), the Σ-pockets are also shown, since they must be considered in connection with hot carriers. Adapted From Tacke *et al.*

order of $10^{17}cm^{-3}$, the depletion length exceeds 300nm. These large depletion lengths make the carrier concentrations quite constant across quantum structures. This is an important feature, since it allows comparatively straightforward interpretation of experimental data that depend on carrier concentrations.

Due to the large dielectric response, excitons should have very large Bohr radii

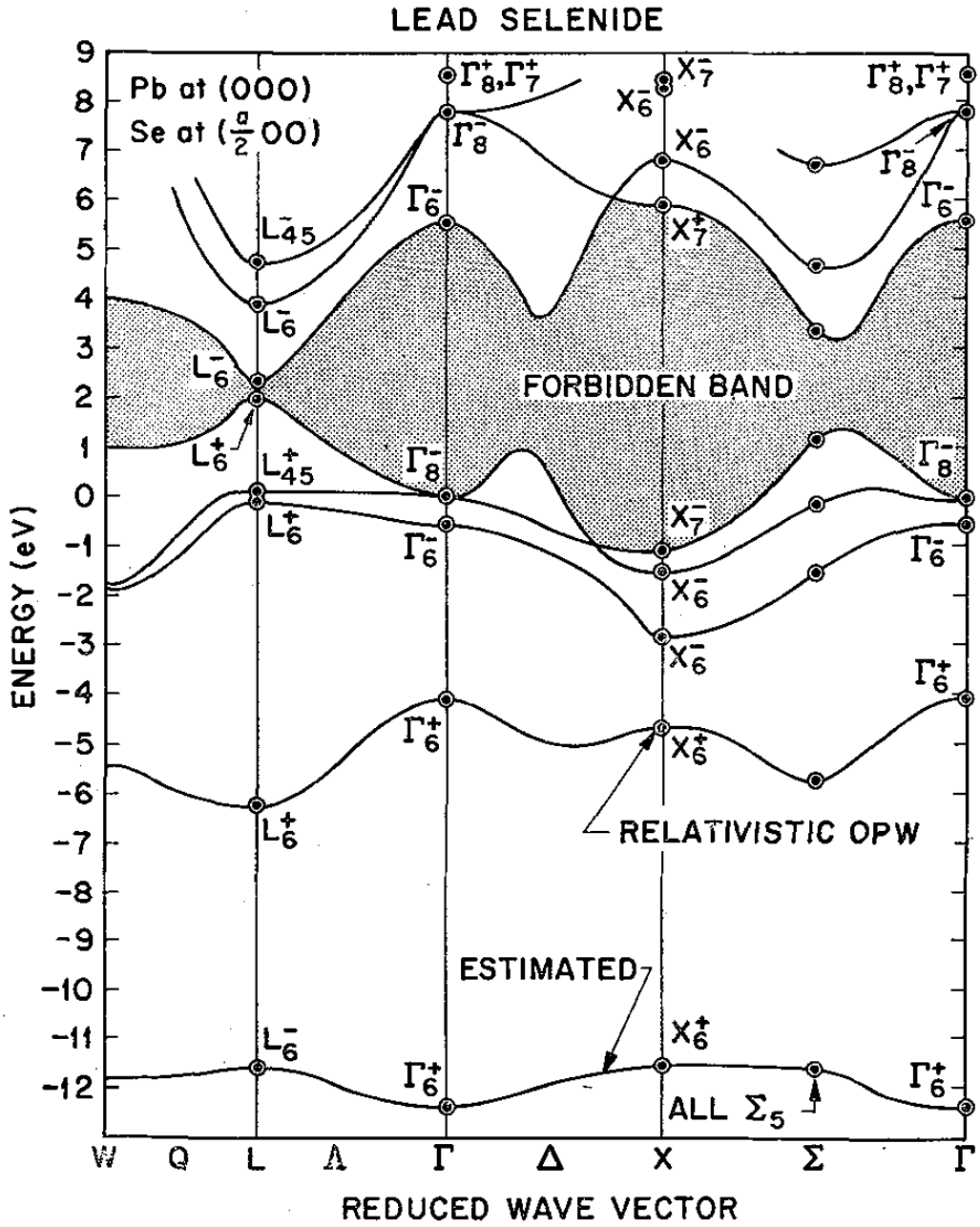

Fig. 1.4 Band structure of PbSe calculated by non-local empirical pseudopotential methods. From online publication.

and very low binding energy; in accordance with this expectation, distinct exciton transitions are not observed directly in this narrow band gap material. There are, however, interpretations of experimental data that are consistent with the existence of such states with binding energies of one to two inverse centimeters, i.e. around 0.1meV[10].

The effective masses of electrons and holes are similar. Due to the four valley structure and electron mass anisotropy, electron effective masses are effective averages of the masses for motion parallel to the minimum rotation ellipsoid axes (m_l) and perpendicular (m_t). While the masses of electrons and holes of the IV-VI compounds are smaller than those of heavy holes of III-V semiconductors, the density of states masses m_d* are comparable, since they are mixed of the transverse and longitudinal masses m_t and m_l by $m_d^* = 4^{2/3}(m_l m_t^2)^{1/3}$ [11].

Since the IV-VI semiconductors are long wavelength infrared materials, free electron absorption in general is strong at wavelengths of interest, with absorption coefficients beyond $10^2 cm^{-1}$ for a material with a carrier concentration of $1x10^{18}cm^{-3}$. Free carrier absorption depends on wavelength, the absorption coefficient α being proportional to the carrier concentration n, the wavelength λ squared, and inversely proportional to the free carrier effective mobility mass m_{eff} and mobility μ or, using the relation between mobility, mass, and scattering time τ with quantum energy $\hbar\omega$ of the photons. From liquid nitrogen to room temperature, the mobility of good grade material is typically not limited by impurities, but rather by optical and acoustical phonon scattering. The reason is qualitatively found in the very high dielectric constant which shields impurities. In this range of temperature T, the mobility empirically follows a power law like $T^{-5/2}$ for pure crystals[12]. Room temperature mobilities are of the order of $1000 cm^2V^{-1}s^{-1}$. Due to the similar band extrema of

electrons and holes, the mobilities of p-type and n-type materials are comparable, the n-type mobility being usually a little larger. The mobility of ternary material is lowered by alloy scattering as usual. However, this effect is sometimes outbalanced by a reduction of the effective mass resulting from the shrinking of the gap. This effect is found notably in the narrow band gap materials $Pb_{1-x}Sn_xSe$ and $Pb_{1-x}Sn_xTe$, that even go through zero band gap due to band inversion. Due to the small mass, mobility increases[13].

The minority carrier lifetime in narrow gap semiconductors is typically limited by the Auger effect. There is a strong difference between IV-VI materials on one side, and on the other side, II-VI and III-V material, in that the Auger recombination rate is two orders of magnitude smaller in the IV-VI material with comparable band gap energy, which is the reason for the IV-VI dominance in mid-infrared diode lasers. This effect was found both theoretically [14] [15] [16] and experimentally[17] [18]. The Auger effect is due to one carrier being excited within a band while two others recombine, one being an electron from the same band, and the other a hole from the valence band. This effect depends on the detailed band structure via energy and momentum conservation. The multi-valley lead salt band structure leads to a special mechanism, intervalley-scattering, where a large momentum is taken up by the intraband transition of the Auger carrier[14] [16]. A pump-probe optical experiment by Klann et al. [17] on PbSe with carrier concentration $3x10^{18}cm^{-3}$ evaluated an Auger coefficient close to $10^{-28}cm^6s^{-1}$, and thus an effective lifetime of $10^{-9}s$, as predicted theoretically[15]. In comparison, Auger recombination coefficients were found to be (at 300K) 60, 210 and 90 in units of $10^{-28}cm^6s^{-1}$, for InAs, $InAs_{0.91}Sb_{0.09}$ and an InAlAsSb multiple quantum well, respectively[19].

Current/voltage characteristics of p-n junctions are usually found to be dominated by carrier generation/recombination characteristics that probably are due to imperfections and/or material impurities. The corresponding non-radiative recombination times of PbSe were 0.7ns for bulk material and 0.45ns for MBE grown material. The defect dominated lifetime is an indicator of a substantial material growth optimization potential[20].

1.1.1.3 Band gap engineering

As stated above, a main property of the electronic band structure of the lead salt compounds (PbSe, PbTe, PbS), representing the technologically most important IV–VI materials, is their small and direct energy gap of less than 410 meV at the L-point of the Brillouin zone (see Fig. 1.1 and Fig. 1.4). As a result, photons can be directly absorbed or emitted at the band edges. The conduction and valence bands are nearly mirror symmetric with almost equal effective masses for the electrons and holes. Because of the narrow energy gaps, the energy bands are strongly non-parabolic and the effective masses of electrons as well as holes are rather small ($0.02m_0$–$0.08m_0$ for the transverse masses). In addition, the bands are anisotropic, i.e., the Fermi surfaces are elongated ellipsoids of revolution around the <111> axes, characterized by a longitudinal and transverse effective mass m^l and m^t parallel and perpendicular to the 8-fold <111> directions. While for most semiconductors the energy band gap increases with decreasing temperature, in the lead salt compounds it decreases upon cooling to from room temperature to 4 K by about 150 meV. This represents a large relative change with respect to the absolute value of the band gap, and thus, the emission of lead salt based diode lasers can be tuned of over a broad wavelength

range just by changing of operation temperature. This effect is used for spectroscopic applications of these lasers.

For adjustment of the fundamental absorption edge of infrared detectors as well as the adjustment of the emission wavelength of lead salt diode lasers, alloying of the lead salt compounds with other chalcogenide compounds is used [21] [22] [23]. This is shown in Fig. 1.1, where the band gap energies of several IV–VI compounds and their alloys are plotted versus lattice constant and compared with various III–V, II–VI and group IV semiconductors. Band gap engineering is also a crucial prerequisite for fabrication of quantum confined low dimensional heterostructures. This is based on the alloying of different semiconductor materials by which the energy band gap of the material can be varied over a wide range. For the IV–VI semiconductors, a number of different ternary and quaternary alloys have been used for this purpose. Of the classical alloys within the IV–VI compounds, the ternary PbSnTe and PbSnSe single phase pseudo binary alloys have been widely used for far infrared applications up to wavelengths of 30 μm (see Fig. 1.1). Since the conduction and valence bands in the tin chalcogenides are exchanged compared to the lead chalcogenides, the band gap of the ternary alloy decreases linearly with increasing Sn content reaching zero for a certain alloy composition. Other pseudo binary IV–VI alloys with exchanged group IV (e.g. Pb/Ge) or group VI element (e.g. Se/Te) are less useful for band gap engineering since the achievable variations of the band gap energies are comparatively small, while the lattice constants change rather strongly with varying alloy composition. For these alloys, the largest tuning range can be achieved in the $PbSe_{1-y}S_y$ system with a band gap variation from 172–310 meV at 77 K. Since other IV–VI compounds such as SnS, GeTe or GeSe do not crystallize in the rock-salt crystal structure, only a limited miscibility regime exists for their alloys with the lead

salt compounds. The same applies also for alloys with MnTe or CdTe. Only $Pb_{1-x}Cd_xS$ exhibits a relatively wide miscibility region and shorter wavelength IV–VI diode lasers have been fabricated in this alloy system.

In order to obtain higher band gap materials, alloys of the lead salts with rare earth mono-chalcogenides (EuTe, EuSe, EuS, YbTe, SmTe, etc.) or alkaline earth chalcogenides (SrTe, SrSe, SrS, BaTe, BaS, CaTe, CaS) have been used [23 24 25]. These compounds share the same rock-salt crystal structure as the lead salt compounds. Of the rare earth mono-chalcogenides most are metallic, with the exception of those with the divalent rare earth elements Eu, Yb, Sm and Tm. The corresponding highly ionic mono-chalcogenides are semiconductors with energy band gaps in the 1–2 eV range. The Eu chalcogenides are the ones with most stable rare earth ion in the 2^+ state due to the half filled 4f shell. Thus, a complete miscibility exists for the $Pb_{1-x}Eu_xX$ systems (X stands for Te, Se, S), resulting in a large band gap tunability of more than 1.5 eV. The lattice constants as well as energy band gaps of the $Pb_{1-x}Eu_xX$ alloys depend nonlinearly on Eu content. For Eu contents below about 10%, the change in energy band gap is very large, with dEg/dx = 3.5, 3.0 and 5 eV for $Pb_{1-x}Eu_xTe$, $Pb_{1-x}Eu_xSe$ and $Pb_{1-x}Eu_xS$, respectively, with little changes in the lattice constants. Consequently, $Pb_{1-x}Eu_xX$ alloys have been the most widely used high energy band gap alloys for lead salt based heterostructures and devices [23 24].

The alternative group of materials for high energy band gap alloys are the alkaline-earth chalcogenides. These compounds such as CaX and SrX have energy band gaps above 4eV and lattice constants comparable to that of the lead salt compounds. For the alloys $Pb_{1-x}Ca_xS$ and $Pb_{1-x}Sr_xS$, a complete miscibility exists, and for $Pb_{1-x}Ca_xTe$, $Pb_{1-x}Sr_x$ Te and $Pb_{1-x}Sr_x$ Se solid solutions have been obtained for Sr or Ca mole fractions at least up to 15%[25]. For other alloys with alkaline-earth

chalcogenides such as BaTe or MgTe, only a very small solubility region exists. In the lead/alkaline earth chalcogenide alloys again the energy band gap increases very rapidly with alkaline earth content with little change in the lattice constants. This makes these alloys equally well suited for fabrication of lead salt based quantum well structures and MIR diode lasers[13].

One general problem associated with the high energy band gap lead salt alloys is the very rapid deterioration of the electrical properties of the epitaxial layers with increasing rare-earth or alkaline-earth content [23 24 25]. In fact, for all of these alloys a decrease of the low temperature electron mobility by more than two orders of magnitude has been observed already for alloy compositions of only 10%. This has been explained by very strong alloy scattering of the charged carriers[24], which can even lead to a disorder-induced metal to insulator transition.

1.1.1.4 Dielectric properties and refractive indices

An important property of the lead salt compounds is their huge static dielectric constant. This results from the fact that these materials, in particular PbTe, are close to a structural phase transition from the cubic to a rhombohedral phase that exhibits obvious ferroelectric properties. Thus, although PbTe remains cubic at all temperatures, the temperature dependence of the static dielectric constant $\varepsilon_0 \propto C/(T-\theta)$ can be associated with an extrapolated negative Curie temperature θ of –75 K. As a consequence, the static dielectric constant increases strongly with decreasing temperature, reaching a value of $\varepsilon_0 = 1350$ at 4 K. The dielectric constants of the lead compounds in the mid-infrared spectral region are also exceptionally large, causing a refractive index above 5 for PbSe and PbTe (see Fig. 1.5). By combining the lead salt compounds with wide band gap and low refractive index materials such as EuTe,

EuSe, SrSe or BaF_2 (see Fig. 1.5), very high reflectivity epitaxial Bragg interference mirrors, as required in vertical cavity surface emitting lasers (VCSELs), can be obtained [25]. The refractive index contrast achieved by combining the lead salt compounds with these materials is up to five times larger as compared to those of III–V materials (see Fig. 1.5). As a result, the optical quality of lead salt based Bragg mirrors is significantly better than those of other materials[26].

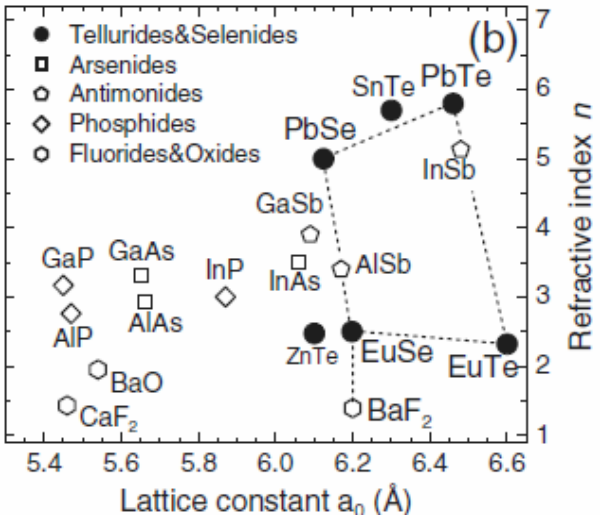

Fig. 1.5 refractive index of various III–V, II–VI, IV–VI, group IV semiconductors and selected fluorides and oxides plotted versus lattice constants. Taken from Schwarzl *et al.*

1.2 IV–VI Molecular Beam Epitaxy (MBE)

Molecular beam epitaxy (MBE) of IV–VI semiconductors has been used for fabrication of low dimensional structures such as quantum wells and superlattices as well as infrared optoelectronic devices. In 1964, the first mid-infrared p–n junction laser was made by Butler et al. [27] using $Pb_{1-x}Sn_xTe$, and since then, efficient mid- and far-infrared IV–VI compound diode lasers have been fabricated, finding their main applications for remote sensing of gaseous pollutants in trace gas sensing devices, toxic gas analysis systems, human breath analysis in medical diagnostics and industrial process control. Recent progress in epitaxial growth techniques has led to the fabrication of lead salt midinfrared diode lasers operating at temperatures up to 225 K in continuous (cw) mode [28] and up to 60 °C in pulsed mode[29]. In fact, lead salt

IV–VI compound diode lasers can cover the whole 3–30 μm wavelength region and feature the highest operation temperature of conventional infrared band gap lasers. Apart from this, IV–VI MBE has also been used for the fabrication of detector arrays on Si substrates [2] and of novel thermoelectric devices[30]. In addition, MBE has been extensively used for the growth of low dimensional electronic and magnetic systems like quantum wells[31], superlattices [32]and self-organized quantum dots[33].

In contrast to other compound semiconductors, the main constituents in IV–VI MBE are supplied from compound effusion sources loaded with PbSe, PbTe, PbS, SnTe, SnSe or GeTe, etc. This is due to the fact that the IV–VI compounds evaporate predominantly in the form of binary molecules, which means that nearly congruent evaporation occurs. While the degree of dissociation is only few percent for lead salt compounds, it notably increases for the tin and germanium chalcogenides. Therefore, additional group VI flux is usually used to assure the right stoichiometry of the epilayers, but only a very small excess group VI is required. By changing the total group IV to group VI flux ratio, the background carrier concentration and type of carriers can be controlled flexibly.

Excess group IV flux leads to n-type and excess group VI flux to p-type conductivity in the epilayers. For the high energy band gap alloys required for band gap engineering, the group IV elements are substituted by rare earth (Eu, Yb) or alkaline earth elements (Sr, Ca). Due to the very low vapor pressure of their chalcogenide compounds, these elements are supplied from elemental sources, which must be complemented by the corresponding amount of excess group VI flux. Dopants such as Bi, Tl or Ag can be supplied either from elemental or compound (e.g., Bi_2Se_3, Bi_2Te_3 or Tl_2Te) sources. Generally, effusion temperatures for the IV–VI compounds are in the range of 400 to 600 °C, for the group VI elements (Te, Se) in

the range of 150–300 °C and for the rare earth and alkaline earths around 450 to 900 °C. The substrate temperatures are typically in the range of 250 °C to 400 °C, where a unity sticking coefficient of all components except for Te, Se or S exists. Above 400 °C a significant reevaporation from the lead salt layers occurs and the growth rates and layer composition become increasingly difficult to control. 2D layer-by-layer growth can be achieved down to temperatures as low as 150 °C, as proven by *in situ* RHEED studies in which pronounced RHEED intensity oscillations were found over a large temperature range[22 23].

Concerning the substrate materials for lead salt epitaxial growth, not only the lattice mismatch to common semiconductor substrates such as Si or GaAs is rather large (10% and more, see Fig. 1.1), but also the crystal structure and even more the thermal expansion coefficient β of the IV–VI compounds of around 20×10^{-6}/K differ strongly from that of Si as well as that of the zinc-blende type III–V or II–VI compounds (β typically less than 6×10^{-6}/K) [36 37]. As a consequence, large thermal strains are induced in the epitaxial layers during cooling of the samples to room temperature and below after sample growth. For thicker epilayers, this leads to a significant structural degradation of epilayers or even to the formation of cracks and peeling during thermal cycling [36 37]. A best compromise in these respects is achieved for BaF_2 substrates, in spite of its different crystal structure (calcium fluoride structure). As shown in Fig. 1.1, BaF_2 shows only a moderate lattice-mismatch to PbSe or PbTe (– 1.2% and + 4.2%, respectively) and moreover, the thermal expansion coefficient is almost exactly matched to that of the lead salt compounds. Therefore, the epilayers are stable against thermal cycling. Furthermore BaF_2 is highly insulating and optically transparent in the mid-infrared region. Thus, BaF_2 has been the most widely used substrate material for the IV–VI epitaxial growth. Due to its high ionic

character, good BaF_2 surfaces can be obtained easily only for the (111) surface orientation. Therefore, in most cases, IV–VI heterostructures have been grown in this surface orientation. However the problems still exist regarding to the BaF_2 substrates, such as low thermal conductivity, hard to cleave along (110) or (100) orientation etc.

1.3 Applications of IV-VI Semiconductors

1.3.1 Midinfrared Detectors

Narrow-gap lead chalcogenides (IV–VI compounds) such as $Pb_{1-x}Sn_xTe$ or $Pb_{1-x}Sn_xSe$ have been known for a long time and were employed as early as the 1970s to fabricate infrared detector arrays for thermal imaging.[34] They can cover the infrared (IR) range from <3 μm to >30 μm by choosing appropriate chemical compositions. The properties of IV–VI materials are remarkably different from the well-known II–VI or III–V compounds (see Table I). The ultimate sensitivities obtainable with IV–VI compounds are similar to those of II–VI narrow bandgap semiconductors such as $Cd_{1-x}Hg_xTe$ (MCT) under similar conditions (i.e., bandgap and operating temperature). They are limited by Auger recombination in both cases (see Table I). This leads to

	IV–VI	II–VI
MWIR 3 μm to 5.5 μm	PbTe, PbSe, $Pb_{1-x}Z_xSe$, $Pb_{1-x}Z_xTe$ Z = Eu, Sr	$Hg_{1-x}Cd_xTe$ (MCT)
LWIR 8 μm to 12 μm	$Pb_{1-x}Sn_xSe$ (LTS), $Pb_{1-x}Sn_xTe$ (LTT)	$Hg_{1-x}Cd_xTe$ (MCT)
Structure	NaCl (ionic/covalent)	Zincblende (covalent)
Direct bandgap	L-point	Γ-point
Effective masses	$m_e \approx m_h$, $\mu_e \approx \mu_h$	$m_e < m_h$, $\mu_e > \mu_h$
Dep. E_g with x: (77 K)	LTS: x = 0…~0.2, 0.18–0 eV LTT: x = 0…~0.4, 0.22–0 eV	MCT: x = 1–0.13, 1.6–0 eV
	PbSe, PbTe already narrow gap → *less Δx dependence*	CdTe not narrow gap *High Δx dependence*
Permittivity ε	Very high: PbTe~480 (RT) PbSe~200 (RT) → Electric field of defects efficiently shielded → *Tolerant to defects*	~20
Homogeneity region	$Me_{1-\delta}X_{1+\delta}$ → *p*-type $Me_{1+\delta}X_{1-\delta}$ → *n*-type $n, p > 10^{17}$ cm^{-3}	much smaller n, p possible
IR sensors (single-cryst. mat.)	PV photovoltaic only (*high n, p*)	PV photovoltaic *or* PC photoconductive
Max. R_oA (0.1 eV, 77 K)	LTT~12 Ω cm^2 LTS~15 Ω cm^2	~11 Ω cm^2
Thermal expansion	~20×10^{-6} (K)	~5×10^{-6} (K)
Main glide planes of dislocations	{100}	{111}

Table I. Some Properties of IV–VI Materials versus MCT

maximal R_oA (differential resistance at zero bias times area) products over a certain doping concentration: e.g., optimal concentrations for 0.1 eV bandgap devices at 80 K are ~2 $\times 10^{14}$ cm^{-3} to ~5 $\times 10^{15}$ cm^{-3} for MCT and ~1 $\times 10^{17}$ cm^{-3} to ~3 $\times 10^{17}$ cm^{-3} for $Pb_{1-x}Sn_xTe$ or $Pb_{1-x}Sn_xSe$. The much higher optimal concentrations in $Pb_{1-x}Sn_xTe$ and $Pb_{1-x}Sn_xSe$ are due to the larger homogeneity region and high permittivities in these materials. These high permittivities, as well as the high thermal expansion coefficients (7 times higher than Si), were one reason why development for IR focal-plane array (FPA) thermal imaging was nearly stopped in the early 1980s in favor of MCT. However, IV–VI materials remained the only choice to fabricate mid-wave infrared (MWIR) laser diodes before the invention of the quantum cascade laser, [35] and continue to be of importance today.

Renewed interest started in the mid-1980s with the growth of IV–VI epitaxial layers on non-latticematched substrates such as Si. High-quality layers were obtained by molecular-beam epitaxy (MBE) on Si(111) substrates with a very thin CaF_2 buffer layer for compatibility. Of most importance is the relief of the thermal mismatch strain by glide of dislocations: the dislocations glide on {100} planes, which are inclined with respect to the (111) surface plane, i.e., the Schmid factors and therefore the shear strains are not zero. On each temperature change, the threading ends of the misfit dislocations glide to remove the mechanical thermal strain built up. They never block (as might occur in zincblende type II–VI and III–V semiconductors) and in addition may even react to decrease the density of threading dislocations and therefore increase the structural layer quality.[36] Linear IV–VI IR sensor arrays on Si(111) were demonstrated with cut-off wavelength ranging from ~3 μm to ~15 μm.[4] A two dimensional (2D) FPA with the IV–VI layer grown epitaxially on an active Si chip containing the readout multiplexing electronics was also demonstrated, proving the

concept that whole IR FPAs might be fabricated by post-processing of complete and tested Si-complementary metal oxide semiconductor (Si-CMOS) circuits.[37]

1.3.2 Midinfrared Lasers

Lead salt semiconductor diode lasers [13] [28] have been widely used for high-resolution gas spectroscopy [38] due to the numerous absorption lines of almost all molecular gases in the MIR spectral region. Due to their large wavelength tunability and their narrow line widths, lead salt lasers have been an excellent tool for gas sensing applications. In mid-infrared vertical cavity surface emitting lasers (VCSELs), the laser resonator is created by epitaxial growth of planar Bragg interference mirrors. Therefore, the laser light is coupled out perpendicular to the epilayer surface. VCSELs offer a variety of advantages such as a small beam divergence, large mode spacing and single mode operation and the possibility of monolithic integration, and they have a great potential for reducing threshold currents and increasing the operation temperatures.

Lead salt mid-infrared VCSELs were first demonstrated by G. Springholz's research group [39] for wavelengths between 4.5 and 6 μm. This development was based on the realization of novel high-reflectivity epitaxial Bragg mirrors and ultra-high finesse microcavity structures for the infrared region [44]. These mirrors consist of multilayer stacks of optically transparent dielectric layers with alternating low and high refractive index and an optical thickness equal to one quarter of the target wavelength λ_T for which the reflectivity is maximized. The high reflectivity is purely caused by multiple-interference effects and can be arbitrarily tuned from 0 to 100% just by changing the layer sequence and/or number of layer pairs. Due to the quite short length of the active region of around 1 μm of VCSELs compared to several

hundreds μm for edge emitters, the reflectivity of the cavity mirrors must be very high, i.e., typically above 98%. This can be only achieved either by using a large number of λ/4 layer pairs or by combining materials with very large refractive index contrast. As shown in Fig. 1.1, the combination of lead salt materials (with high refractive index) (n ~ 5) with wide band gap materials such as EuTe, EuSe or BaF_2 with n ~ 2.5 to 1.5 clearly fulfills this requirement. Due to the resulting very high refractive index contrast Δn / n of up to 100%, ultra-high reflectivity Bragg mirrors with reflectivity above 99.5% can be achieved already with 3 layer pairs [27], in great contrast to the case of III–V Bragg mirrors, which require typically around 20 periods because the achievable refractive index contrasts are only around 15%. In addition, these materials are epitaxially compatible with the lead salt compounds, featuring lattice constants and thermal expansion coefficients that fit reasonable well to that of the lead salt compounds. Due to the very high refractive index contrast, lead salt Bragg mirrors exhibit ultra-broad high-reflectivity stop band regions with a spectral width of up to 80 % of the central mirror wavelength. This makes them highly suitable also for passive optical elements such as low loss omni-directional mirrors and interference filters[40].

1.3.3 Quantum Dots

Strained-layer heteroepitaxy has become a powerful tool for fabrication of self-assembled semiconductor nanostructures[41 42]. It is based on the natural tendency of highly strained layers to spontaneously form coherent, i.e., dislocation free three-dimensional (3D) nanoislands on the surface of a thin 2D wetting layer[43]. This islanding is driven by the highly efficient strain relaxation possible within the islands due to lateral elastic expansion or compression in the directions of their free side

faces[44]. For islands larger than a certain critical size, such relaxed elastic energy outweighs the corresponding increase in free surface energy, leading to an effective lowering of the total free energy of the system. Overgrowth of these islands with a higher band gap barrier material results in a confinement of the free carriers in all three directions of space and thus, self-assembled quantum dots are formed. Due to the statistical nature of growth, however, these dots exhibit considerable variations in size and shape. This results in a large inhomogeneous broadening of the quantum confined energy levels and the corresponding optical transitions[45].

In addition, there is little control over the lateral arrangement and position of the nanoislands. Both factors pose considerable limitations for device applications. Three-dimensional stacking of self-assembled quantum dots in multilayer or superlattice structures provides an effective tool for controlling the vertical and lateral arrangement of the dots. PbSe/PbEuTe quantum dot superlattices represent a particular interesting system for investigation of such interlayer correlations. On the one hand, the elastic anisotropy is particularly large and therefore, an exceedingly efficient vertical and lateral ordering takes place. On the other hand, different dot stacking types occur for different spacer thicknesses as well as growth conditions. Therefore, this system is very well suited for testing of various theoretical predictions of superlattice growth models. In addition, comprehensive systematic studies on interlayer correlation mechanisms have been carried out in this material system[46 47].

Quantum dots can be made by self-organized growth from quantum-well structures, and also by photolithographic techniques. Due to the possibility to grow adjacent layers of quite different lattice constant in the IV-VI material family, strain can well be incorporated into superlattice structures. The inherent strain can be designed and predetermined by selection of the material composition and layer

thickness. The first reported self-organized quantum-dot structure was made by MBE from $Pb_{1-x}Eu_xTe$ (x = 0.05 to 0.1) spacers and PbSe wells, with some 5.5% lattice mismatch[35]. Growth resulted in PbSe islands that were embedded by consecutive spacers. While these islands appeared at irregular positions in the first PbSe layer, they got organized in subsequent periods, resulting in a face centered cubic (FCC) superstructure of the single dots localized in the wells. The lattice constant of the resulting dot crystal was shown to be variable and determined by changing the superlattice period. The comparative ease of making these quantum-dot crystals bears considerable potential for optoelectronic device applications.

1.4 Thesis Overview

The main goal of this research is to improve the Pb-salt materials quality for midinfrared detector and laser application. In order to achieve such goal, proper design of a procedure of MBE growth and fabrication of laser and detector structure on various substrates are needed that would preferentially make the device to operate in high performance such as high temperature, high sensitivity, etc. Chapter one introduces the basic properties of the IV-VI semiconductors and their applications in various fields. Chapter two discusses the growth defects in the Pb-slat epilayers such as growth pits and etch pits. The growth pits in Pb-salts semiconductors are studied thoroughly in shape, size and density since the threading dislocations have been studied by the other researchers previously. Normaski and Scanning Electron Microscopy (SEM) images are provided to verify the properties of the growth pits in IV-VI semiconductors in order to deeply understand the origin of the growth defects. Chapter three describes the *in-situ* surface treatment method, which is carried out during MBE-grown PbSe on CaF_2/Si (111) heterostructure. The details of the experimental procedures are given step by step and supported by in-situ RHEED patterns. The promising results are listed in form of the

enhanced electrical and optical performance of the Pb-salt epilayers. Chapter four discusses fabrication and characterization of a single element Pb(Sn)Se mid-infrared detector grown on Si(111) substrate. The details of the growth and processing are addressed based on detector structure, doping, etching, Ohmic contact, etc. I-V curves from the P-N junctions are provided to verify the performance and properties of the P-N junction and the issues related to the performance and fabrication of the detector are addressed too. Chapter five presents the fabrication of an edge emitting Mid-IR laser structure grown on a polished (110)-oriented BaF_2 substrate. The details of fabricating procedures are addressed and fabrication issues have been discussed according to the intensity and linewidth of the photoluminescence (PL). By using electroplating technique, a metal base is formed in contact with epitaxial layer and is followed by a growth substrate removal for complete transfer of the epitaxial layer to a metal membrane. Chapter six details the future direction for this project and explains the issues needing further investigation and improvements.

Some material properties and outcomes thereafter were still not clearly understood. Therefore, some questions remain unanswered. Despite these, many novel processes have been already developed and many challenges were overcome in an honest effort towards betterment. Hopefully this dissertation provides a clear picture of the field in Pb-salt semiconductor materials and devices and therefore inspires a continuation of this work at the University of Oklahoma.

1.5 References

[1] F. Braun, "Ueber die Stromleitung durch Schwefelmetalle ("On Current Flow through Metallic Sulfides"), *Annalen der Physik und Chemie* **153**, 556 (1874).

[2] H. Zogg, A. Fach, C. Maissen, J. Masek and S. Blunier. *Optical Eng.* **34,** 1964 (1995).

[3] L.D. Hicks, T.C. Harman, X. Sun, and M.S. Dresselhaus, *Phys. Rev.* B **53**, R10493 (1996).

[4] H. Zogg, S. Blunier, T. Hoshino,C. Maissen, J. Masek, A. N. Tiwari, *IEEE Trans. Electron Devices* **38**, 1110 (1991).

[5] Katzir, A., Rosman, R., Shani, Y., Bachem, K. H., Böttner, H., Preier, H.M.: Tunable lead salt lasers, in: Handbook of solid state lasers, Peter K. Cheo (ed.), Marcel Dekker, New York, Basel (1989)

[6] Bauer, G., Kriechbaum, M., Shi, Z., Tacke, M., *J. Nonlin. Opt. Phys. Mater*. **4,** 283 (1995).

[7] M. Tacke, Lead Salt Lasers, in: Long wavelength infrared emitters based on quantum wells and superlattices, Helm, M. (ed.), Optoelectronic properties of semiconductors and superlattices, Gordon & Breach Science Publishers SA, Amsterdam (2000).

[8] Bauer, G., Pascher, H. in: Semimagnetic semiconductors and diluted magnetic semiconductors, M. Averous, M. Balkanski (eds)., Plenum Press, New York (1991), p. 209-236.

[9] Bauer, G., Pascher, H., Kriechbaum, M, *Physica Scripta* T **19** 147 (1987).

[10] Ishida, A., Fujiyasu, H.: *Jpn J. Appl. Phys*. **24,** L956 (1985).

[11] Landolt-Börnstein, New Series, Group III, Vol **17**: Semiconductors, O. Madelung, M. Schulz, H. Weiss (eds.), Springer, Berlin, Heidelberg, New York. For IV-VI compounds see Subvol. III/17f (1983).

[12] Nimtz, G., Schlicht, B.: Narrow gap lead salts, *Springer Tracts Mod. Phys.,* Vol. **98,** Springer, Berlin (1983).

[13] M. Tacke, *Infrared Phys. Technol*. **36**, 447 (1995).

M. Tacke, in: Long Wavelength Infrared Emitters based on Quantum Wells and Superlattices, edited by M. Helm (Gordon and Breach Science Publishers, Amsterdam, 2000), pp. 347–396.

[14] Ziep, O., Genzow, D., Mocker, M., Herrmann, K. H.: *Phys. Status Solidi* (b) **99,** 129 (1980).

[15] Mocker, M., Ziep, O.: *Phys. Status Solidi* (b) **115,** 415 (1983).

[16] Rosman, R., Katzir, A.: *IEEE J. Quantum Electron*. **18,** 814 (1982).

[17] Klann, R., Buhleier, R., Elsaesser, T., Lambrecht, A.: *Appl. Phys. Lett*. **59,** 885 (1991).

[18] Findlay, P. , Pidgeon, C.R., Murdin, B.N., van der Meer, A.F.G., Langerak, C.J.G.M., Ciesla, C.M., Oswald, J., Springholz, G., Bauer, G.: *Phys. Rev.* B **58,** 12908 (1998).

[19] Lindle, J.R., Meyer, J.R., Hoffman, C.A., Bartoli, F.J., Turner, G.W., Choi, H.K.: *Appl. Phys. Lett.* **67,** 3153 (1995).

[20] Xu, J., Tacke, M.: *Infrared Phys*. **33,** 151 (1992).

[21] D. L. Partin and J. Heremans, in: Handbook on Semiconductors, edited by T.S. Moss and S. Mahajan, Vol. 3A (North-Holland, Amsterdam, 1994), pp. 369–450.

[22] G. Springholz, in: Lead chalcogenides – Physics and Applications, edited by D. Khoklov (Taylor and Francis Inc., 2003), p. 123.

[23] G. Springholz, H. Zogg, and Z. Shi, in: Thin Films: Heteroepitaxial Systems, edited by W. K. Liu and M. B. Santos (World Scientific, Singapore, 1999), pp. 621–688.

[24] A. Prinz, G. Brunthaler, Y. Ueta, G. Springholz, G. Bauer, G. Grabecki, and T. Dietl, *Phys. Rev.* B **59**, 12983 (1999).

[25] G. Springholz, T. Schwarzl, and W. Heiss, in: Mid-infrared Semiconductor Optoelectronics, edited by A. Krier (Springer Verlag, 2006).

[26] T. Schwarzl, W. Heiss, and G. Springholz, *Appl. Phys. Lett.* **75**, 1246 (1999).

T. Schwarzl, G. Springholz, H. Seyringer et al., *IEEE J. Quantum Electron*. **35**, 1753 (1999).

W. Heiss, T. Schwarzl, J. Roither, G. Springholz, M. Aigle, H. Pascher, K. Biermann, and K. Reimann, *Prog. Quantum Electron.* **25**, 193 (2001).

[27] J. F. Butler, A. R. Calawa, R. J. Phelan, Jr., T. C. Harman, A. J. Strauss, and R. H. Rediker, *Appl. Phys. Lett.* **5**, 75 (1964).

[28] Z. Feit, D. Kostyk, R. J. Woods, and P. Mak, *Appl. Phys. Lett*. **58**, 343 (1991).

[29] U. Schießl and J. Rohr, *J. Infrared Phys. Technol*. **40**, 325 (1999).

[30] L. D. Hicks, T. C. Harman, X. Sun, and M.S. Dresselhaus, *Phys. Rev.* B **53**, R10493 (1996).

[31] G. Springholz, G. Ihninger, G. Bauer, M. M. Olver, J. Z. Pastalan, S. Romaine, and B. B. Goldberg, *Appl. Phys. Lett.* **63**, 2908 (1993).

[32] S. Yuan, G. Springholz, G. Bauer, and M. Kriechbaum, *Phys. Rev*. B **49**, 5476 (1994).

[33] G. Springholz, Holy, M. Pinczolits, and G. Bauer, *Science* **282**, 734 (1998).

[34] A. Rogalski, K. Adamiec, and J. Rutkowski, Narrow Gap Semiconductor Photodiodes (Bellingham, WA: SPIE, 2000).

[35] J. Faist, F. Capasso, D.L. Sivco, C. Sirtori, A.L. Hutchinson, and A.Y. Cho, *Science* **264**, 553 (1994).

[36] P. Muller, H. Zogg, A. Fach, J. John, C. Paglino, A.N. Tiwari, M. Krejci, and G. Kostorz, *Phys. Rev. Lett.* **78**, 3007 (1997).

[37] H. Zogg, K. Alchalabi, D. Zimin, and K. Kellermann, *IEEE Trans. Electron. Dev.* **50**, 209 (2003).

[38] R. Grisar, H. Böttner, M. Tacke, and G. Restelli (Eds.), Monitoring of Gaseous Pollutants by Tunable Diode Lasers (Kluwer Academic Publishers, Dordrecht, 1992).

[39] T. Schwarzl, W. Heiss, G. Springholz, M. Aigle, and H. Pascher, *Electron. Lett.* **36**, 322 (2000).

G. Springholz, T. Schwarzl, M. Aigle, H. Pascher, and W. Heiss, *Appl. Phys. Lett.* **76**, 1807 (2000).

[40] E. W. Baumgartner, T. Schwarzl, G. Springholz, and W. Heiss, *Appl. Phys. Lett.* **89**, 051110 (2006).

[41] D. Bimberg, M. Grundmann, and N. N. Ledentsov, Quantum Dot Heterostructures (Wiley, Chichester, 1998).

[42] J. Stangl, V. Holý, and G. Bauer, *Rev. Mod. Phys*. 7**6**, 725 (2004).

[43] V. A. Schchukin, N. N. Ledentsov, and D. Bimberg, Epitaxy of Nanostructures (Springer Verlag, Berlin, 2004).).

[44] J. Tersoff and F. K. LeGoues, *Phys. Rev. Lett*. **72,** 3570 (1994).

[45] G. Springholz and G. Bauer, *Phys. Stat. sol.* (b) **8,** 2752 (2007).

[46] A. Raab, R. T. Lechner, and G. Springholz, *Appl. Phys. Lett*. **80**, 1273 (2002).

[47] R. T. Lechner, T. Schülli, V. Holy, G. Springholz, J. Stangl, A. Raab, T. H. Metzger, and G. Bauer, *Appl. Phys. Lett*. **84**, 885 (2004).

Chapter Two

Growth Pits of Pb-Salt Epilayers Grown on Silicon Substrates

2.1 Defects in Semiconductors

Understanding the defects in semiconductors will lead to improve the performance of semiconductor devices for applications in civil and military technology. The focus of this research is the study of one kind of defects (growth pits) in IV-VI Pb-salt semiconductors. The goal is to understand how this kind of defect originate, their shapes, and their effects on the properties of the materials.

The physical characteristics of semiconductors are determined both by the properties of the host crystal and by the presence impurities and crystalline defects. Dopant impurities, which typically substitute for a host crystal atom, introduce electronic states in the bandgap close to the valence and conduction band edges and thus determine the type and conductivity of the material. These so-called shallow level defects enable the wide range of semiconductor devices available today. However, crystal lattice defects or other impurities, which introduce electronic states deeper in the bandgap and are referred to as deep level defects, also modify the properties of the semiconductor and thus may make a semiconductor unsuitable for its intended applications.

When a semiconductor film is grown epitaxially on a substrate that has a slightly different lattice constant, the lattice mismatch strain in the film may be relaxed by the introduction of misfit dislocations or other lattice defects. The electronic and optoelectronic devices for many important semiconductor applications are complex engineered structures in which both the lattice mismatch strain and the defects must be tightly controlled.

As is well known, some of the defects in the semiconductors play a dramatic role on the performance of the devices. For instant, detectivity (D*) of photovoltaic (PV) detectors is restrained by threading dislocations and operability of detectors is limited

by growth pits density in the semiconductors. While the main defects in Pb-salt semiconductors are exactly threading dislocations and growth pits.

2.1.1 Threading Dislocation in IV-VI Materials

The threading dislocations in IV-VI semiconductors were studied in references [1 2]. The scientists have found the ways to reduce the threading dislocation densities in lattice-mismatched layers. For Pb-salt semiconductors grown on the Si (111) substrates, the lattice and thermal expansion mismatch strain can be relaxed by glide of dislocations in the main {100} <110> glide system for epilayers which have the NaCl crystal structure. **Fig. 2.1** shows a schematic drawing of the glide and crystallographic geometry. Nearly complete strain relaxation is obtained in layers with a thickness of several μm, and on each temperature cycle, e.g., from room

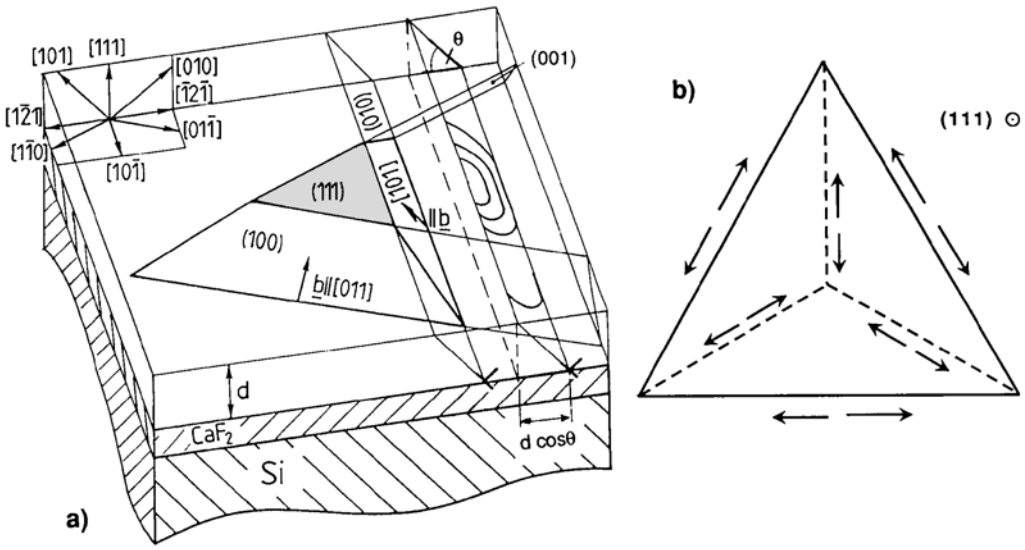

Fig.2.1. Schematic drawing of the arrangement of the {100} <110> glide system for the NaCl type PbSe (111) layers on Si(111). (a) Perspective drawing; (b) arrangement of possible *a*/2<110>-type Burgers vectors; dashed lines: Burgers vectors which are inclined to the interface and therefore belong to glissile dislocations. Taken from Muller *et al.*

temperature (RT) to 80 K. Even after more than 1400 such cycles, plastic strain relaxation still occurs on each temperature change, and it was estimated that the layers

had undergone a cumulative plastic deformation exceeding 400% in report[3]. The structural quality has changed only slightly after these procedures. Even higher quality of epilayers is obtainable if the samples are annealed at 200 – 400 ^{0}C in vacuum or Se vapor environment. An estimate based on geometrical arguments and the experimental findings was performed which predicted movements of the threading ends of misfit dislocations in the centimeter range in layers with dislocation densities of 10^8 cm^{-2} [4].

Etch-pit (threading dislocation) densities of typical PbSe layers after growth were 1×10^7 to 3×10^7 cm^{-2}. To demonstrate the easy mobility of threading ends, rectangular islands were etched into the layers. **Fig. 2.2(a)** shows the etch-pit density of an as-grown island. A homogeneous distribution of etch pits is observed. Similar islands of the same sample (but where no etch-pit treatment was applied) were heated to 300 ^{0}C, and etched after cool down to RT for etch-pit analysis. **Fig. 2.2(b)** shows a micrograph of such an island. The most striking feature is the extremely reduced etch-pit density over most of its interior. On all such rectangular islands investigated, similar patterns were reproducibly observed. All showed the same features, a very low

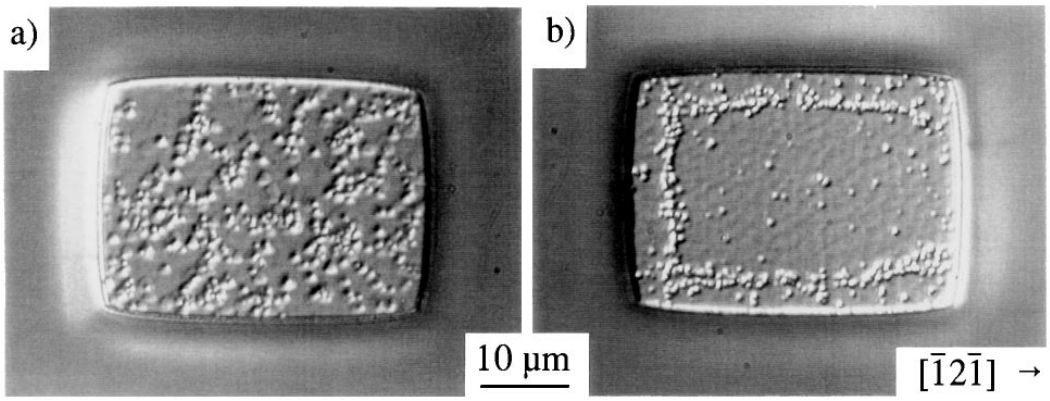

Fig. 2.2 Distribution of etch pits on rectangular PbSe (111) islands on Si(111) before (a) and after (b) a thermal cycle to 300 ^{0}C. The crystallographic orientation is plotted pointing into the same directions as in Fig. 2.1. Adapted from Zogg *et al.*

dislocation density in the interior, and an increased density along a U-shaped band

located a few micrometers away from the edges. This band runs along three of the four edges only, while no increased density is observed along the fourth edge (Fig 2.2 （b）right side). This latter edge runs parallel to the [101] direction formed by the intersection with the surface of the (010)-glide planes inclined away from the edge (i.e., the (010)-glide planes plotted in **Fig. 2.1** with the island on the left). On the other three edges with a different crystallographic orientation, a band with increased etch-pit density was observed. The asymmetry is correlated with the mechanical strain, which decreases to zero at the edges. For most orientations, it becomes too small near the edge to move the threading segment of the misfit dislocation completely out of the island. Only for edges oriented along [101] and with the (010)-glide planes inclined away as described, the strain field is changing in a manner that the threading ends can escape completely.

The decrease of dislocation densities (etch-pit densities) with increasing layer thickness is plotted in **Fig. 2.3.** A similar sample was etched down to different thicknesses and annealed, and the revealed etch pits in the interior of the samples were counted. With increasing thickness, the threading dislocation density at the surface of the layer decreases with approximately the square of the thickness *d*, which is different from III-V or II-IV semiconductors,

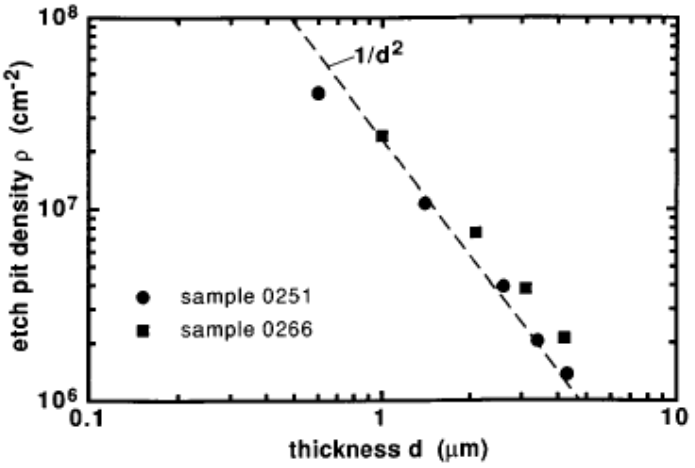

Fig. 2.3 Etch-pit density in PbSe (111) on Si(111) vs thickness *d* of the layers (points). A $1/d^2$ dependence is indicated by the dashed line. Taken from Fach *et al.*

where a $1/d$ scaling is observed, or even a leveling off of the density for thicker layers[5]. The $1/d$ dependence can be understood as the probability that two threading dislocations meet during growth in order to annihilate is proportional to dislocation density ρ[2 6]. The near $1/d^2$ dependence found in the study for annealed PbSe can be explained as follows: For a certain grown layer with thickness d (and before performing anneals or temperature changes), the threading dislocation density existed during growth scales with $1/d$ as described. When changing the temperature (after growth is completed), one has to take into account that each threading end of the misfit dislocations is able to glide along the whole layer dimension. If a threading dislocation does not encounter and react with any other threading dislocations on its glide across the whole sample, no change in the $1/d$ dependence results. However, assuming that this moving threading end encounters another threading end and reacts (annihilates or fuses) with it, a further dislocation reduction takes place. Remembering that all threading dislocations behave in this manner, the result must be that this reduction again scales with $1/d$ in order to finally achieve the observed $1/d^2$ dependence.

An explanation of this dependence has to take into account the inhomogeneous distribution of dislocations across the layer thickness. The junctions where two threading ends have reacted in the interior of the layer may be able to move further towards the interface as long as the dislocation density is low. Near the interface, the dislocation density increases and the junctions encounter more obstacles to move down. Thus, a higher decrease of the dislocation density is possible closer to the surface. Clearly, a $1/d^2$ dependence as compared to a $1/d$ dependence leads to a faster decrease of dislocation density with increasing layer thickness, which is of value for growth of thick layers with very low dislocation density. The exact nature of the

dislocation interactions for these NaCl-type semiconductors is not known and deserved further studies.

2.1.2 Growth Pits in II-VI Semiconductors

As compared to IV-VI materials, growth defects in II-VI semiconductors have been investigated extensively[7 8 9]. For example, in the prevailing II-VI material, $Hg_{1-x}Cd_xTe$ (MCT), different growth defects have been identified as dislocations, stacking faults and twins, voids and hillocks, as well as precipitates. **Fig. 2.4** shows typical

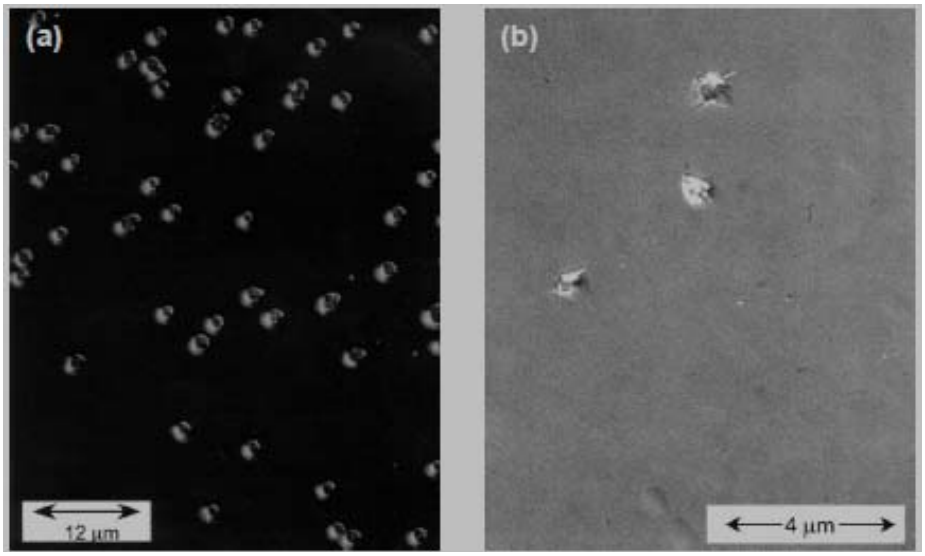

Fig.2.4 (a) Defects which appear to be voids inside hillocks. (b)Defect complexes where the hillocks appear to be associated with void edges. Taken from Chandra *et al.*

defect complexes (one kind of voids defects) in MCT. From the images, one can see the voids exist inside hillocks, or voidhillock complexes. These defect complexes appear to be associated with a nest of 'decorating' dislocations. This becomes apparent upon defect etching small sections of films such that the location of each individual defect complex is relatively precisely correlated during the etching process.

The large voids, with sizes usually greater than 5 µm, nucleated at the substrate-epilayer interface. The smaller voids, however, appeared to nucleate away from the substrate-epilayer interface. Direct evidence of these voids on cleaved cross-sections

of MBE-grown films has been obtained earlier[10] and reproduced in **Fig. 2.5.** As displayed, usually the voids, once nucleated either at the substrate-epilayer interface or away from it, continued to replicate through to the top surface of the films.

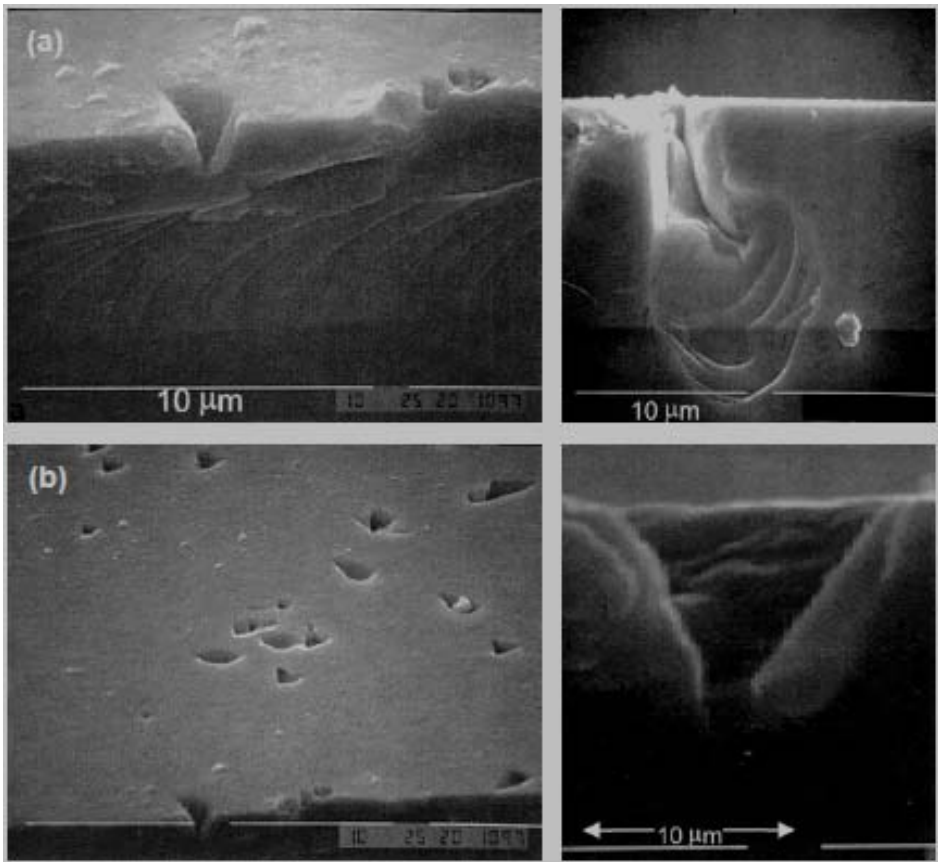

Fig. 2.5 Cross-sectional and three dimensional SEM microphotographs of void defects nucleated at various stages of MBE growth: at the growth interface, (a) in the middle of the growth run, (b) near the end of the growth run. Adapted from Aoariedn *et al*

Fig. 2.6 displays a fraction of the voids appears to close before reaching the film surface. Here the voids nucleated slightly away from the film-substrate interface, continued to replicate for a while as the growth progressed, but then relatively rapidly closed off at significant depths from the film surface. The whole sequence was completed before two-thirds of the film growth was completed. Examination of the top surface of these films does not reveal any indication of voids within the depth of the films. These only become apparent upon examination of cleaved cross-section of these films. Voids, which close during growth, can nucleate either at the interface or

away from the interface. Furthermore, these voids may not always be leaving any "fingerprints" on the top surface. Defect etching these films did not indicate a

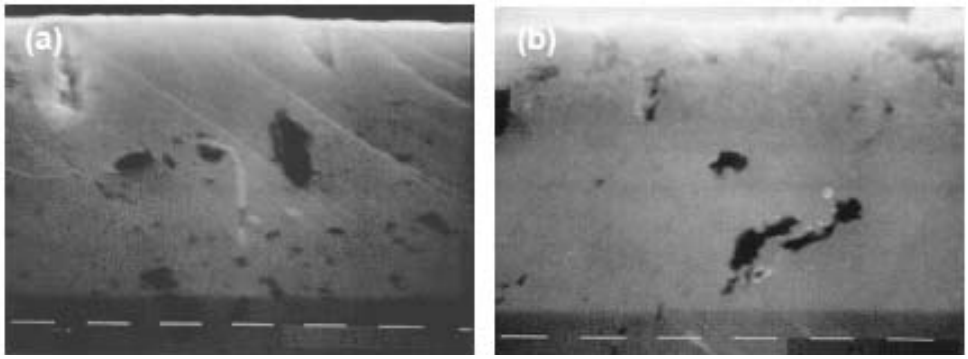

Fig.2.6 Cross-sectional SEM microphotograph of void defects which "closed" before the end of the growth. These voids will be completely hidden and not apparent from the top surface. Taken from Frazier *et al.*

presence of nesting dislocations. However, void density increased upon selective and progressive removal of the epilayers. When defect etching was performed following a partial removal of the film, dislocation nests were observed decorating these voids in some cases. An example is displayed in **Fig. 2.7.** No nests or decorative pattern of

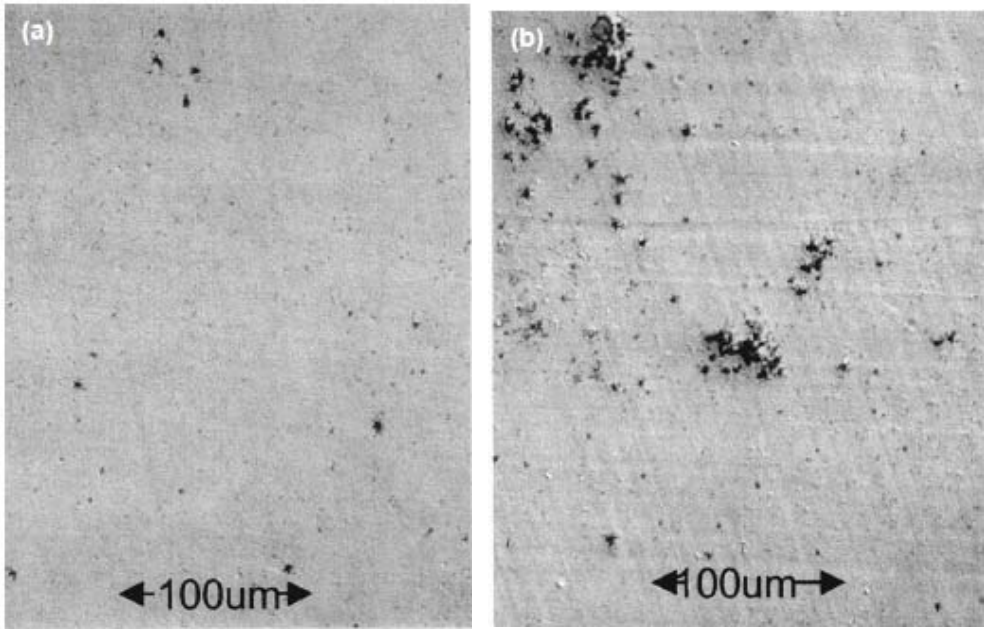

Fig.2.7. Dislocation etching of a MBE epilayer containing "hidden" voids. (a) Dislocation nests are not apparent on the top surface, (b) but become apparent upon removal of half of the film. Adapted from Shih *et al.*

dislocations were observed upon defect etching the top surface of a selected small section of a MBE film (**Fig. 2.7a**). Upon removal of approximately half of the film thickness by chemical etching, this section was then defect etched. A number of dislocation nests springs into view (**Fig. 2.7b**).

As stated above, Void defects during MBE growth of HgCdTe can nucleate at the substrate-epilayer interface as well as away from it. The latter kind of void defects is smaller in size compared to voids nucleating at the interface and appears to be usually present as a defect complex, which leads to the formation of an associated decorative dislocation nest. Both kinds of voids usually penetrate through to the surface of the films. However, examples where voids have closed before reaching the top surface of the films have been found. No indications of these hidden voids can be observed by examining the top surface of the films. Elimination of fluctuations in growth conditions, usually likely to be associated with multi-layer and multi-composition films, eliminated the formation of these complex defects.

2.2 Investigation of Growth Pits in IV-VI

Although IV-VI semiconductors like $Pb_{1-x}Sn_xSe$ show a comparably high capability in comparison to II-VI and III-V materials, such as $Hg_{1-x}Cd_xTe$ and InSb[11] [12], not many efforts have been devoted to exploring the full potential of IV-VI materials. Recently, an investigation of defects in the IV-VI Pb-salt materials was carried out by our research group and a significant conclusion in nature of growth pits was made according to our experimental results.

2.2.1 Samples Preparation

In this research, a single monocrystalline Lead salt (PbSe) layer was epitaxially grown on silicon substrate in a customer-designed MBE apparatus. Throughout the growth process, the reflection high energy electron diffraction (RHEED) patterns were recorded for confirmation of the quality of epilayer. Further details regarding to the growth have been described in elsewhere[13]. The surface morphology of epilayer was then characterized by Nomarski microscopy and scanning electron microscopy (SEM). Energy dispersive x-ray analysis (EDXA) was performed on the special area of the epilayer surface to investigate the composition of the growth defects.

Fig. 2.8 shows a Nomarski micrograph of an as-grown PbSe epilayer surface on a Si (111) substrate. A number of bright spots with various sizes are conventionally called "growth pits" or surface defects, which are also prevalent in epitaxial semiconductor materials such as $Hg_{1-x}Cd_xTe$ and SiC[14 15]. The detailed information about the growth pits in PbSe epilayer is presented through SEM observation. **Fig. 2.9** shows a typical SEM image of a PbSe epilayer grown on a Si (111) substrate, from which the detailed characteristics of the growth pits can be clearly observed. Higher resolution images of a small growth pit (labeled by a circle) are displayed in **Fig. 2.10** in plan view and Fig**. 2.11** in 60° oblique view. It is very interesting to note that the growth pit is composed of two micro-sized cuboids both of which have rectangular facets approximately parallel to



Fig. 2.8 Nomarski micrograph of an as-grown PbSe epilayer on Silicon substrate.

the (111) crystal plane of Si substrate. The 3-dimensional (3D) display of the micro-cuboids in **Fig. 2.11** shows that the upper part of the larger micro-cuboid extrudes outwards from the epilayer, and the facets of the micro-cuboid are vertically intersecting each other. **Fig. 2.12** provides a 3D image of another micro-cuboid. While the orientations of the micro-cuboids differ from one structure to another, similar micro-cuboids were readily observed in our samples.

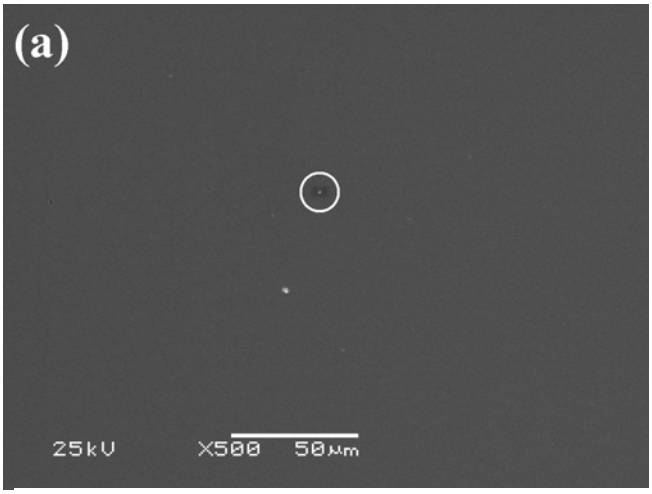

Fig. 2.9 SEM image of PbSe epilayer grown on a Si (111) substrate.

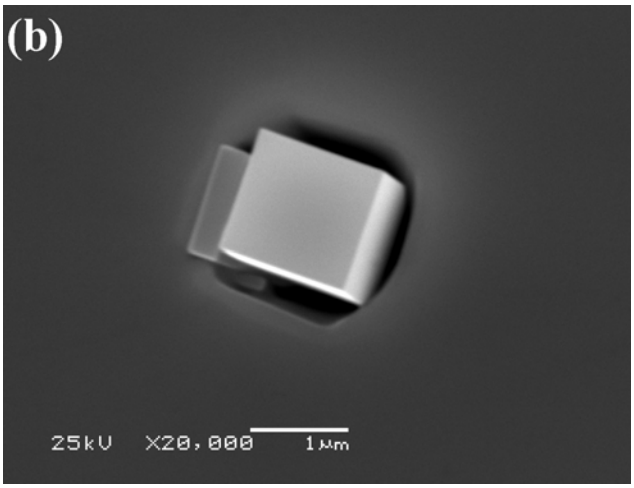

Fig. 2.10 Plan view of enlarged SEM image of the circled part in Fig. 2.9.

2.2.2 Composition of Micro-Cuboids

EDXA was conducted in order to investigate the chemical composition of the micro-cuboids. **Fig. 2.13** shows the EDXA spectrum of the micro-cuboid in **Fig. 2. 11**, where the two most intense peaks were identified to be lead and Selenium. Elemental analysis of EDXA shows that there is a very small compositional difference between micro-cuboids and the surrounding epilayer. The atomic percentages of Pb and Se are 51% and 46%, respectively, which indicates that both the micro-cuboids and the

epilayer are made of PbSe. Considering that IV-VI semiconductors like PbSe and PbTe possess a cubic NaCl-type structure, it is reasonable to identify the micro-cuboids as PbSe micro-crystals since both facets and regular shapes of micro-cuboids are of single crystalline character. The facets of the micro-cuboids in **Fig.2.11 and Fig.2.12** are most likely attributed to the {100} plane of lead salt materials. The RHEED patterns, however, indicate a three-fold rotational symmetry during the growth, which means that the crystalline orientation of the PbSe epilayers is along the <111> direction of Si substrate. The discrepancy of crystal orientations between PbSe epilayer and micro-crystal suggests that the PbSe micro-crystals may originate from a self-assembly growth mode which is completely different from the growth mechanism of the surrounding PbSe epilayers.

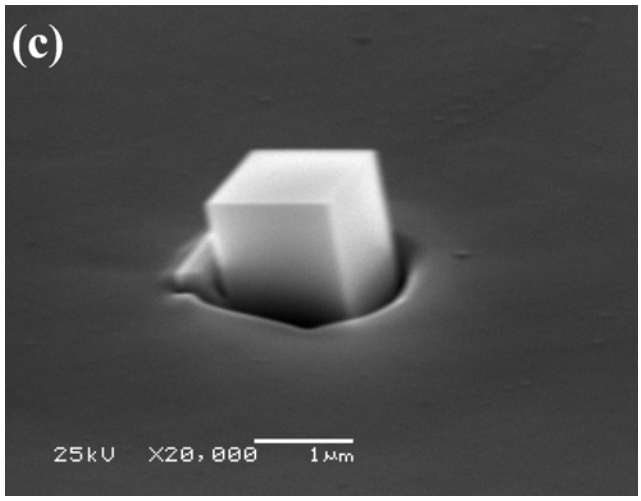

Fig. 2.11 60^0 oblique view of enlarged SEM image of the circled part in Fig. 10.

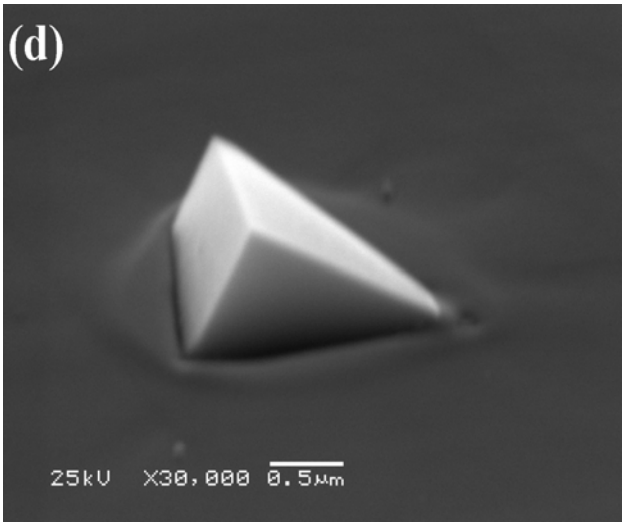

Fig. 2.12 3-D of SEM image of Micro-cuboid.

2.2.3 Multiple Growth Pits

In addition to the smaller growth pits (~1μm), several larger growth pits were also observed as shown in **Fig. 2.14** with a 60° oblique view. The size of those pits is more than 5μm. Obviously, this larger growth pit is a direct result of a stack of micro-cuboids with the size of each cuboid around 0.5 to 1 μm. However, every cuboid has a specific crystal orientation, and the size of single micro-cuboids is not uniform. Some of the smaller cuboids are so close to their neighbors, so it is difficult to identify individual cuboids because they overlap or merge with each other, appearing as irregular shapes.

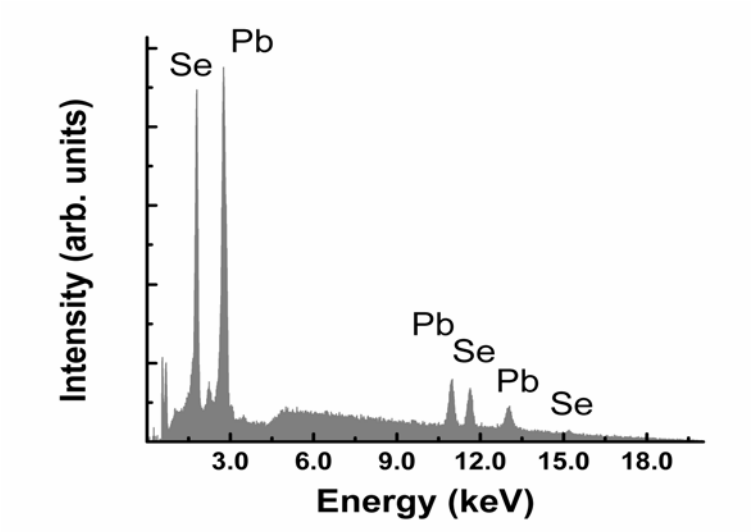

Fig. 2.13 A typical EDXA spectrum of micro-cuboids.

2.2.4 Origin of Growth pits

Regardless of the size of the growth pits, there are always narrow gaps between micro-cuboids and surrounding epilayers, which indicates that these micro-cuboids are in fact embedded in PbSe epilayer rather than simply on the surface. This

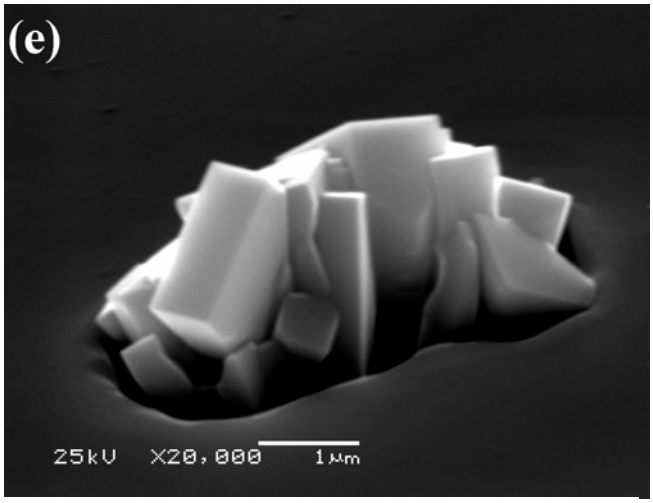

Fig.2.14 SEM image of a ~5 μm growth pit with a 60° oblique view formed by A cluster of single micro-cuboids.

line of reasoning is confirmed in **Fig. 2.15**, where a cross-sectional SEM image of a cleaved sample clearly shows that the "roots" of the micro-cuboid are located near the middle of the epilayer. However, this is one representative case as the roots of other micro-cuboids were found at various depths throughout the profile of the epilayers. Additionally, if the surface of the epilayer was blown by nitrogen or cleaned in an ultrasonic bath, most of large micro-cuboids were removed and craters were left behind them (see Fi**g. 2.16**). The depths of craters differ and follow the general rule: the larger the size of micro-cuboid, the deeper the crater. These results indicate that the nucleation of PbSe micro-crystals can take place at various stage of the epitaxial growth, while the heights and volumes of micro-crystals increase along specific crystal orientations as the epitaxial growth is ongoing.

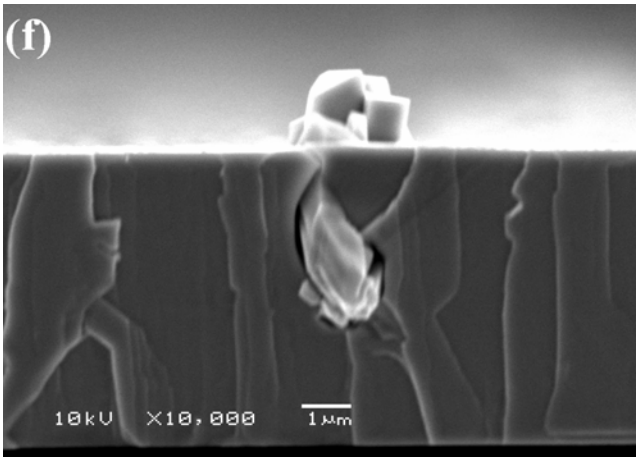

Fig.2.15 Cross-sectional SEM image of a cleaved sample which clearly shows that the "roots" of the micro-cuboid are located near the middle of the epilayer.

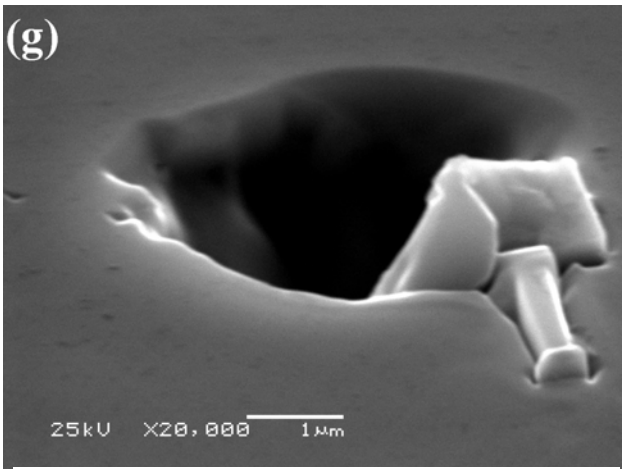

Fig. 2.16 SEM image of crater after the surface was blown by nitrogen gas.

2.2.5 Conclusions on Growth Pits

All of these results provide definite clues about the growth mechanism of micro-cuboids. As mentioned above, the individual micro-cuboids can be identified as PbSe micro-crystals, but the random crystalline orientation of all micro-cuboids is a strong indication of polycrystalline growth. Herein, we tentatively assume that polycrystalline seeds provide the initial stage of micro-cuboidal growth. In subsequent stages, single crystalline PbSe micro-crystals will grow randomly along various crystal orientations of the polycrystalline seeds. Apparently, the growth along <100> is faster than the growth in other directions since the {100} facets have a lower surface energy than that of the higher index planes. This reason coincides with the growth of other PbSe nano-crystals whose shapes vary from spherical to highly faceted truncated octahedrons to cubic with sizes ranging from several nanometers to tens of nanometers[16] . We believe that in our case, once the polycrystalline seeds are formed at a certain stage, the high growth rate of micro-cuboids promotes the out-plane growth and the self-assembling of micro-cuboids. Because the height and volume of micro-cuboids prevents further deposition in the shadows of micro-cuboids, gaps will appear between micro-cuboids and epilayers.

Interestingly, after we decorated the threading dislocations in PbSe epilayers using H. Hogg's etching technique[17] , there are no extra dislocations observed around growth pits. However, the situation is reverse for II-VI materials grown by MBE. The dislocation densities always increase in the areas near growth defects like voids and void/hillock for II-VI materials[18] . In our case, the gaps between micro-cuboids and the epilayer are believed to play an important role, because the gaps prevent the stem of micro-cuboids from coming into contact with the epilayer, the micro-cuboids will not introduce extra strain fields into the epilayer around them. Once passivated by post-growth treatments, these larger defects, which are actually highly-crystalline

material, are not expected to negatively impact the performance and reliability of fabricated devices. Additionally, it should be noted that the same structures of PbSe micro-crystals were also found in PbSe and PbSnSe epilayers grown on BaF_2 (111) substrates, which means that the formation of micro-crystals is a common fact for IV-VI epitaxial growth.

Possible explanations behind the polycrystalline seed nucleation include the large lattice mismatch between lead salt materials and silicon substrates or surface contaminations. Here we present only preliminary results and discussions about the structures and morphologies of the growth pits in Pb-salt semiconductor on Si substrate. In order to further clarify the growth mechanism, IV-VI epilayers grown on the different substrates should be investigated and other high-precision characteristic techniques such as transmission electron microscopy (TEM) are required.

2.3 References

[1] A. FACH, J. JOHN, P. MULLER, C. PAGLINO, and H. ZOGG, *J. Electron. Mater.* **26**, 873 (1997).

[2] P. Müller, H. Zogg,* A. Fach, J. John, C. Paglino, A. N. Tiwari, and M. Krejci, *Phys. Rev. Lett.* **78**, 3007 (1997).

[3] H. Zogg, S. Blunier, A. Fach, C. Maissen, P. Müller, S. Teodoropol, V. Meyer, G. Kostorz, A. Dommann, and T. Richmond, *Phys. Rev.* B **50**, 10801 (1994).

[4] H. Zogg, P. Müller, and A. Fach, *Mater. Res. Soc. Symp. Proc.* **379**, 27 (1995).

[5] J. S. Speck, M. A. Brewer, G. Beltz, A. E. Romanov, and W. Pompe, *J. Appl. Phys.* **80**, 3808 (1996).

[6] H. Kroemer, T.-Y. Liu, and P. M. Petroff, *J. Cryst. Growth* **95**, 96 (1989).

[7] D. Chandra, F. Aqariden, J. Frazier, S. Gutzler, T. Orent, W. D. Shih, *J. Electron. Mater.* **29**, 887 (2000).

[8] Y. Chang, G. Badano, J. Zhao, C. H. Grein, and S. Sivananthan, T. Aoki and David J. Smith, *Appl. Phys. Lett.* **83**, 4785 (2003).

[9] I.V. Sabinina, A.K. Gutakovsky, Yu.G. Sidorov, A.V. Latyshev, *J. Cryst. Growth* **274**, 339 (2005).

[10] D. Chandra, H.D. Shih, F. Aqariden, R. Dat, S. Gutzler, M.J. Bevan, and T. Orent, *J. Electron. Mater.* **27**, 640 (1998).

[11] A. Rogalski, *Infrared Phys.* **28**, 139 (1988).

[12] H. Zogg, A. Fach, C. Maissen, J. Masek, S. Blunier, *Opt. Eng*. **33**, 1440 (1994).

[13] Z. Shi, X. Lv, F. Zhao, A. Majumdar, D. Ray, R. Singh, and X. J. Yan, *Appl. Phys. Lett.* **85**, 2999 (2004).

[14] X. Ma , H. Chang, Q. Zhang and T. Sudarshan, *J. Cryst. Growth* **279**, 425 (2005).

[15] L. Chen, Y. Wu, M. F.Yu, S. L. Wang, Y. M. Qiao, L.He, *J. Infrared Millim. Wave* **20**, 406 (2001).

[16] A. J. Houtepen, R. Koole, D. Vanmaekelbergh, J. Meeldijk, and S. G. Hickey, *J. Am. Chem. Soc*. **128**, 6792 (2006).

[17] A. Fach, J. John, P. Muller, C. Paglino, and H. Zogg, *J. Electron. Mater*. **26**, 873 (1997).

[18] P. S. Wijewarnasuriya, M. Zandian, D. B. Young, J. Waldrop, D. D. Edwall, W. V. Mclevige, D. Lee, J. Arias and A. I. D'Souza, *J. Electron. Mater*. **28**, 649 (1999).

Chapter Three

A Novel In-situ Surface Treatment during MBE Growth of PbSe on CaF_2/Si(111) Heterostructure

3.1 Introduction of Surface Treatment for II-VI Epitaxy

In-situ surface treatment is extensively used in the interfaces during growth of semiconductors on mismatched substrates. For example, a nitrogen-plasma (N-Plasma is one kind of *in-situ* surface treatment) was applied to the interfaces between substrates and epilayers during MBE growth of ZnSe on Si (111) for improving the quality of the epilayers[1].

As we know, high quality ZnSe epilayers are difficult to obtain due to the chemical and mechanical mismatch between ZnSe and Si. The ~ 4.3% lattice mismatch and the difference in the thermal expansion coefficients between these two materials are responsible for the introduction of crystal defects like dislocations and stacking faults[2 3]. On the other hand, it is known that an imbalance in the interface charge is one of the serious problems associated to the growth of a polar semiconductor on a nonpolar one[4]. For example, at the (100) interface between Si and the Se plane of ZnSe, the interface bonds will each receive a total of 5/2 electrons per bond instead of the two electrons required. This excess charge would generate a huge internal electric field. Harrison et al[4] suggested that in order to eliminate the excess charge the growth process itself produces modifications in the ideal atom arrangement resulting in a distorted interfacial geometry. Moreover, if the bonding problems at the interface are such that in the absence of any flux of Se, the sticking coefficient of Zn on the Si surface is very small[5]. Furthermore, chemical reactions between Si and Se at the interface during the very initial stage of growth cause the formation of a thin $SiSe_x$ amorphous interlayer[6 7]. This layer hinders the smooth growth of ZnSe, resulting in a high density of crystal defects in the films. From the above statements, it is clear that the control of the initial stages of growth is essential in order to reduce the defect density.

The scientists described the effects of Si substrate surface irradiation with plasma of nitrogen (N-plasma) prior to the molecular beam epitaxial (MBE) growth of ZnSe, and found that a substantial improvement on the crystal quality of ZnSe epilayers on Si(111) can be achieved by this novel substrate surface treatment with N-plasma[1]. The use of this surface treatment allowed the researchers to obtain a two dimensional growth of ZnSe on Si, as revealed by the presence of reflection high-energy electron diffraction (RHEED) oscillations at the initial stages of growth.

3.1.1 N-plasma Si Surface Treatment

N_2 gas was introduced in the MBE chamber when the oxide was fully desorbed from the Shiraki-cleaned Si (111) surface. In order to increase the reactivity of nitrogen with the Si surface, an rf-plasma discharge source was used to produce highly reactive nitrogen species[8]. After the N-plasma treatment the substrate surface showed a RHEED pattern with bulk 1×1 streaks and a blurred 7×7 reconstruction, as observed in **Fig. 3.1.**

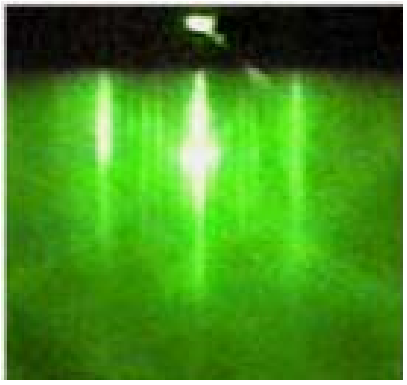

Fig. 3.1 RHEED patterns of N-plasma treated Si(111) substrate. Taken from Méndez-García *et al*.

Fig. 3.2 shows the RHEED pattern obtained after 8 ML of ZnSe grown by conventional MBE directly on Si(111) without the N-plasma treatment. The intense bulk spots and the diffuse background are indicative of a three-dimensional growth mode. With further growth,

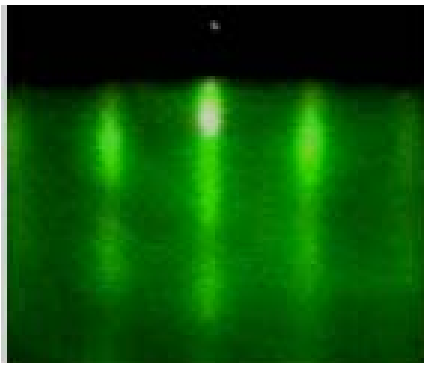

Fig. 3.2 RHEED patterns of Growth of 8 ML ZnSe on an untreated Si(111) substrate. Adapted from López-López*et et al.*

crystal defects became evident by the appearance of extra-spots indicating the formation of twinned regions, as observed in the RHEED pattern of **Fig. 3.3** that corresponds to the growth of 30 ML of ZnSe. It is difficult in obtaining a smooth ZnSe growth by this technique. The three-dimensional islands resulting from the direct MBE growth on untreated Si substrates are shown in **Fig. 3.4.**

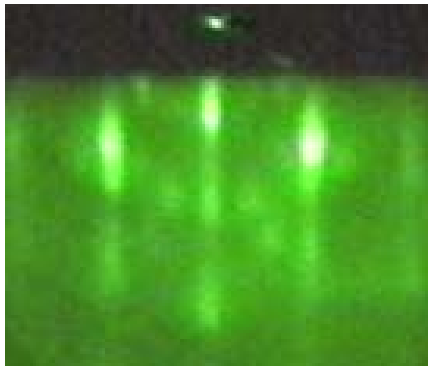

Fig. 3.3 RHEED patterns of 30 ML of ZnSe grown by conventional MBE directly on an untreated Si(111) substrate. Taken from Méndez-García *et al*.

3.1.2 Improvement by Surface Treatment

The great improvement in the epitaxy obtained when growing on a Si surface treated with N-plasma. **Fig. 3.5** shows the RHEED pattern obtained after 8 ML of ZnSe grown by pulsed MBE on an N-plasma treated substrate. The RHEED pattern looks very streaky, and moreover a 2-fold reconstruction can be observed suggesting a two-dimensional growth mode and an atomically ordered surface. The improved epitaxy is evident when comparing these RHEED patterns with the corresponding patterns obtained by direct

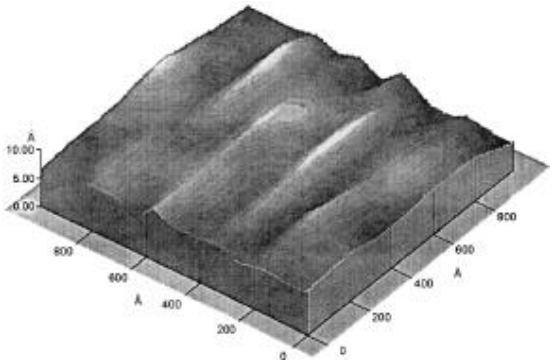

Fig. 3.4 Atomic force microscopy images of 30 ML of ZnSe grown by conventional MBE directly on a treated Si substrate. Adapted from Hernández-Calderón *et al.*

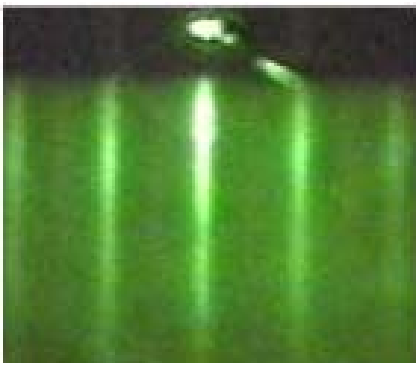

Fig. 3.5 RHEED patterns of 8 ML and (f) 30 ML of ZnSe grown by pulsed MBE on an N-plasma treated Si(111). Taken from López-López*et et al.*

MBE on untreated substrates (**Figs. 3.2**). The RHEED patterns in **Figs. 3.5** have a low background and are much streakier, indicating a flat surface.

Auger measurements revealed a better ZnSe-coverage for the N-plasma treated Si surface, supporting the idea of a layer by layer growth promotion by this technique. The AFM image in **Fig. 3.6** confirmed the flatter ZnSe surface obtained on the N-plasma treated Si surface.

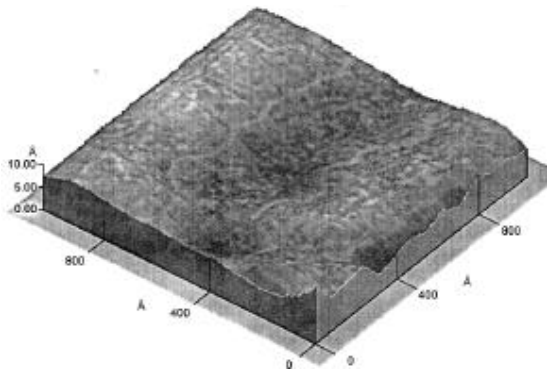

Fig. 3.6 30 ML of ZnSe grown by pulsed MBE on an N-plasma treated Si substrate. Taken from Hernández-Calderón *et al.*

3.1.3 Growth Model

The two dimensional growth could be induced by the formation of a nitrogen interlayer that avoid the formation of the $SiSe_x$ compound, and could balance the electric charge at the ZnSe/Si interface, thus allowing the growth of a smooth ZnSe epilayer.

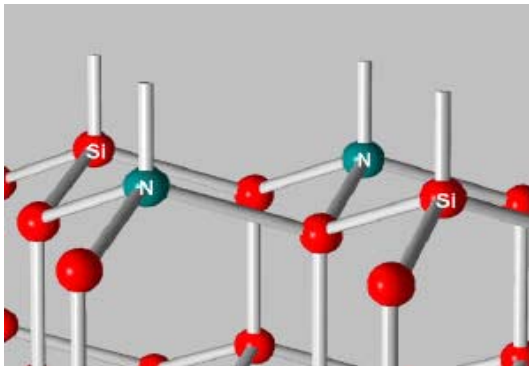

Fig 3.7 Schematic picture of a possible atomic arrangement of the Si surface after the N-plasma treatment. Adapted from Uhrberg *et al.*

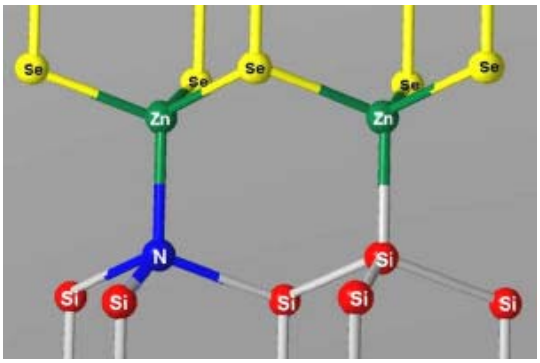

Fig 3.8 Schematic picture of a possible atomic arrangement in the early stages of the ZnSe growth. Taken from Uhrberg *et al.*

For the (111) interface a sub-monolayer amount of nitrogen is enough. For example, charge balance occurs when the nitrogen atoms displaces Si atoms and take the place of 50% of the surface sites, so the N atoms share

three bonds to the substrate, as shown in Fig. 3.7.. In this way the growth could smoothly continue with a complete monolayer of Zn atoms bonded to a surface formed by Si and N, as illustrated in **Fig. 3.8**. A different sub-monolayer amount of N could be possible depending on the particular atomic geometry at the Si surface. The partial coverage of the Si(111) surface with nitrogen could be reflected by the blurred 7x7 reconstruction after the N-plasma treatment, as shown in **Fig. 3.2.**

3.2 *In-Situ* Treatment for IV-VI Epitaxy

Although many of the methods were applied to reduce the defects in IV-VI epilayers grown by MBE, such as low and high temperature cycling, defects are still the major challenge for device applications especially for epitaxy on Si substrate. In particular, the growth pits and etch pits in the Pb-salt semiconductors are relatively higher than those in III-V and II-VI materials. For instance, the threading dislocations density in Pb-salt epilayers is usually from high 10^6 to low 10^8 cm^{-3}, compared to MCT with dislocation density of only $10^4 \sim 10^5$ cm^{-3}. Hence, reduction of dislocations in IV-VI semiconductors is critical for high performance device applications. In this research, we explored a new surface treatment method to reduce dislocation density. This method, as is described in the following section, will reduce the thermal mismatch as well as the lattice mismatch between the interfaces.

3.2.1 Motivation of research

The continual improvement of IV-VI materials grown by molecular beam epitaxy (MBE) is a key step in the development of IV-VI infrared semiconductor devices on silicon substrates. This research presents a novel surface treatment method which is carried out during MBE growth of monocrystalline PbSe on Si(111)-oriented

substrates. Details of the experimental procedures are described and supported by reflection high-energy electron diffraction (RHEED) patterns. The effect of the *in-situ* surface treatment method is exhibited in the forms of improved electrical and morphological properties of PbSe thin films. Specially, the carrier mobility increases almost three-fold at 77K and nearly two-fold at 300K. The density of the growth pits undergoes almost three-fold reduction, whereas the density of the threading dislocations decreases around four-fold respectively after surface treatment.

3.2.2 Traditional growth of Pb-salt on Si

One of the most important applications for IV-VI semiconductors is the detection of light in the mid- and far- infrared region. Growth of homogeneous high quality materials on Si substrates makes IV-VI semiconductors a promising candidate for the large format focal plane array (FPA) detectors.[9] It has already been shown that IV-VI detectors especially those based on $Pb_{1-x}Sn_xSe$ materials grown on Si substrate offer high sensitivity similar to that of MCT detectors.[10] [11] Nonetheless, the full potential of IV-VI semiconductor detectors is not yet entirely realized, mainly due to lattice and thermal expansion mismatch of IV-VI materials with Si substrate. These mismatches introduce defects such as dislocations. As is well known, defects in semiconductors play a critical role on the performance of the devices. There are primarily two kinds of defects in epitaxial IV-VI semiconductor materials – threading dislocations and growth pits.

The thermal expansion and lattice parameter mismatches between PbSe and silicon substrates are about 12% and 700% at 300K respectively (see **Table II**). Despite these large mismatches, high quality IV-VI layers can still be grown on (111)-oriented silicon substrates successfully and hence reported.[12] Initial work in this area

focused on using a stacked BaF_2/CaF_2 buffer layer on Si substrate, but later MBE-growth results have shown that just a thin CaF_2 layer produces good PbSe epitaxy.[13] This fluoride buffer layer, even when as thin as 20 Å, appears to be necessary for good PbSe epitaxy since attempts to grow PbSe directly on Si(111) substrate have resulted in poor layer quality.[14] The layer-by-layer growth modes for both CaF_2 and PbSe are observed by RHEED intensity oscillations and reported in literature. After growth, the epilayers are reported to be entirely free of cracks and their crystalline quality is reasonably good as evidenced by high resolution X-ray diffraction (HRXRD) with full-width half-maximum (FWHM) values of typically less than 200 arcsec.[15] However, the dislocation density in all these reports has still been in the range of high 10^7 cm^{-2}, which needs to be further reduced for high device performance.

Up to date, post growth annealing seems to be the most effective way implemented to reduce the dislocation density in IV-VI epilayers after MBE growth lead salt on mismatched substrates, but the lowest dislocation density by annealing seems to be limited to mid 10^6 cm^{-2} even after 1400 cycles.[16] So it is highly desirable to develop other ways to reduce defect density either before or after growth. A promising method is substrate treatment before growth. Based on this idea, we designed a MBE-growth procedure for obtaining high quality IV-VI epilayers with further reduced defect density. Several buffer layers are applied between CaF_2/Si substrate and PbSe epilayer in relation to their crystal structure, lattice constant and thermal expansion coefficient.

3.2.3 Design of Experimental Procedure

Based on the properties of IV-VI semiconductors as well as the characteristics of their MBE growth (see Table II), we figured out an experimental procedure during

MBE-Growth of PbSe on CaF_2/ Si(111) heterostructure for further reducing growth defects and thread dislocations. According to the material properties, in particular

Materials Properties	Silicon	CaF_2	SrF_2	SrSe	PbSe
Thermal expansion coefficient ($\mu m \cdot m^{-1} \cdot K^{-1}$)	2.6	18.85	18.1	7.3	19.4
Crystal structure	Face-Centered Cubic	Cubic Closest Packing	Cubic Closest Packing	Rock salt	Rock salt
Lattice constant (Å)	5.4309	5.464	5.7996	6.2509	6.124

Table. II. Properties of semiconductor materials related to surface treatment at 300K

their crystal structure, lattice parameters and thermal expansion coefficients and our feasible sources as well MBE chamber conditions, we designed a detailed growth approach by considering every growth parameter such as substrate temperature, source flux, growth time, etc. The details of the designed experiments are shown in **Fig. 3.9.** In the traditional growth method PbSe film is directly grown on

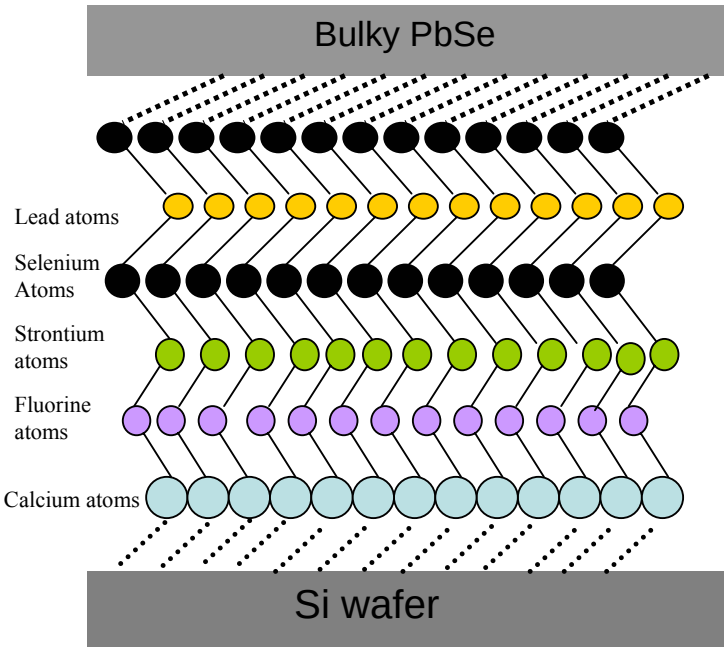

Fig. 3.9 Schematic of layer by layer growth of the in-situ surface treatment.

CaF_2/ Si(111) substrate without any additional treatment, like ZnSe directly grown on Si substrate. However, under the treated growth procedure, several more layers are grown between substrate and epilayer as shown in **Fig. 3.9**. Strontium source is open for a while right after CaF_2 growth, it is expected that a single atomic layer of SrF_2 can be formed on the CaF_2 surface at high surface temperature, moreover, no extra strain introduces during this growth due to the same crystal structure of the CaF_2 and SrF_2. Next, selenium source is opened for growth of the SrSe on SrF_2. It is supposed that Se atoms are only reacted by Sr atom on the surface and thus the surface is covered Se atoms after this step. Finally, PbSe is grown on SrSe with the reduced lattice mismatch and the same crystal structure.

3.2.4 *In-situ* Surface Treatment Procedure

As stated above, the Pb-salt semiconductors are generally grown on the cleaved bulk BaF_2 or on silicon with fluoride buffer layers. To further improve the quality of the epilayer, we figured out an *in-situ* surface treatment procedure. In this procedure, PbSe thin films were grown on a (111)-oriented Si substrate covered by several buffer layers using a compound PbSe source and an elemental Se source. A single-sided polished p-type Si substrate (resistivity ~ 100 ohm-cm) was prepared by the modified-Shiraki cleaning method for epitaxial

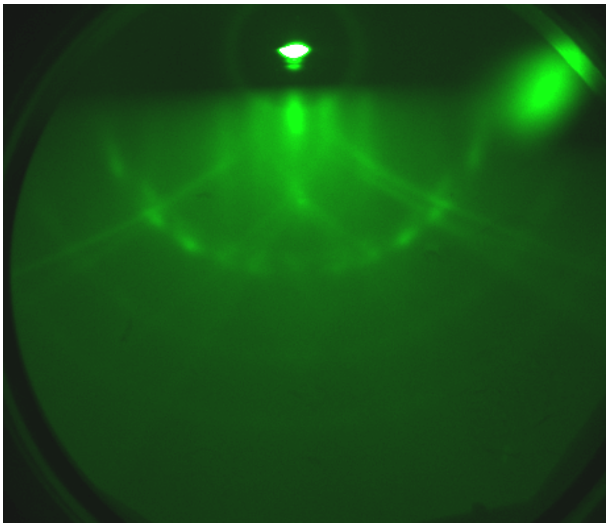

Fig. 3.10 RHEED pattern (20 kV) from a clean Si (111) surface at 770°C with the streaky (7x7) surface reconstruction along [112] incidence

growth. When the substrate temperature reached 770 ºC, a clear 7x7 reconstruction RHEED pattern (as seen in **Fig. 3.10**) indicates the oxidation layer was thoroughly removed and the substrate surface was ready to grow fluoride buffer layers on it. A 20 Å thick CaF_2 layer was then grown as a buffer layer whose quality was confirmed by RHEED pattern in **Fig. 3.11 (a**).

The substrate with buffer layers was then transferred to the main MBE chamber for PbSe growth. At this time, an optimized surface treatment method was applied to CaF_2/Si heterostructure. When the substrate was heated up to 530 ºC, the strontium source associated with the main chamber was opened for 200 seconds. Thus the substrate surface was covered with SrF_2 as evidenced by RHEED in **Fig.3.11 (b**). Subsequently, the selenium source attached to the main chamber was opened for 30 seconds and at this point, the surface was covered with SrSe as evidenced by RHEED image shown in **Fig. 3.12**. Finally, the substrate temperature was set at 375 ºC and a PbSe single layer was grown on the treated substrate. The RHEED pattern in

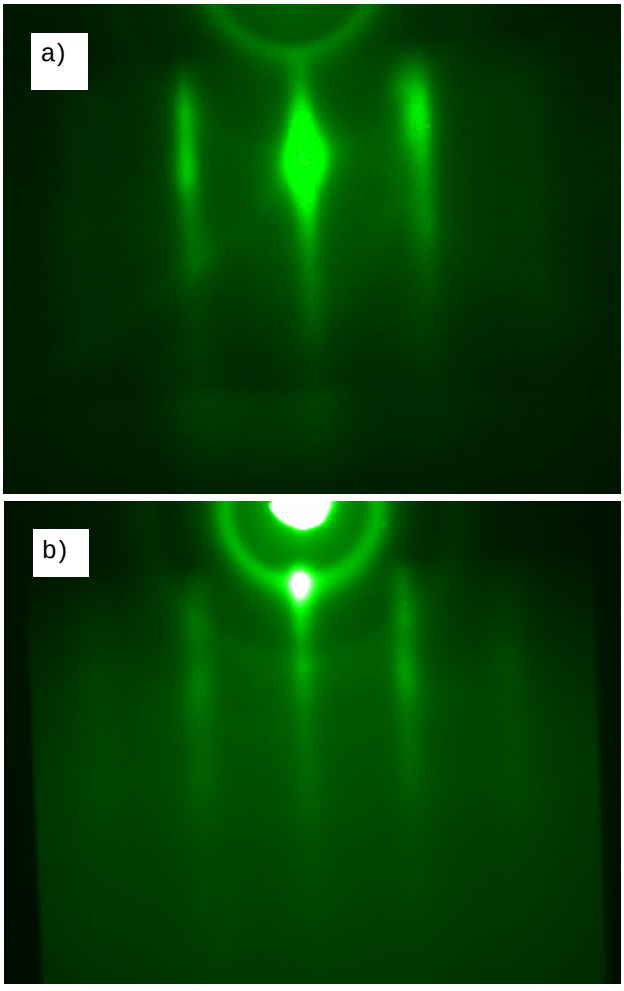

Fig.3.11 RHEED image in the [112] azimuth (a) during growth of the CaF_2 layer at a temperature of 770^0C and (b) during growth of the SrF_2 layer at a temperature of 530^0C

Fig.3.13 confirmed the epitaxial growth of the lead salt layer. During the growth of PbSe, a 12% Se-to-PbSe flux ratio was maintained while the growth rate was kept constant at 2.0 μm/hr.

3.2.5. Results and Discussion

The buffer layers grown by the optimized *in-situ* surface treatment at the interfaces between CaF_2/Si and IV-VI epilayer are to reduce lattice and thermal mismatches between the adjacent layers in a gradual manner. [17] The purpose of growing each buffer layer is described in detail as following. Firstly, a thin CaF_2 layer is grown on the Si (111) substrate because mismatch of their lattice parameters is only 0.6% at 300K (see Table. II).The thickness of CaF_2 layer is controlled within the critical thickness of CaF_2 on Si substrate at the corresponding temperature. Secondly, the

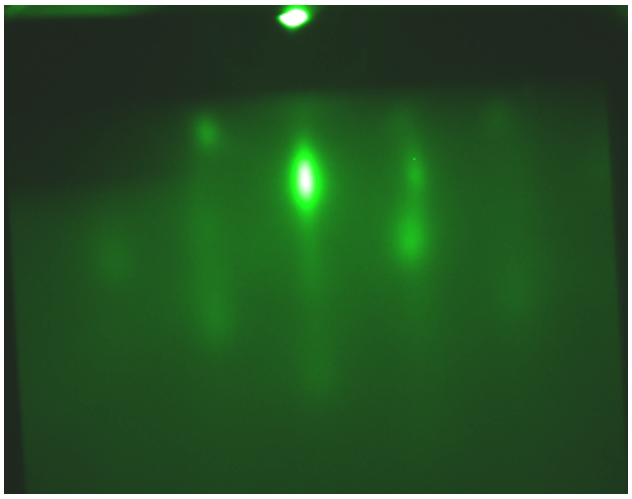

Fig.3.12 RHEED image in the [112] azimuth during exposure of the SrF_2 /CaF_2 layer in selenium flux at a temperature of 530^0C

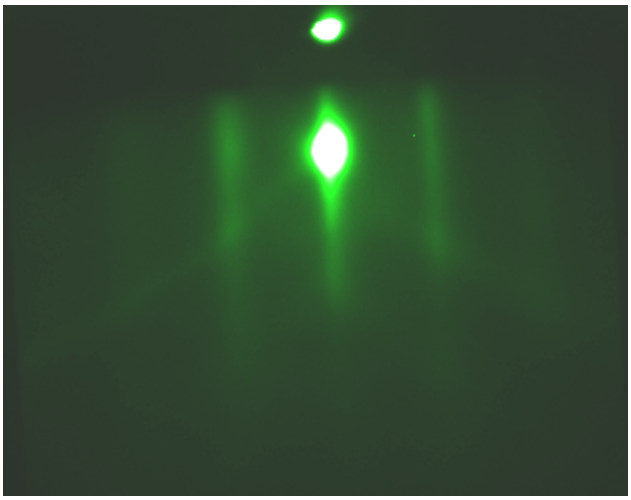

Fig.3.13 RHEED image in the [112] azimuth during growth of the PbSe layer at a temperature of 375^0C

CaF_2 layer is exposed to strontium flux so as to form a single atomic layer of SrF_2, whose thermal expansion coefficient is nearly the same as that of CaF_2. There is no visible change on the RHEED patterns during growth of SrF_2 as seen in **Fig.3.11 (a**) and Fig.**3.11 (b),** because the crystal structures of CaF_2 and SrF_2 are the same and also their lattice mismatch is only 5 % at 300K (see Table. II). However, there is indirect evidence which supports the formation of SrF_2 on CaF_2. If a CaF_2 layer without the strontium treatment is directly exposed to the selenium flux at 530 ºC, RHEED patterns have no change even after several hours' exposure. However, there is an obvious change on the RHEED patterns after strontium and then selenium treatments as seen in **Fig. 3.12**. Thirdly, the SrF_2 layer is exposed to selenium flux in order to deposit a single atomic layer of SrSe on SrF_2 surface. As already mentioned, there is a visible change on the RHEED patterns during growth of the SrSe layer because the crystal structures of SrF_2 (Cubic Closest Packing) and SrSe (Rock salt) are totally deferent. Actually, the SrF_2 and SrSe layers are the elastic-strain layers,

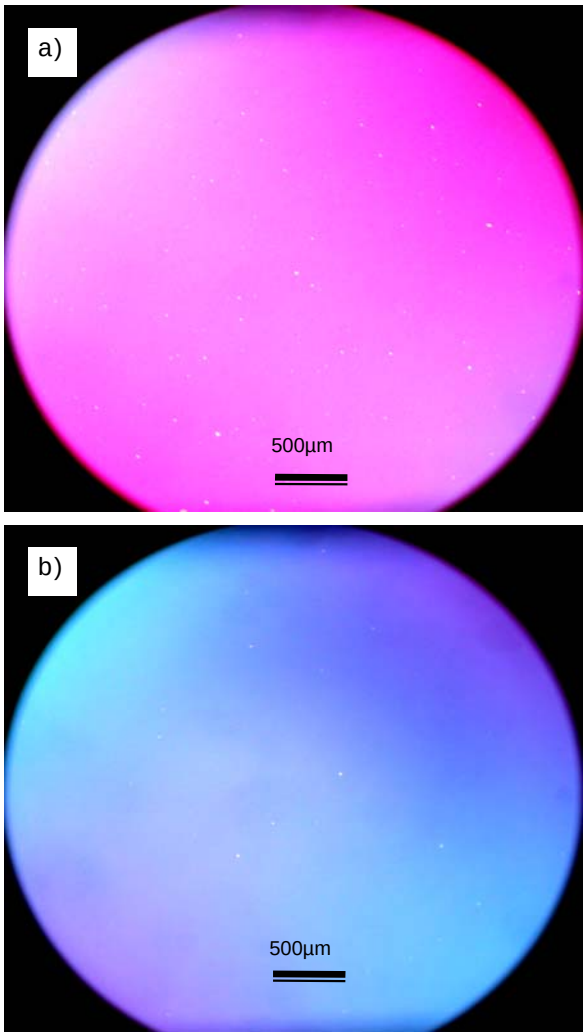

Fig. 3.14 Nomarski images of growth pits (a) in traditional growth: 1352 cm^{-2} (size <5µm) and 383 cm^{-2} (size >5µm) and (b) pits in optimized growth: 454cm^{-2} (size <5µm) and 167 cm^{-2} (size >5µm)

which help in releasing strain by reducing lattice and thermal mismatch between the CaF_2/Si heterostructure and the PbSe epilayer.[18 19] Finally, a monocrystalline PbSe layer is grown on the SrSe surface (see RHEED patterns in **Fig. 3.13)** because their crystal structures are the same and their lattice mismatch is only 2% at 300K.

After the MBE growth, the samples are taken out and the growth pits density is measured under the Nomarski microscope. The improvement by the *in-situ* surface treatment on the reduction of growth pits density is almost three-fold. The growth pits density decreases from 1735 cm^{-2} by traditional MBE-growth to 621 cm^{-2} by the improved MBE-growth as shown in **Fig. 3.14 (a) and Fig. 3.14 (b).** This, on the other hand, signifies that the defect limited operability of the detector based on such improved IV-VI materials increases from 99.60% to 99.85% theoretically, where the pixel operability is predicted for 30μm x 30μm pixels with 30μm pixel spacing. The etch

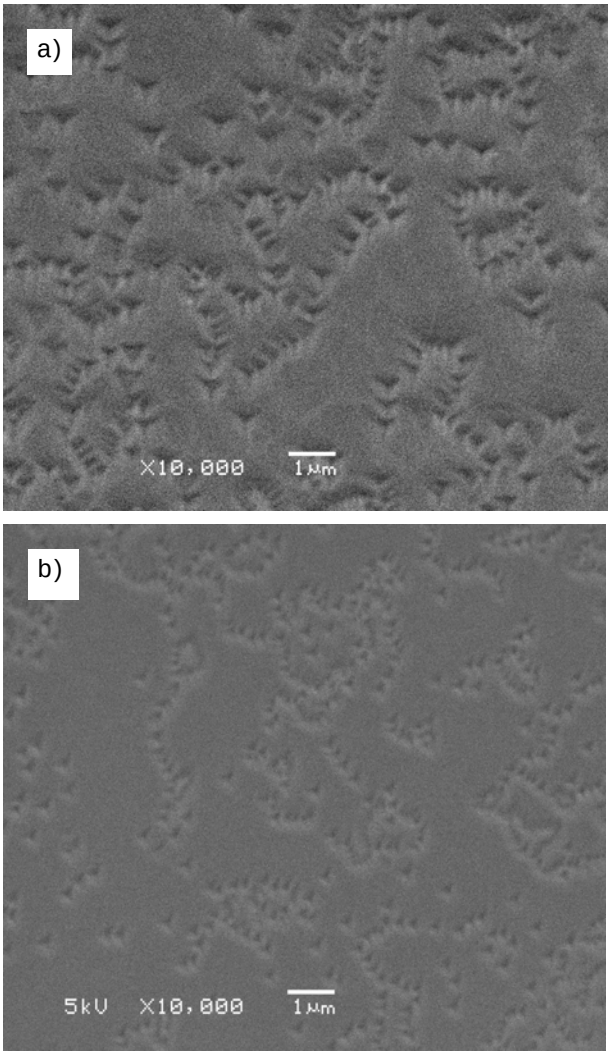

Fig. 3.15 SEM images of etch pits (a) in traditional growth (PbSe on CaF_2/Si) and (b) in optimized growth (after *in-situ* surface treatment), both in etchant for 5 minuets at 75 ^{0}C.

pits density, as characterized by scanning electron microcopy (SEM) in **Fig. 3.15 (a) and Fig. 3.15 (b),** reduces from a level of 2×10^{8} cm^{-2} to 5×10^{7} cm^{-2} due to the surface treatment. Moreover, the *in-situ* surface treatment helps in increasing the mobility of majority carrier from 9,875 cm^2/V.s (carrier concentration: 8.0×10^{16} cm^{-3}) to 29,912 cm^2/V.s (carrier concentration: 7.2×10^{16} cm^{-3}) at 77K and from 647 cm^2/V.s (carrier concentration: 2.0×10^{17} cm^{-3}) to 1,073 cm^2/V.s (carrier concentration: 1.7×10^{17} cm^{-3}) at 300K. As we know, the detectivity of the detectors is limited by the threading dislocation and the carrier lifetime is mainly determined by the mobility. It is, therefore, highly expected that the IV-VI device performance would increase significantly by using these improved MBE-grown epilayers.

3.2.6 Water-resist

Another phenomena observed during the experiments is that water-resistence becomes weak if the CaF_2 buffer layer is too thick (over 50 angstrom). For example, the surface of a sample named by Si38608 with 50 angstrom CaF_2 buffer layer became rough when it was placed in DI water for 24 hours (**Fig. 3.16 (b))** compared to the as-grown one in Fig. **3.16 (a)** , but the epilayer with 20 angstrom

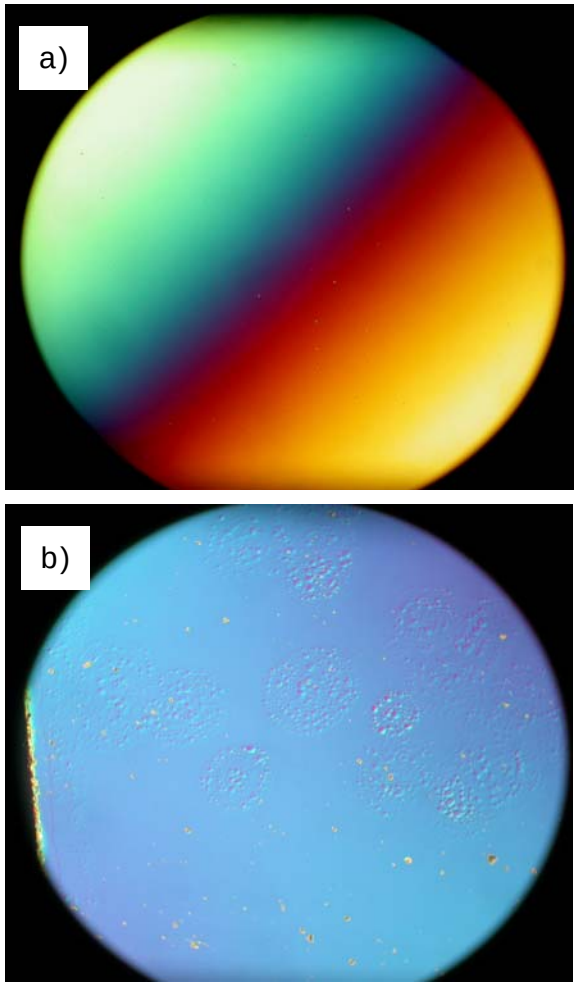

Fig. 3.16 Nomarski images of surface: (a) as-grown sample Si38608 (b) Samples Si38608 in DI water for 24 hours

CaF_2 buffer layer did not change in DI water for 24 hours or longer. We thought that a persuasive explanation is: the function of the buffer CaF_2 layer becomes weak when the thickness of the buffer layer is higher than the critical thickness of silicon and CaF_2 at growth temperature. Normally if the thickness of a buffer layer is within the critical thickness between the layers, then the buffer layer serves as an elastic strain layer, so the extra stress may be released by this layer. Otherwise, if the thickness of the buffer layer is much thicker than the critical thickness, the buffer layer (actually, this layer does not work as the buffering function any longer) just grows as itself crystal structure and therefore it loses its adjustment between bottom and top layers. The other mechanism regarding this result is still in study.

3.2.7 Conclusions of *In-situ* Surface Treatment

In summary, by applying a surface treatment method on CaF_2/Si, the quality of IV-VI epilayer increases considerably. The reduction of growth pits and etch pits densities in the epilayer by this optimized surface treatment method is roughly three-fold and four-fold respectively. This is extremely valuable for the IV-VI midinfrared detector applications. Meanwhile, the improvement in carrier mobility is more than three-fold at 77K and two-fold at room temperature respectively. As is shown in this chapter, the preliminary results are very encouraging and could lead to significant progress in future device performance of IV-VI materials. The impact of this procedure with respect to additional performance factors related to device operation is an ongoing research and will be provided in future.

3.3 References

[1] V. H. Mendez-Garcia, M. Lopez-Lopez, *Journal of Crystal Growth* **210/202**, 518 (1999).

[2] L. T. Romano, J. Knall, R. D. Bringans and D. K. Biegelsen, *Appl. Phys. Lett.* **65**, 869 (1994).

[3] R. D. Bringans, D. K. Biegelsen, L. E. Swarts, F. A. Ponce and J. C. Tramontana, *Phys. Rev*. B **45**, 13400 (1992).

[4] W. A. Harrison, E. A. Kraut, J. R. Waldrop and R. W. Grant, *Phys. Rev.* B **18**, 4402 (1978).

[5] R. M. Park and H. A. Mar, *Appl. Phys. Lett.* **48**, 529 (1986).

[6] R. D. Bringans and M. A. Olmstead, *Phys. Rev.* B **39**, 12985 (1989).

[7] L. T. Romano, R. D. Bringans, J. Knall, D. K. Biegelsen, A. García and J. E. Northrup, *Phys. Rev.* B **50**, 4416 (1994).

[8] R. M. Park, *J. Vac. Sci. Technol.* **A 10**, 701 (1992).

[9] S. L. Elizondo, F. Zhao, J. Kar, J. Ma, J. Smart, D. Li, S. Mukherjee, and Z. Shi, *J. Electron. Mater.,* online first (2008).

[10] H. Zogg, S. Blunier, T. Hoshino,C. Maissen, J. Masek, and A. N. Tiwari, *IEEE Trans. Electron Devices* **38,** 1110 (1991).

[11] H. Zogg, *Appl. Phys. Lett*. **49**, 933 (1986).

[12] H. Zogg, A. Fach, J. John, J. Masek, P. Müller, and C. Paglino, Narrow Gap Semiconductors 160(1995), Institute of Physics Publishing Ltd., London (1995).

[13] P. J. McCann, X. M. Fang, W. K. Liu, B. N Strecker, and M. B. Santos, *Journal of Crystal Growth* **175/176,** 1057 (1997).

[14] P. Müller, A. Fach, J. John, A. N. Tiwari, H. Zogg, and G. Kostorz, *Journal of Applied Physics* **79,** 1911 (1996).

[15] H. Z Wu, X. M. Fang, D. McAlister, R. Salas, Jr., and P. J. McCann, *Journal of Vacuum Science and Technology* **B 17,** 1263 (1999).

[16] H. Zogg, *SPIE* **3629,** 52 (1999).

[17] G. Springholz, H. Zogg, and Z. Shi, in: Thin Films: Heteroepitaxial Systems, edited by W. K. Liu and M. B. Santos (World Scientific, Singapore, 1999), pp. 621–688.

[18] C. Gautier, G. Breton1, M. Nouaoura1, M. Cambon1, S. Charar1 and M. Averous, *Thin Solid Films* **315,** 118 (1998).

[19] M. Tacke, *Infrared Phys. Technol.* **36**, 447 (1995).

Chapter Four

Single Element Mid-Infrared PbSnSe Detector on CaF_2/Si (111)

4.1 Narrow Band-gap Mid-Infrared Photodetectors

At present, efforts in infrared (IR) detector research are directed towards improving the performance of single element devices and large electronically scanned arrays, and to obtain higher operating temperature of detectors. Another important goal is to make IR detectors cheaper and more convenient to use. Recent progress in different IR photodetector technologies includes: HgCdTe (MCT) photodiodes, InSb photodiodes, alternative to HgCdTe, III-V and II-VI ternary alloy photodiodes, and monolithic IV-VI (lead chalcogenide) photodiodes. Investigations of the performance of photodiodes operated at short wavelength IR (SWIR), 1-3 μm; medium wavelength IR (MWIR), 3-5 μm; and long wavelength IR (LWIR), 8-14 μm; are carried out and discussed in this chapter.

4.1.1 Introduction of Narrow Gap Detectors

The years during World War II saw the origins of modem infrared (IR) detector technology. Recent success in applying IR technology to remote sensing problems has been made possible by the successful development of high-performance IR detectors over the last six decades. Many materials have been investigated in the IR field. Spectral detectivity curves for a number of commercially available IR detectors are shown in **Fig. 4.1**.[1] Interest has centered primarily on the wavelengths of the two atmospheric windows 3-5 μm and 8-14 μm, though in recent years there has been increasing interest in longer wavelengths stimulated by space applications.

During the 1950s IR detectors were built using single-element-cooled lead salt detectors, primarily for anti-air-missile seekers. Usually lead salt detectors were polycrystalline and were produced by vacuum evaporation and chemical deposition from a solution, followed by a post-growth sensitization process.[2] The first extrinsic

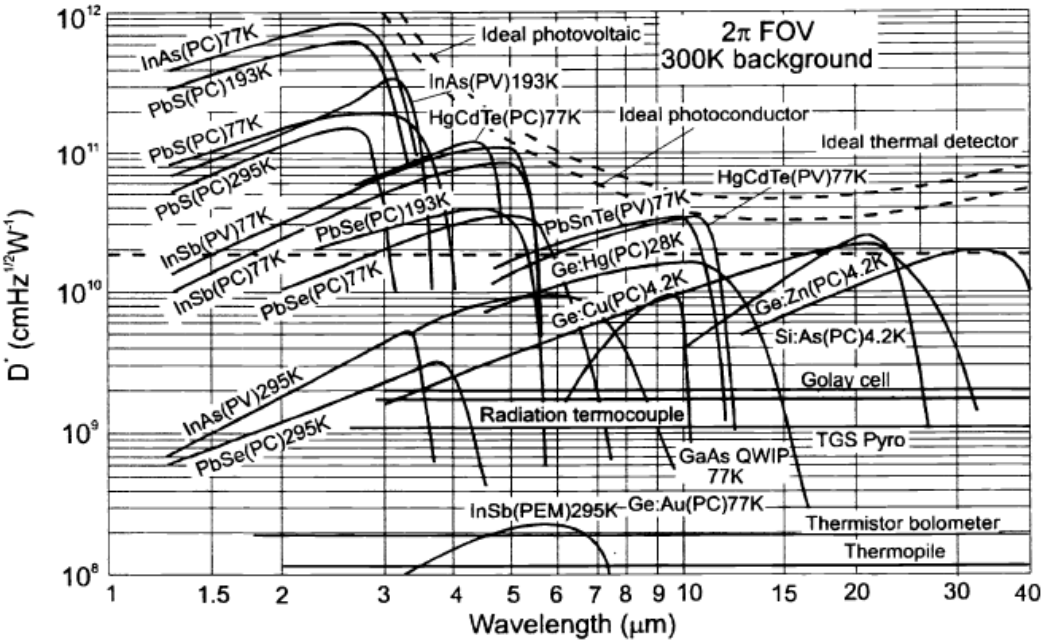

Fig. 4.1 Comparison of the D* of various commercially available infrared detectors when operated at the indicated temperature. Chopping frequency is 1000 Hz for all detectors except the thermopile (10 Hz), thermocouple (10 Hz), thermistor bolometer (10 Hz), Golay cell (10 Hz) and pyroelectric detector (10 Hz). Each detector is assumed to view a hemispherical surround at a temperature of 300 K. Theoretical curves for the background-limited D* for ideal photovoltaic and photoconductive detectors and thermal detectors are also shown. Adapted from Rogaiskia *et al.*

photoconductive detectors were reported in the early 1950s. Since the techniques for controlled impurity introduction became available for germanium at an earlier date, the first high performance extrinsic detectors were based on the use of germanium. Extrinsic photoconductive response from copper, zinc, and gold impurity levels in germanium made devices possible in the 8- to 14- μm long wavelength spectral window (LWIR) and beyond to the 14- to 30- μm very long wavelength region (VLWIR). The extrinsic photoconductors were widely used at wavelengths beyond 10 μm, prior to the development of the intrinsic detectors. They must be operated at lower temperatures to achieve performance similar to that of intrinsic detectors, and a sacrifice in quantum efficiency is required to avoid impracticably thick detectors.

At the same time, rapid advances were being made in narrow bandgap semiconductors that would later prove useful in extending wavelength capabilities and improving sensitivity. The first such material was InSb, a member of the III-V compound semiconductor family. The semiconductor alloys in III-V, IV-VI and II-VI material systems were introduced by the end of the 1950s. **Table III and IV** listed

Material	E_g (eV)		n_i (cm^{-3})		ε	μ_e (10^4 cm^2/Vs)		μ_h (10^4 cm^2/Vs)	
	77 K	300 K	77 K	300 K		77 K	300 K	77 K	300 K
InAs	0.414	0.359	6.5×10^3	9.3×10^{14}	14.5	8	3	0.07	0.02
InSb	0.228	0.18	2.6×10^9	1.9×10^{16}	17.9	100	8	1	0.08
$In_{0.53}Ga_{0.47}As$	0.66	0.75		5.4×10^{11}	14.6	7	1.38		0.05
PbS	0.31	0.42	3×10^7	1.0×10^{15}	172	1.5	0.05	1.5	0.06
PbSe	0.17	0.28	6×10^{11}	2.0×10^{16}	227	3	0.10	3	0.10
PbTe	0.22	0.31	1.5×10^{10}	1.5×10^{16}	428	3	0.17	2	0.08
$Pb_{1-x}Sn_xTe$	0.1	0.1	3.0×10^{13}	2.0×10^{16}	400	3	0.12	2	0.08
$Hg_{1-x}Cd_xTe$	0.1	0.1	3.2×10^{13}	2.3×10^{16}	18.0	20	1	0.044	0.01
$Hg_{1-x}Cd_xTe$	0.25	0.25	7.2×10^8	2.3×10^{15}	16.7	8	0.6	0.044	0.01

Table III. Some physical properties of narrow gap semiconductors

important electrical and optical parameters of the materials used in IR detectors fabrication. These alloys allowed the bandgap of the semiconductor and hence the

Material	lattice constant Å	thermal expansion coefficient at 300K 10^{-6} /K	band gap energy eV	cut-off wavelength μm	low frequency permittivity
Si	5.431	2.6	1.1	1.1	
CaF_2	5.46	19.1	>>1		
SrF_2	5.80	18.4	>>1		
BaF_2	6.20	19.8	>>1		
PbS	5.94	20.3	0.42	3.0 (300K)	172
			0.31	4.0 (77K)	184
PbTe	6.46	19.8	0.31	4.0 (300K)	380
			0.22	5.6 (77K)	428
PbSe	6.12	19.4	0.27	4.6 (300K)	206
			0.18	7.0 (77K)	227
$PbS_{1-x}Se_x$ (x=0-1)	5.94-6.12		0.42 - 0.18	3 - 7	
$Pb_{1-x}Eu_xSe$ (x=0-≈.02)	6.12		0.18 - 0.42	7 - 3	
$Pb_{1-x}Sn_xSe$ (x=0-≈.2)	6.12-6.06		0.18 - 0	7 - ∞ (77K)	
$Pb_{1-x}Sn_xTe$ (x=0-≈.4)	6.46-6.40		0.22 - 0	5.6 - ∞ (77K)	
$Cd_{1-x}Hg_xTe$ (x=0-≈.87)	6.48-6.46	5.0	1.6 - 0	0.8 - ∞	18

Table IV Some material properties of narrow-gap semiconductors for IR sensor application.

spectral response of the detector to be custom tailored for specific applications. In

1959, research by Lawson and co-workers triggered development of variable bandgap HgCdTe alloys, which provided an unprecedented degree of freedom on infrared detector design.[3]

4.1.2 Theory of Infrared Photodetectors

The photodetector is a slab of homogeneous semiconductors with the actual electrical area A_e that is coupled to a beam of infrared radiation by its optical area A_o. Generally, the optical and electrical areas of the device are the same or close. The use of optical concentrators can increase the A_o/A_e ratio. Detectivity D* as the main parameter characterizing normalized signal to noise performance of detectors is equal [4 5]

$$D^* = \frac{\lambda}{hc}\left(\frac{A_o}{A_e}\right)^{1/2}\eta[2(G+R)t]^{-1/2} \qquad (1)$$

For a given wavelength and operating temperature, the highest performance can be obtained by maximizing $\eta/[t(G+R)]^{1/2}$. This means that high quantum efficiency must be obtained with a thin device. Assuming a single pass of the radiation and negligible frontside and backside reflection coefficients, the highest detectivity can be obtained for $t = 1.26/\alpha$.[6] In this optimal case $\eta = 0.716$ and detectivity is equal

$$D^* = 0.45\frac{\lambda}{hc}\left(\frac{\alpha}{G+R}\right)^{1/2}. \qquad (2)$$

To achieve a high performance the thermal generation must be suppressed to possible the lowest level. This is usually done with cryogenic cooling of the detector.

$$D^* = 0.31\frac{\lambda}{hc}\left(\frac{\alpha}{G}\right)^{1/2} \qquad (3)$$

For practical purposes, the ideal situation occurs when the thermal generation is reduced below the optical generation. At equilibrium the generation and recombination rates are equal, and then we have

The ratio of absorption coefficient to the thermal generation rate α/G is the fundamental figure of merit of any material for infrared photodetectors which directly determines the detectivity limits of the devices. An optimized photodetector of any type should consist of the following regions (see **Fig. 4.2**): (1) Lightly-doped narrow gap semiconductor region, which acts as an absorber of IR radiation. Its band gap, doping and geometry should be selected. (2) Electric contacts to the narrow gap region which sense optically generated charge carriers. Contacts should not contribute to the dark current of the device. (3) Passivation of the narrow gap region. The surfaces of the absorber regions must be insulated from the ambient by a material, which also does not contribute to the generation of carriers. In addition, the carriers, which are optically generated in absorber, are kept away from surfaces, where recombination can reduce the quantum efficiency. For the best sensitivity the frontside face should perfectly transmit IR radiation. (4) Refractive, reflective or diffractive concentrator of IR radiation. (5) Backside minor for double pass of IR radiation.

In real case, such device can be obtained using 3-dimensional gap and doping

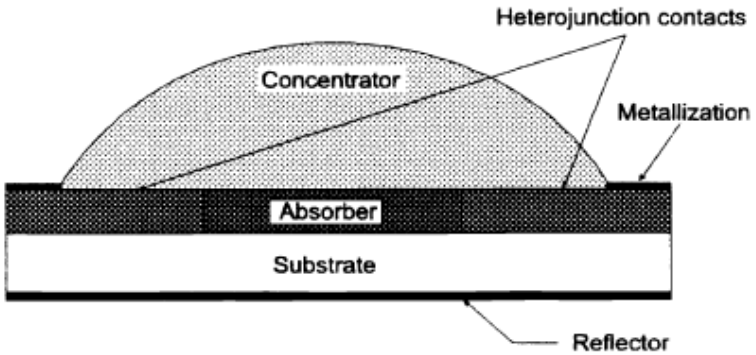

Fig. 4.2 Schematic of 3-D heterostructure photodetector. Taken from Piotrowski *et al*

engineering, with the narrow gap absorber buried in a wide gap semiconductor. The undoped wide gap material can be used as a window, and/or a concentrator of incoming radiation. Doped n- and p-type semiconductors are used for contacts. The device must be also supplied with contact metallization and electrodes. Thermal generation in the contact regions is virtually eliminated by making them wide gap.

The generation-recombination (G-R) processes are associated with the predominant recombination mechanisms. There are three important generation and recombination mechanisms: Shockley-Read, radiative, and Auger mechanisms. The Shockley-Read mechanism occurs via lattice defects and impurity energy levels within the forbidden energy gap. These mechanism sets can be controlled by the procedure used to grow the material; consequently, the Shockley-Read process is not a fundamental limit to the performance of the detector. The radiative generation-recombination and Auger mechanisms are fundamental band-to-band processes, which are determined by the electronic band structure of the semiconductor. It appears that Auger mechanisms dominate generation and recombination processes in high-quality narrow gap semiconductors. The generation rate due to the Auger 1 and Auger 7 processes can be described as [7]

$$G_A = \frac{n}{2\tau^i_{A1}} + \frac{p}{2\tau^i_{A7}} = \frac{1}{2\tau^i_{A1}}\left(n + \frac{p}{\gamma}\right) \qquad (4)$$

where τ^i_{A1} and τ^i_{A7} are the intrinsic Auger 1 and Auger 7 recombination times. Then Auger dominated detectivity is equal [see Eq. (1)]

$$D^* = \frac{\lambda}{2^{1/2} hc} \frac{\eta}{t^{1/2}} \left(\frac{\tau^i_{A1}}{n + p/\gamma}\right)^{1/2} \qquad (5)$$

where $\gamma = \tau^i_{A7} / \tau^i_{A1}$. Since the resulting Auger generation rate achieves its minimum for $p = \gamma^{1/2} n_i$, it leads to important conclusion about optimum doping. The optimal

performance of Auger limited detectors can be achieved with a lightly p-type doping with hole concentration $p = \gamma^{1/2} n_i$.

Assuming that the saturation dark current I_s of a photodiode is only due to thermal generation in the base layer and that its thickness is low compared to the diffusion length, then we have

$$I_s = qGAt \tag{6}$$

where G is the generation rate in the base layer. Because the zero bias resistance-area product is

$$R_oA = \frac{kTA}{qI_s} \tag{7}$$

so

$$R_oA = \frac{kT}{q^2Gt} \tag{8}$$

Taking into account the Auger 7 mechanism in extrinsic p-type region of n^+-on-p photodiode, we get

$$R_oA = \frac{2kT\tau^i_{A7}}{q^2N_at} \tag{9}$$

And the same equation for p-on-n photodiode

$$R_oA = \frac{2kT\tau^i_{A1}}{q^2N_dt} \tag{10}$$

where N_a and N_d are the acceptor and donor concentrations in the base region, respectively. By now, photodiodes were only analyzed in which the dark current was limited by diffusion. However, several additional mechanisms are involved in determining the dark current-voltage (I-V) characteristics of the photodiode. The dark current is the superposition of current contributions from three diode regions: bulk,

depletion region and surface. If we are concerned with the current contribution of high-quality photodiodes with high R_oA products limited by: (1) generation-recombination within the depletion region, (2) tunneling through the depletion region, (3) surface effects, then we will get the following equations. The first two

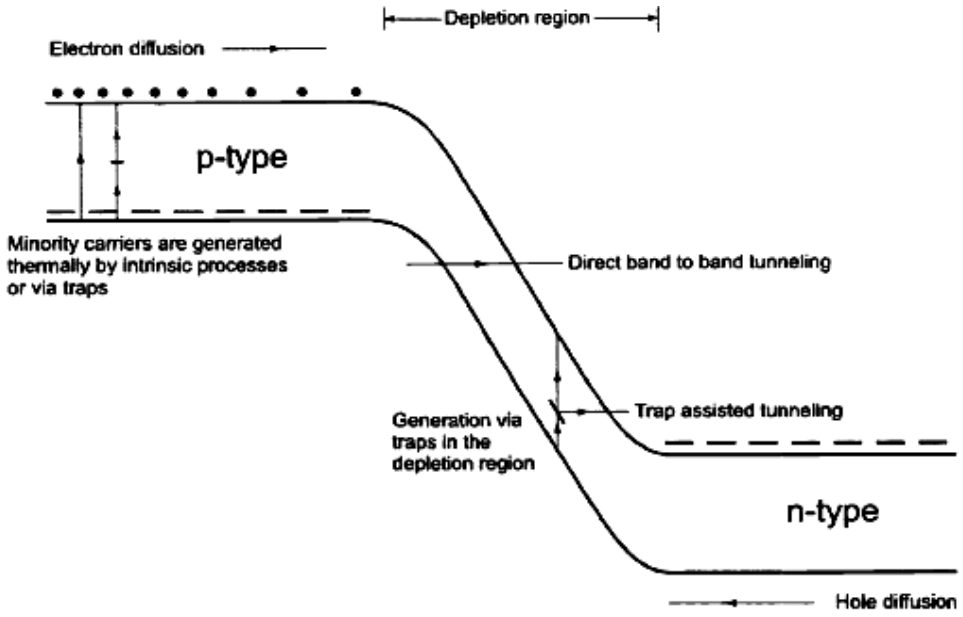

Fig. 4.3 Schematic representation of some of the mechanisms by which dark current is generated in a reverse biased p-n junction. From online publication

mechanisms are schematically illustrated in **Fig. 4.3.**

The generation-recombination current of the depletion region can be described as

$$J_{GR} = \frac{qwn_i}{\tau_o} \qquad (11)$$

if a trap is near the intrinsic level of the band gap energy. In this equation τ_o is the carrier lifetime in depletion region. The surface leakage current can be described in the same way.

The space-charge region generation-recombination current varies with temperature as n_i, i.e., less rapidly than diffusion current which varies as n_i^2.

The zero bias resistance can be found by differentiating Eq. (11) and setting V = 0:

$$(R_oA)_{GR} = \left(\frac{dJ_{GR}}{dV}\right)^{-1}_{|V=0} = \frac{2V_b\tau_o}{qn_iw} \qquad (12)$$

where $V_b = kT\ln(N_aN_d/n_i^2)$. In evaluating Eq. (12), the term of greatest uncertainty is τ_o.

The third type of dark current component that can exist is a tunneling current caused by electrons directly tunneling across the junction from the valence band to the conduction band (direct tunneling) or by electrons indirectly tunneling across the junction by way of intermediate trap sites in the junction region (indirect tunneling or trap-assisted tunneling - see **Fig. 4.3**).

The tunneling current (and R_oA product) is critically dependent on doping concentration. **Fig. 4.4** shows the dependence of the R_oA product components on the doping concentrations for one-sided abrupt HgCdTe, PbSnTe and PbSnSe photodiodes at 77 K (Eg ~ 0.1 eV). To produce high R_oA products for HgCdTe and lead salt photodiodes, the doping concentration of 10^{16} cm^{-3} and 10^{17} cm^{-3} (or less) are required, respectively. The maximum available doping levels due to onset of tunneling are

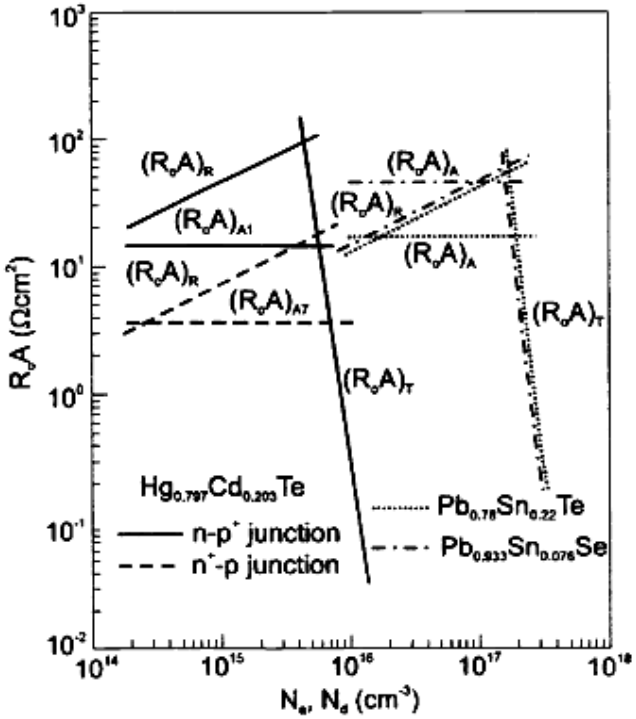

Fig. 4.4 The dependence of the R_oA product on doping concentration for one-sided abrupt HgCdTe, PbSnTe and PbSnSe photodiodes at 77 K (Eg ~ 0.1 eV). (see Ref 11).

more than an order of magnitude higher with IV-VI than with HgCdTe photodiodes. This is due to their high permittivities ε because tunneling contribution of the R_oA product contains exp [const $(m^* \varepsilon / N)^{1/2} E_g$] factor. [8]

4.1.3 IV-VI Photovoltaic Infrared Devices

The first photovoltaic IV-VI IR-detectors were fabricated in 1970 by Holloway et al. [9] [10] in layers grown on BaF_2 (111) substrates (lattice mismatch 4% versus PbTe). They were of the Schottky barrier type with Pb evaporated as a blocking contact on p-PbTe. Pb inverts the surface region, so the barrier height approximately corresponds to the band-gap. The devices fabricated on Si-substrates follow the same technique. The first devices on Si were demonstrated in 1985 [11] [12] using a CaF_2/BaF_2 buffer layer and HWE (hot wall epitaxy) for growth of lead salt. Currently, the Pb-salt devices are grown in a MBE system with CaF_2 buffer layers.

4.1.4. Comparison of IV-VI with Other Narrow-gap Detectors

The theoretical ultimate sensitivities are almost the same for the different narrow gap semiconductor families like HgCdTe or lead-salts under similar conditions (such as bandgap, operation temperature, etc). Both MCT and lead salt (mainly PbSnSe, PbSnTe) technologies were developed for IR-sensor applications with comparable efforts until to the end of the 1970s. [13] At that time, it was decided that it did not make sense to develop two materials in parallel, and then the IV-VI were given up. Reasons for this decision were the large permittivities of the IV-VI which make the devices slower, the large thermal expansion coefficient of IV-VI which makes the hybrid connection to Si more difficult, and because bulk IV-VI materials are extremely soft which make the processing more difficult. While this decision might have been right

at that time when mainly scanning systems were anticipated, these arguments no longer hold for staring arrays with photovoltaic sensors today. Moreover, one might argue in retrospect that the decision was unfortunate since it turned out that MCT was extremely difficult to develop and has some drawbacks. IV-VI detector arrays are able to compete with MCT in each of the important aspects[14]: The material technology is much easier with IV-VI than with MCT, and IV-VI detectors can withstand higher temperatures.

As stated in introduction, the thermal expansion mismatch does not impede fabrication of high quality layers and IR-detectors on Si (l11) substrates. The high permittivities of IV-VI still do not pose problems with speed for staring FPA, but have the advantage to shift the optimal carrier concentrations for photodiodes (the sensitivity is ultimately limited by Auger recombination) to near two decades higher values than in MCT. These rather high doping levels are easily controlled. In addition, the high permittivities shield the electric field of charged defects. Higher quality devices are therefore obtained in lower quality material. The optical absorption is strong enough in IV-VI with 1-2 μm thickness to obtain a near reflection loss limited quantum efficiency.

Up to date, the quality of the IV-VI devices was still limited by the rather high dislocation densities in the high 10^7 to 10^8 cm^{-2} range. It is surprising that devices at these high dislocation levels still work satisfactorily, although their performance is far below their theoretical limitation under most operation conditions. With a dislocation density $p = 2*10^7 cm^{-3}$, the theoretical sensitivity limit for PbTe Schottky barrier detectors was obtained down to 150K. By fabricating devices into layers with $p = 1*10^6 cm^{-3}$, the theoretical sensitivity limit would be obtained down to 80K for e.g. PbSe Schottky barrier sensors.[15] For PbTe p-n junctions, the theoretical performance

(diffusion limit) is higher than with Schottky barrier devices; with a similar dislocation density ($1*10^6$ cm^{-3}), the diffusion limit would be followed down to about 180K. Therefore, a rather small effort would suffice to make IV-VI-on-Si sensor arrays operating at the theoretical sensitivity limit under many operation conditions, and hence technically even competitive to the best presently available techniques.

Moreover, concerning manufacturability, homogeneity, and costs, photovoltaic IV-VI sensor arrays on Si substrates offer substantial advantages compared to MCT. Material technology is much easier: MBE growth is straightforward and already in routine use for laser fabrication. No Hg-related problems occur, and material stability and diffusion is no problem in IV-VI. The bandgap of $Pb_{1-x}Sn_xSe$ depends much less on x than in $Hg_{1-x}Cd_xTe$, much higher uniformities in cutoff wavelength are therefore achievable. For example, the cutoff wavelength of a nominally 0.1 eV $Pb_{1-x}Sn_xSe$ sensor (12.4 μm cutoff) depends five times less on chemical composition x than in $Hg_{1-x}Cd_xTe$. This is because at x =0, PbSe is already narrow gap, whereas Eg is as high as 1.6 eV in CdTe. In addition, there is no need for very low residual impurity levels because the optimal carrier concentration for photovoltaic detectors is as high as in the low 10^{17} cm^{-3} range.

4.2 PbSnSe Single-element Detectors on Si

4.2.1 Design and Growth of Detector Structure

The detector consists of 4.5 μm p-type PbSnSe layer with carrier concentration of 1.3×10^{17} cm^{-3} and 0.5 μm n-type (bismuth doped) PbSnSe layer (**see Fig. 4.5**) with carrier concentration of 2.0×10^{18} cm^{-3}. The designed absorption wavelength at 77K is 10 μm. Single element detectors are formed by the square absorption areas with size

variable from 100×100 μm^2 to 500×500 μm^2. The gap between n-type contact and p-type contact is 10μm. The process undertakes photolithography, wet etching, surface passivation and formation of Ohmic contact, wire bonding, etc. Before growth of devices, a set of photo-masks for detectors processing were designed and fabricated according to the future detector structure.

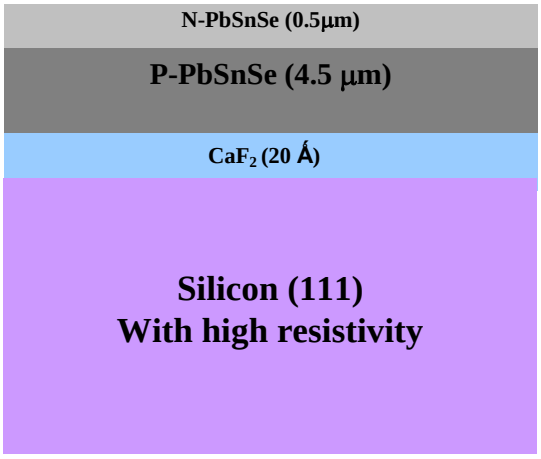

Fig. 4.5 schematic of designed PbSnSe infrared detector structure on CaF_2/Si(111)

The growth of epilayers is performed under ultra-high-vacuum (~ 10^{-10} Torr) MBE system in our research group; this MBE chamber is specially designed and machined for IV-VI materials growth. A 3-inch Si(111) wafer with high resistivity was treated by modified Shiraki method and dried by high-purity nitrogen gas. The Si substrate was outgassed in the buffer chamber at 200 ^oC for 2 hours and then transferred to the subsidiary MBE chamber for growth of buffer layer of CaF_2. A thin layer of CaF_2 was deposited on the dioxided Si surface at high substrate temperature. The Pb-salt materials were deposited in the main MBE chamber. For $Pb_{1-x}Sn_xSe$, the flux ratio of a PbSe and SnSe source determines x, and an additional Se source is used to adjust the carrier concentration to p-type in the low 10^{17} cm^{-3} range. In our

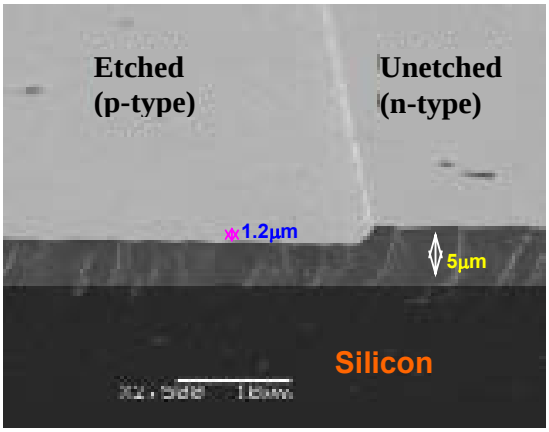

Fig. 4.6 SEM image of P-N junction after wet etch. The etched surface is comparable to the unetched one.

case, the flux ratio of SnSe and PbSe is kept to 5%, and the ratio of Se and PbSe is 10%. Substrate temperatures are maintained at 420 °C, growth rates are around 2 μm/h, and epilayer thicknesses are estimated by beam flux for 5 μm.

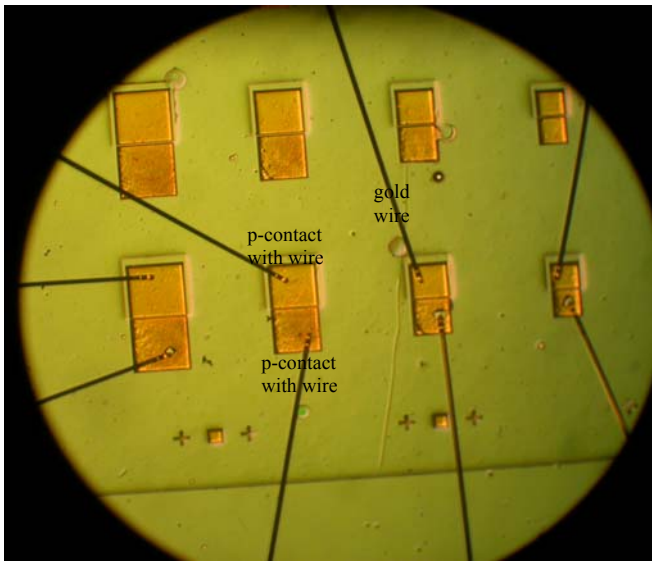

Fig. 4.7 Nomarski images of Etched mesa structures and wire-bonding on P- and N contacts

After growth, the sample was annealed in MBE chamber for 48 hours at 200 °C for reducing dislocation density and improving the surface morphology of epilayer. When temperature is down to room temperature, the sample was taken out for post-growth processing. At this stage, several standard processes were conducted on sample toward device fabrication.

A mesa structure was etched in ultrasonic bath as shown in **Fig. 4.6**. From the figure one can clearly see that the etched surface (P-type side) is comparable to the unetched surface (N-type side). The smooth and uniform surface results from our optimal etching approaches, which is important for the subsequent processing. A mesa

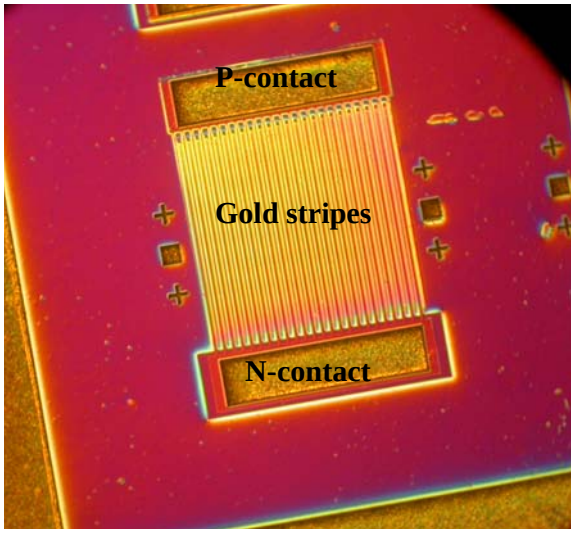

Fig 4.8 Nomarski image of comb structure of detector after electroplating of gold for Ohmic contact

structure was followed by the second lithography for gold electroplating. **Fig. 4.7** shows that the Ohmic contacts (p-type and n-type) were made by electroplating gold on the photoresist windows. The comb structures were also made at the same experimental processing as shown in **Fig. 4.8. Fig 4.9** is partially enlarged from Fig. 4.8, which clearly illustrates the comb structure with p- and n- contacts. In the **Fig. 4.9,** the widths of p- and n- contact stripes are 10 μm and the gap between p- and n- type is 10 μm too.

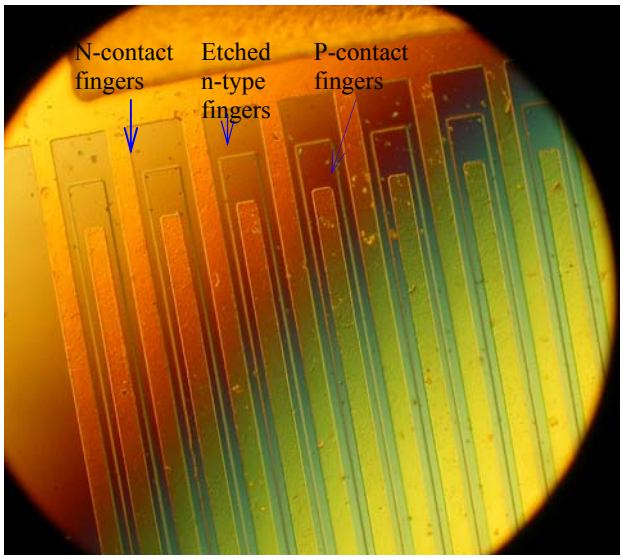

Fig. 4.9 Nomarski image of partially enlarged comb structure after gold electroplating (see Fig 4.8)

The gold wires were bonded by wire–bonding processing as seen in **Fig. 4.7**. The different sizes of the contacts were made in one chip, which indicates tens of the single element detectors can be made at the same time. The current-voltage (I-V) curves in

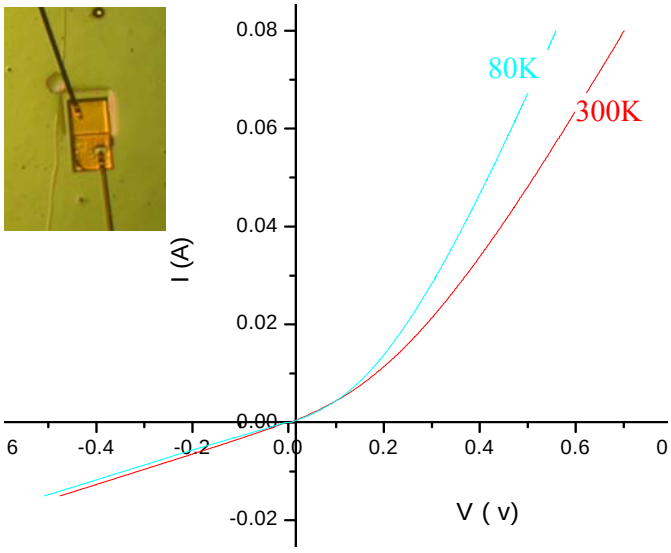

Fig.4.10 I-V characteristics of P-N junction made by improved PbSe epilayer on CaF_2/Si (111) heterostructure (N-type doped by Bi~2.0 x 10^{18} cm^{-3})
Inset: single element detector after processing (etching, Ohmic contact, passivation, wire bonding, etc)

Fig. 4.10 shows the characteristic of the fabricated P-N junction in **Fig. 4.7**. In **Fig. 4.10** the contact sizes of p- and n- type are 200 × 200 μm^2 and the gap between p- and n- contacts is 10 μm. The threshold voltage of the P-N junction is around 0.15 volts and forward current-voltage response is comparable to that of II-VI detectors.[16] The leakage current, however, is still high in reverse bias (two magnitudes higher than that of the II-VI detectors), so the performance of the P-N junction still needs to be enhanced by further improving the material quality and device fabrication technique.

In the future, it is expected that the linear or two-dimensional arrays of PbSnSe photovoltaic detectors will be fabricated on Si chips that contain the complete readout circuits as illustrated in **Fig. 4.11**. Currently, the readout circuit is fabricated in complementary metal-oxide semiconductor (CMOS) technology on Si (111) chips. A fanout is insulated by polymers or fluoride layer. Illustration is from the backside through the IR-transparent buffer layers and Si substrate. According to our theoretical calculation, an optimal detector structure will be applied by changing detector profiles,

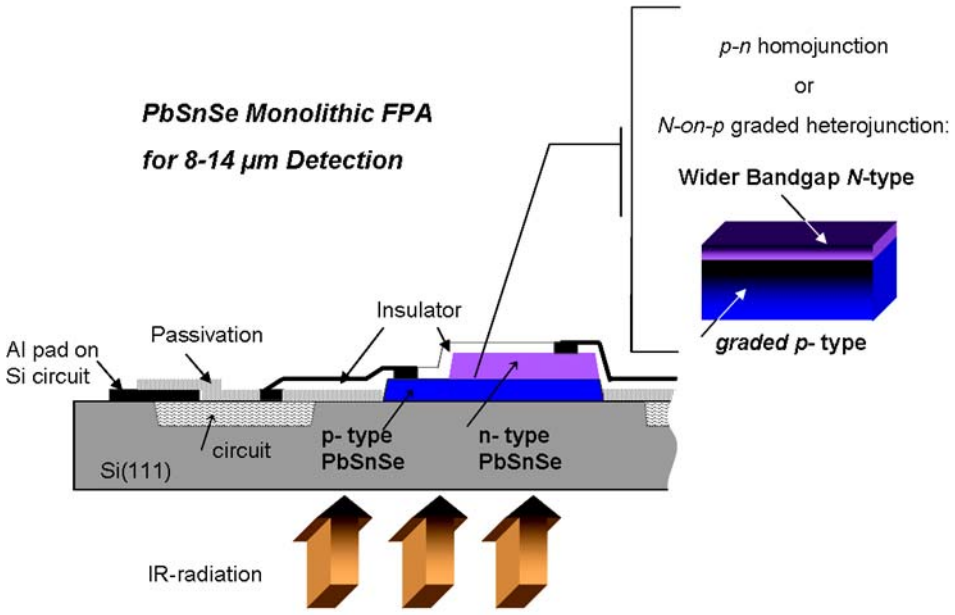

Fig 4.11 Designed PbSnSe monolithic FPAs on silicon for mid-infrared detection in the future

which includes the graded p-type PbSnSe layer and the wide bandgap confinement layers. In this procedure, The highest temperature of all materials growth and device fabrication have to controlled below 450 ^{o}C because of aluminum metallization (standard integrated circuit technology).

4.3 References

[1] A. Rogalski, *opto-Elctro. Rev*. **5,** 3 (1997).

[2] R. J. Cushman, *Proc. IRE* **47**, 1471 (1959).

[3] D. Lawson, S. Nielson, E. H. Putley and A. S. Young, *J. Phys. Chem. Solids* **9**, 325 (1959).

[4] A. Rose, *Concepts in photoconductivity and Allied Problems*, Interscience, New York, (1963).

[5] J. Piotrowski, in Infrare Photon Detectors, Edited by A. Rogalski, optical Engineering Press, Bellingham, 391 (1995).

[6] J. Piotrowski and W. Gawron, *Infrared Phys. Technol*. **38** 63 (1997).

[7] A. Rogalski and R. Ciupa, *J. Appl. Phys.* **77** 3505 (1995)

[8] A. Rogalski and W. Larkowski, *Electron Technology* **18** 55 (1985).

[9] E. M. logothetis, H. Holloway, A. J. Wilkes, *Appl. Phys. Lett.* **21**, 318 (1971).

[10] H. Holloway, in "physics of thin Films", Academic Press. **11**, 105 (1980).

[11] H. Zogg and M. Huppi, *Appl. Phys. Lett*. **47**, 133 (1985).

[12] H. Zogg and P. Norton, Technical Digest, Int. Electron Devices Meeting, Washington DC, Dec 1-4, 121 (1985).

[13] P.R. Norton, *Opt. Eng*. **30**, 1649 (1991).

[14] H. Zogg, S. Blunier, T. Hoshino, C. Maissen, J. Masek, AN. Tiwari, *IEEE Trans. Electron Devices* **ED38**, 1110 (1991).

[15] A. Fach, J. John, P. Muller, C. Paglino, and H. Zogg, *J. Electronic Mat.* **26**, 873 (1997).

[16] N. T. Gordon, R. S. Hall, C. L. Jones, C. D. Maxey, N. E. Metcalfe, R. A. Catchpole, and A. M. White, *J. Electron. Mater.,* **29**, 818 (2000).

Chapter Five

Edge-Emitting Lead Salt Mid-Infrared Laser Structure on BaF_2 [110] Substrate

5.1 Midinfrared Diode Lasers

Mid-infrared emissions were first demonstrated in 1963, which were from InAs and InSb p-n junction diode emitting at a wavelength of 3.1 μm[1] and 5.3μm[2] respectively. In 1964, just after one year, laser emission from PbTe p-n junction diode at a higher wavelength was reported[3]. After this demonstration of first Pb-salt laser, standard MIR lasers were fabricated from narrow gap IV-VI semiconductors such as PbS, PbTe, PbSe, PbSSe, PbSnTe, and PbSnSe in the next twenty years. These lasers were all diffused-diodes emitting in 4 – 30 μm wavelength range with an operation temperature of 4 – 77 K. As the epitaxial growth techniques advanced, new growing techniques such as liquid-phase-epitaxy (LPE), hot-wall-epitaxy (HPE), molecular-beam-epitaxy (MBE) were developed and therefore double-heterostructures (DH) (see **Fig. 5.1)** were grown. Carriers are sufficiently accumulated within the active region to induce population inversion in a double-heterojunction (DH) structure, where a thin

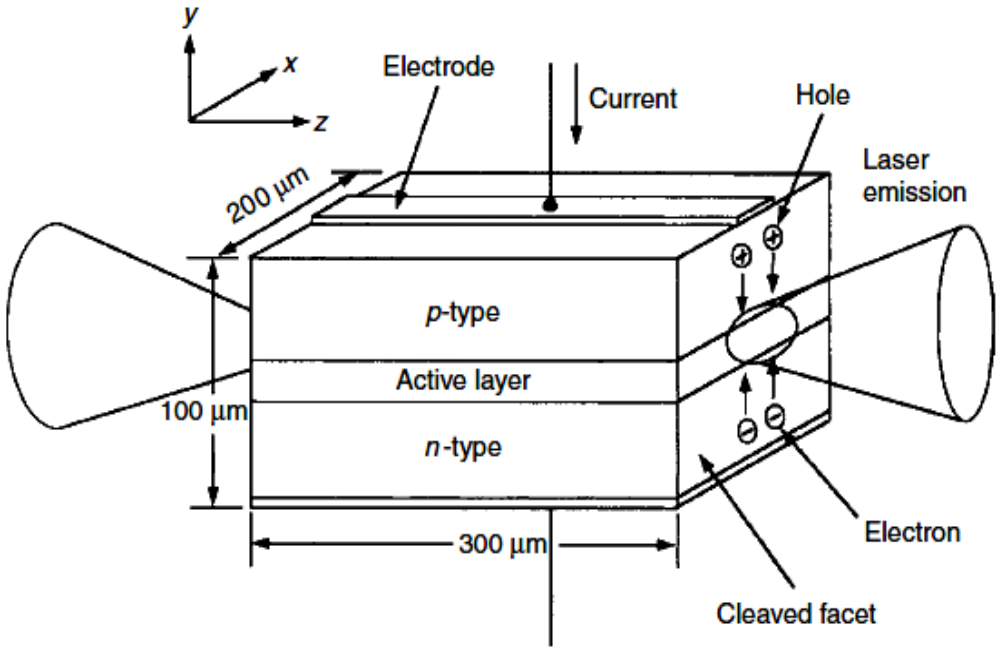

Fig. 5.1 Schematic illustration of a double-heterostructure semiconductor laser. Taken from online publication.

active layer, typically ~ 0.1 μm thick, but as thin as 10 nm in quantum well lasers, is sandwiched between *n*- and *p*-type cladding layers, which have wider band gaps than the active layer. Electrons and holes injected into the active layer through the heterojunctions are confined within the thin active layer by the potential barriers at the heteroboundaries, as illustrated in **Fig. 5.2(a**). The DH structure forms an efficient optical waveguide as well, because of the refractive-index difference between the active and cladding layers shown in **Figs. 5.2(b) and 5.2(c**). Thus, the DH structure facilitates the interaction needed for laser action between the optical field and the injected carriers.

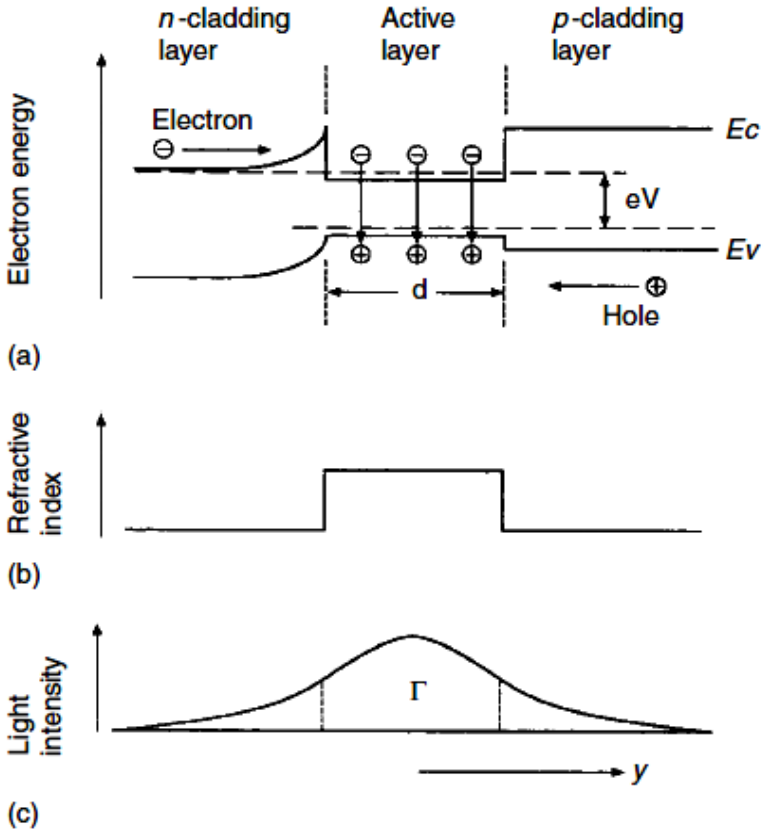

Fig. 5.2 Diagram illustrating carrier confinement and waveguiding in a double heterostructure (a) Energy-band diagram at high forward bias; (b) refractive-index distribution; (c) light intensity distribution. *E*c and *E*v: The edges of the conduction and valence bands. *V*: Applied voltage. *d*: Active-layer thickness (~0.1 μm). Γ: Confinement factor. Taken from online publication.

DH-structure made revolution in IV-VI laser performances as well. Lead-salt DH lasers remained the standard of MIR lasers still 1990. These lasers were grown on PbS, PbSe or PbTe substrates, with active layers having PbEuSSe for 3 – 4 μm[4],

PbEuSeTe or PbEuSe for 4 – 8 μm range, and PbSnTe or PbSnSe for wavelengths beyond 8 μm. During that time DH laser based on III-V materials were becoming promising candidate for MIR light source as well. AlGaAsSb/GaInAsSb/AlGaAsSb DH lasers on GaSb substrate and InAsPSb/InAsSb/InAsPSb DH lasers on InAs substrates showed excellent performance at room temperature in the 2.0 - 2.5 μm range [5] [6]. The InGaAsSb/AlGaAsSb strained multi-quantum-well (MQW) laser showed striking results in CW operation at and above room temperature and till date appears to be well-established technology for laser emission in the 2.0 - 2.7 μm wavelength range[7]. Beyond 2.7 μm, type-II quantum well lasers based on the InAs–GaSb system, III–V quantum cascade laser and IV–VI lead salt semiconductor lasers are in use[8] [9] [10].

5.2 Lead-Chalcogenide Diode Lasers

Lead chalcogenide diode lasers emitting in the MIR region have been commercially available for more than three decades. Their emission covers the wavelength range from 3μm to more than 20μm[11]. Electrically injected lead salt lasers have achieved 223K operation in continuous wave mode [12] and above-room-temperature operations in pulsed mode[13]. In the earlier stage, there was misconception regarding the incapability of IV-VI lasers to produce high output power. However, in 1997 it was reported that even a diffused-junction laser can produce up to 24 mW of CW output power[14].

5.2.1 Properties of Lead Salt Diode Lasers

Bandgap energies of IV-VI semiconductors increase with increasing temperature. Hence, they have very large temperature and current tuning ranges. The temperature

induced bandgap energy change also helps in reducing facet heating. Facet heating is a big disadvantage of III-V lasers that suffer from thermal runaway problems associated with the decrease in bandgap energy with increasing temperature [15]. Absence of facet heating in IV-VI lasers make them more reliable for high temperature operation.

Among all the previously-mentioned state of the art MIR lasers, lead salt diode lasers have the advantages of large tuning range, easy current tuning and narrow line-width. Group IV-VI materials have suppressed Auger non-radiative loss[16] [17]. Also they posses much lighter electron and hole masses that lead to further reduction of the lasing thresholds. These properties enable lead salt lasers to set and maintain the earlier records for maximum operation temperatures for both pulsed and CW operation among all mid infrared semiconductor diodes.

As can be seen in **Fig. 5.3**, the wavelength of a MIR Pb-salt diode can be easily tuned by changing the composition from 3.5 um to 10 um with high reproducibility. It is clear from **Fig. 5.4** that further fine-tuning of the bandgap by changing QW width and temperature is possible. As also can be seen in **Fig. 5.4,** the temperature tuning is about five times larger than that of III-V materials. It was mentioned before that the energy bandgap of IV-VI semiconductors increase with the

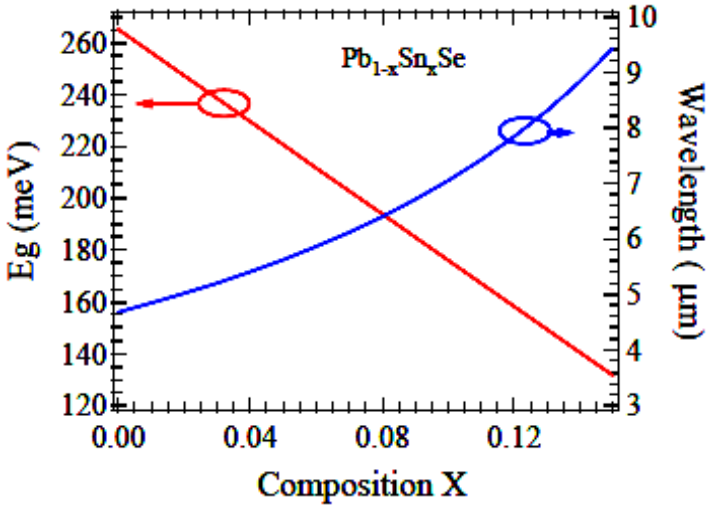

Fig 5.3 Energy band gap of PbSnSe at room temperature (Taken from Dewali's thesis, 2007)

increasing temperature. Therefore, an increment in injection current will make a blue-shift of both the gain peak and the energy band gap by Joule-heating and thus the laser emission wavelength can be easily tuned. For a number of years, lead salt diode lasers remained the only commercially available semiconductor laser emitting in the mid-infrared region. However, their performance remains far from that desired. Low thermal conductivity of IV-VI materials prevents room temperature CW operation of traditional IV-VI lasers. Also, there are issues with high dislocation density[18] (~10^6 to 10^7 cm^{-2}) as well; therefore commercially available Pb-salt lasers require cryogenic cooling presently.

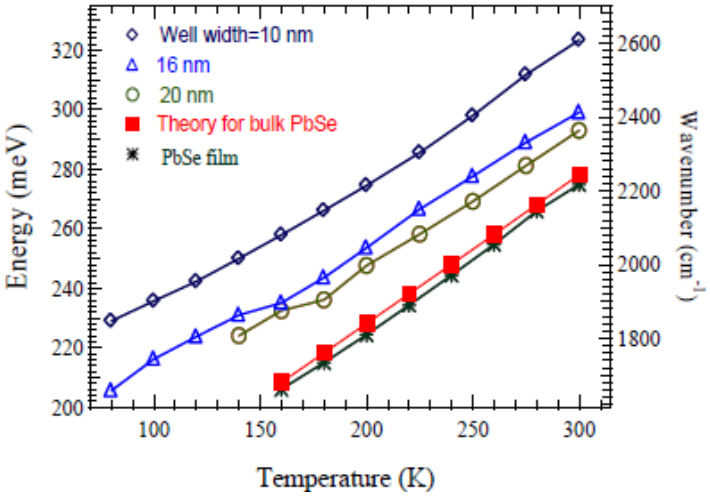

Fig. 5.4 Temperature dependant emission wavelengths of PbSe/PbSrSe QW structures (Adapted from Dewali's thesis, 2007)

The lead salts differ from the more usual semiconductors in their band structure as mentioned in the introduction. As an example, PbSe has a bandgap absorption at 4.6 μm and relative density of states masses of 0.3 and 0.34 for electrons and holes; the corresponding data for InSb are 6.9 μm, 0.014 and 0.4. While these III–V and IV–VI data are quite different, the effective temperature behavior of heterostructures does not differ too much regarding threshold carrier concentrations; the differences seem to cancel by and large when it comes to device characteristics. There is, however, one notable material difference of central importance to lasers: the non-radiative

recombination of carriers by the Auger effect is lower by two orders of magnitude in materials with the lead-salt band shape, as opposed to those with III–V band shape. This effect is strongly dependent on the band structure, grows with laser emission wavelength, and is the main reason why conventional diode lasers made from III–V heterostructures cannot compete with lead-salt lasers from longer than 3.5 μm wavelength onward.

Apart from these band shape related properties, the refractive index of the IV-VI materials is also important for the design of optoelectronic devices. In this point, the lead salts are somewhat special as well. On one hand, the relative static dielectric constant is very large, of the order of a few hundred. This results in a screening of imperfections that reduces free carrier scattering and thus increases carrier mobility; it also results in longer recombination lifetimes. This large dielectric constant makes infrared detectors comparatively slow, so that they do not play any role in military applications which are governed by II–VI detectors, and, increasingly, quantum-well devices. However, it does play a minor role for lasers. The infrared dielectric constant is quite high as well, as can be seen in **Fig. 5.5.** It follows the usual rule that an

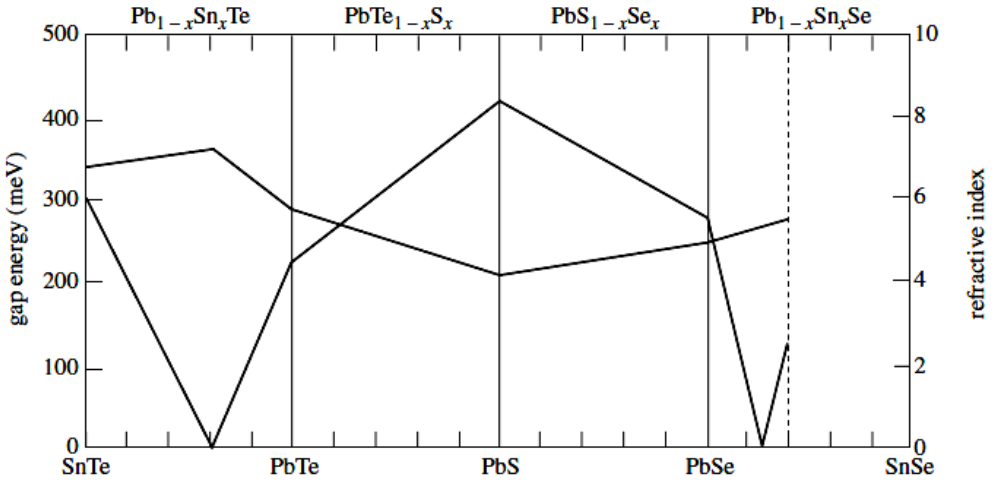

Fig. 5.5 The refractive index of lead-salt materials. Taken from Katzir *et al.*

increase in bandgap energy is connected to a decrease in dielectric constant. Hence one may combine all of these materials to form structures that at the same time confine the carriers and guide the infrared radiation. This is in accordance with the other optoelectronic semiconductor material families.

The lead salts have a comparatively low thermal conductance. This is a definite disadvantage for laser application because of their high heat dissipation and limits continuous wave (CW) operation temperatures, as compared with the much higher pulsed operation temperatures. The other material advantages, however, are so strong that no other heterostructure laser diodes can compete regarding maximum CW operation temperatures for wavelengths longer than 3.5 μm. One further concerning is the comparative softness of the Pb-salt materials which gives lead-salt devices less stability. On the other hand, the material properties are quite reproducible after a deformation. Hence the devices have inherent stability, and Pb-salt diode lasers have, for instance, successfully passed vibration tests for space-born applications.[11]

5.2.2 Application of Pb-Salt Lasers

The present lead-salt diode laser market is governed by the needs of gas analysis with highest demands regarding selectivity and sensitivity, and target molecules like N_2O, NO, NO_2, or hydrocarbons like HCHO, CH_4, C_2H_2, C_2H_4, C_2H_6, to name some from two chemical groups of interest. These can be detected by tunable diode laser spectroscopy with detection levels to below 100 ppt.

Typical requirements from such applications for lasers are as follows. The power should be larger than 100 μW in order to lift detector noise limits. The linewidth should be of the order of 10 MHz for the 10^{-6} resolution needed at reduced pressure (Doppler-) linewidth in order to reach optimum selectivity. Resolution and sensitivity

ask for laser power noise less than 10^{-6}, since the laser noise directly shows up in the detector signal. In order to trace the absorption of a single line, the emission wavelength must be stable to 10^{-6}. In order to scan lines well, fast tuning across a minimum of 10^{-5} is needed with low power modulation and constant low noise; larger variations would be good in order to allow simple multi-component measurement. In order to hit a specific absorption line, a larger tuning range is of course necessary; 1 cm^{-1} usually is considered to be sufficient.

The lead-salt diode lasers fulfill these requirements by and large. One would of course like higher operation temperatures than the present cryogenic ones. Additionally, toady's lead-salt lasers must be selected for single-mode operation near a target absorption line, and carefully tuned regarding current and temperature in order to run under appropriate conditions. Single-mode designs have been demonstrated with success, and technically their development would not pose any substantial problems, but up to date the limited gas analysis market has not allowed the corresponding investments. Lead-salt lasers fulfill the needs of high-performance gas analysis quite well; in a suitable system, they stay on line for years with reproducible performance, and have an impressive record of working under difficult conditions.

Gas analysis requirements as discussed above are met by the lasers fabricated today and selected for this purpose. For longer wavelengths, these are homostructure lasers; between 3 and 10 μm DH-lasers with mesa structure, buried waveguide or stripe contact lateral confinement are standard. While the stripe contact is, of course, the simplest lateral design and allows good production yields, it is well known to often produce laterally multi-lobed emission. The missing lateral carrier confinement gives rise to both ineffective injection and possible current density instability, the

latter being detrimental to high-resolution spectroscopy since it reduces reproducibility and increases the effective linewidth. Hence laboratory models often have lateral structures by growth of DH structures and subsequent mesa formation, or by growth of a single heterostructure (SH), a lateral etch process and subsequent epitaxial overgrowth of this then buried heterostructure (BH). These are the most common designs.

One quite obvious laser parameter for monitoring development success is the operation temperature. On one hand, the present cryogenic operation temperatures ask for unwanted investments in cooling equipment; these costs are reduced by allowing for higher temperatures. On the other hand, the larger the operation temperature range is, the larger the tuning range for a single laser device; this is helpful for detecting different molecules with the same laser. Most important for contemporary high-performance gas analysis equipment is CW (or at least quasi-CW) operation, since under pulsed conditions, the linewidth of laser emission is too large to resolve Doppler broadened absorption lines.

5.2.3 Trends of IV-VI Lasers

One objective for future IV-VI research is to find higher operation temperatures, with room-temperature or higher operation of course being the primary goal. Another is for higher emission power. Both of them probably cannot be met with the present selection of lead-salt laser structures and material combinations. One can expect further steady improvements, but no breakthrough by now, since the laser designs are optimized empirically without available models for Pb-salt lasers. So the question is where the limitations can be found? We shall concentrate on the output power, and discuss operation temperatures as we move along.

The efficiency of lead-salt lasers is usually of the order of one to a few per cent if operated in multimode emission. A general observation is that the smaller the cross-section, the lower the output power is. This effect runs opposite to the design for maximum operation temperature, where one tries to minimize the active volume thickness in order to obtain a high carrier concentration at constant current load. DH lasers with the same lateral structures reach higher operation temperatures with a thin active layer (as is standard), but get higher output power with a thick active region.

Typically, the total power of lead-salt diode lasers at standard operation temperatures is of the order of a few milliwatts per ampere in CW mode. One explanation for low external efficiencies is high internal loss. This is, however, quantitatively unreasonable at low temperatures, where the free carrier absorption is

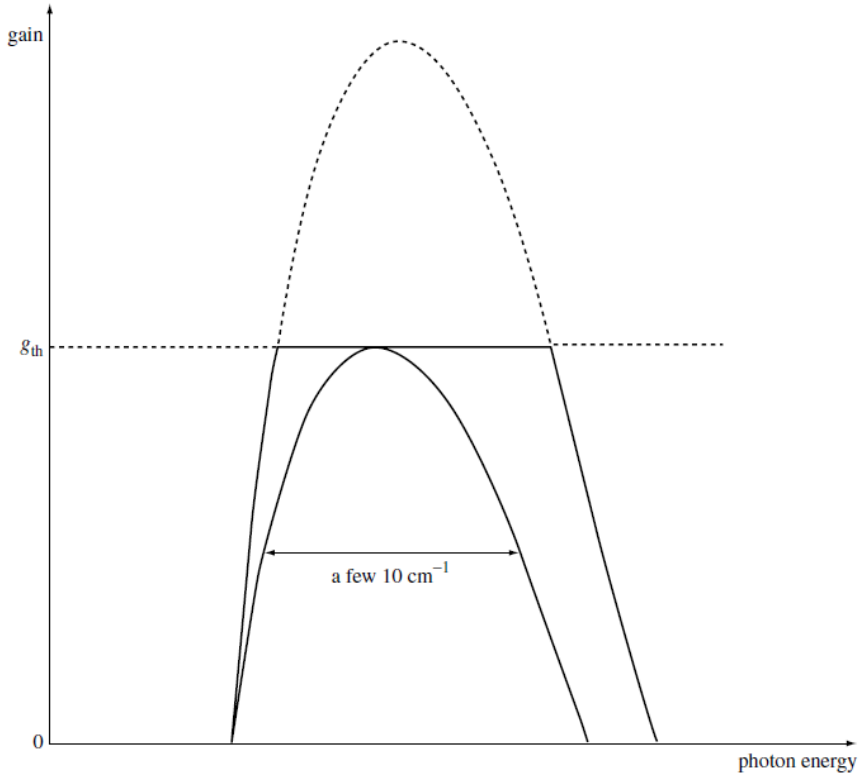

Fig. 5.6 The gain curve reaches threshold at a single point as the current is increased from zero. In this position, its half-width is of the order of the multimode wavelength band width (a few 10 cm^{-1}). The unsaturated gain, which reduced in maximum to a curve touching g_{th} at the mode positions (here symbolized by a flat line), would be much higher than g_{th} (broken line). Adapted from Tacke (2000).

lower than the equivalent loss due to resonator out coupling. Another explanation is saturation. Saturation is evidenced by the multimode operation of these lasers. Inhomogeneous broadening leads to spectral hole burning around the lasing mode, so that the gain curve is not clamped to its position at threshold, but rather touches the threshold gain for the whole multimode emission band width. This is shown schematically in **Fig. 5.6.** In order to reach this higher gain (especially at the multimode emission high-energy band edge), additional injected carrier concentration is necessary.

As stated above, improving the heat dissipation in the active region of Pb-salt lasers is urgently required for enhancing the performance of the laser operating at high temperature. In this research, we designed a way by removing growth substrate with the low thermal conductivity and replacing it for metal heat sink with high thermal conductivity. From the above mentioned points, this should increase the laser performance, in particular operation temperature significantly. The details of the experimental procedures are described and supporting data and figures are listed in this chapter.

5.3 Edge-Emitting Lasers on BaF_2 (110)

In this chapter, a lead salt mid-infrared laser sample grown by molecular-beam epitaxy (MBE) on a polished BaF_2 [110] substrate is studied. For improving the laser performance at higher operation temperature, a method of substrate transfer from a BaF_2 substrate to a copper heat sink is developed. The cleaved facet along the {100} plane, which is helpful for the formation of a Fabry-Pe′rot resonant cavity on the laser sample, is observed. Pulsed photoluminescence measurements are conducted on the

laser sample step by step during processing in order to trace the effect of each process step.

At the initial stage, lead salt laser structure on BaF_2 (110) were fabricated and examined, owing to the advantages mentioned in the previous section. In order to overcome the existing problems associated with the [100] orientation of the edge emitting devices, the [110]-orientation was then chosen. Compared with the conventional [100]-oriented materials, [110]-orientation provides higher material quality, high modal gain and partially lifts the degeneracy. Despite the low thermal conductivity of IV-VI semiconductor (thermal conductivity 4.2 $Wm^{-1}.K^{-1}$@300K for PbSe), proper design of a laser fabrication method on those substrates having higher thermal conductivity allows significant improvement in the laser operation temperature. A successful epitaxial transfer and cleaving of [110]-oriented IV-VI laser structure on copper substrate, which has almost 34 times higher thermal conductivity (401 $Wm^{-1}.K^{-1}$@298 K) than BaF_2 substrates (11.7 $Wm^{-1}.K^{-1}$ @300 K), was reported. This dissertation describes all my experimental work towards the development of lead-chalcogenide laser structures. The journey was full of challenges and the following chapters also describe how they were met and solved.

5.3.1 Motivation of This Research

Mid-infrared semiconductor lasers have been investigated extensively in recent years due to tremendous application requirements in both research as well as in industry. Most of the attraction has originated from the prospects for ultrahigh-sensitivity trace-gas sensing systems based on laser absorption spectroscopy.[19] Presently, the leading technologies for serving these applications are: III-V interband quantum cascade lasers, Sb-based type-II band alignment quantum well

semiconductor lasers, and IV-VI lead–salt semiconductor lasers.[20] [21] Compared with the other mentioned techniques, IV-VI lead salt lasers have obvious advantages such as large and easy current tuning capability, narrow spontaneous emission linewidth, and low Auger recombination rate, which are essential for mid-infrared gas sensing applications. Due to the existence of two parallel facets along the {100} plane to form a Fabry-Pe'rot resonant cavity, the lead salt diode laser structures are naturally fabricated on [100]-oriented lead salt substrates.

It has been demonstrated that [110] is the best orientation for lead salt laser performance.[22] Previous theoretical simulations[23]describe that the gain from [110]-

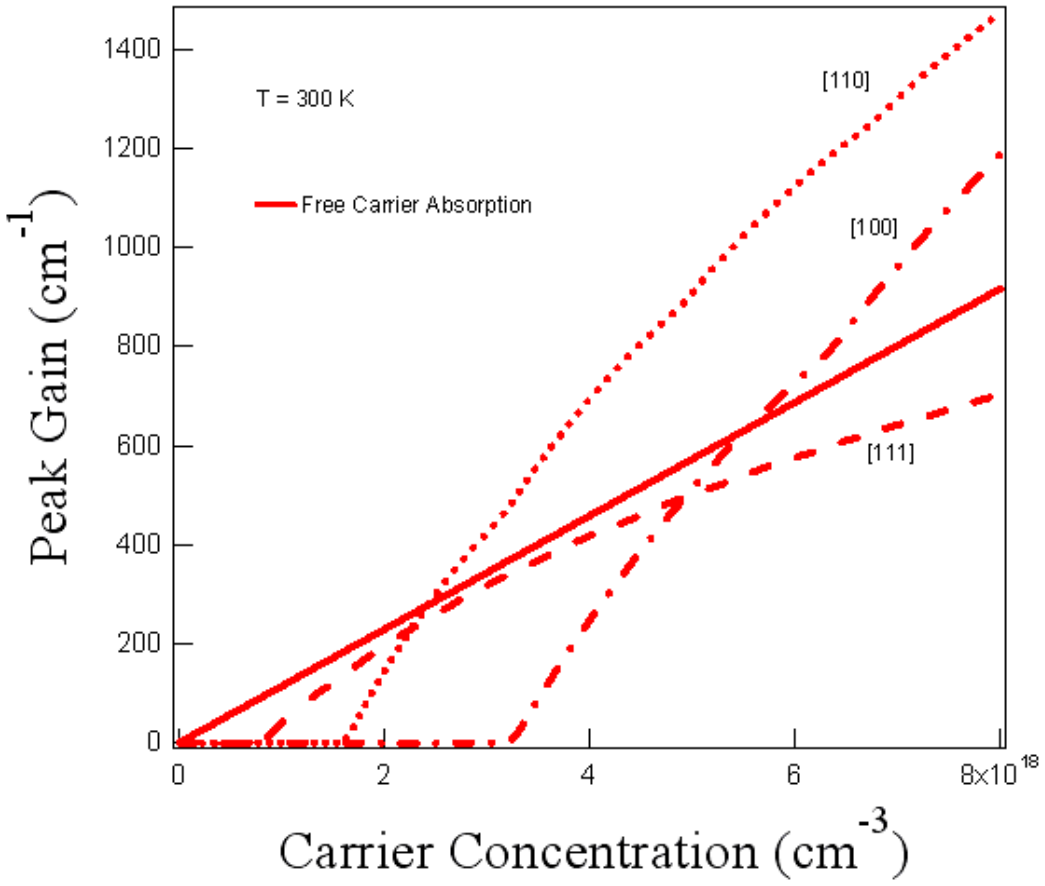

Fig. 5.7 Calculated peak gain for [111], [100] and [110] QW structure at different injected carrier concentrations at 300 K. The free carrier absorption (solid line) is shown as well. Taken from Shi (2004)

oriented lead salt quantum well structures is radically higher than that from [100]-oriented counterparts (**see Fig. 5.7**). Moreover, the maximum operation temperature of a [110]-oriented lead salt laser is 70 ^{0}C higher than that of a conventional [100]-oriented lead salt laser. In addition, two parallel cleavage facets can also be formed on [110]-oriented lead salt materials in order to fabricate a Febry-Pe'rot cavity.[24] Recently, our group has successfully demonstrated an electrically-pumped Pb-salt laser on the [110]-oriented PbSnSe substrate. In that report, the maximum achievable heat-sink temperature for the pulsed (40% duty cycle) laser emission at λ = 5.2 μm was 158 K as seen in **Fig. 5.8**.[25] The limitation in high-temperature operability of such lasers is mainly due to the low thermal conductivity of lead salt substrates.

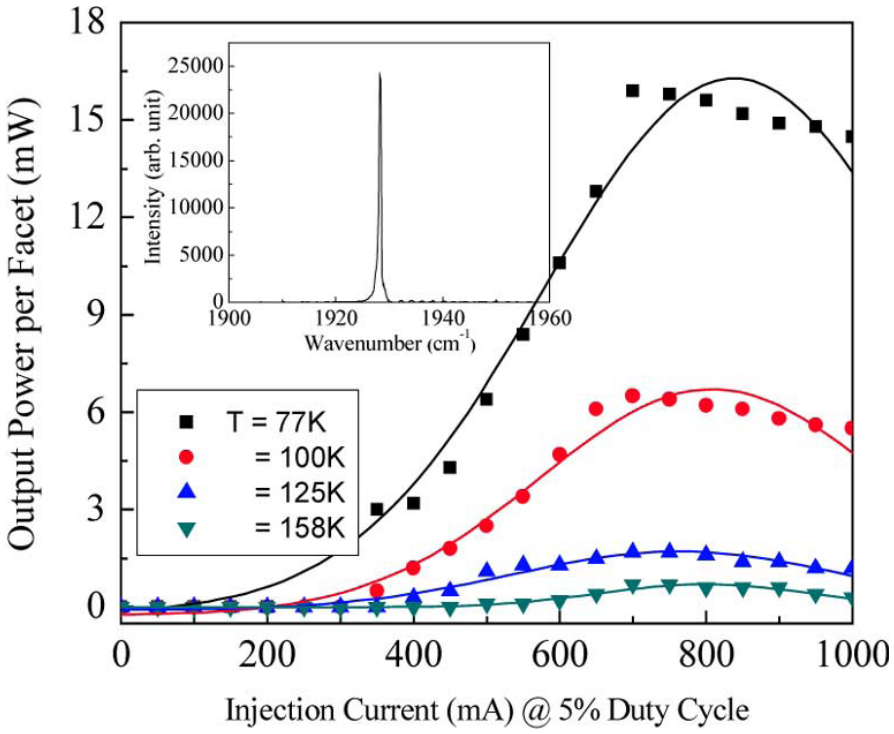

Fig. 5.8 Laser light output per facet versus injection current (L-I) at several heat-sink temperatures. Inset: Laser spectrum at 158 K. Taken from Mukherjee (2007).

Additional disadvantage for these substrates are their commercial unavailability and associated high expense. BaF_2, which is considered to be a widely accepted growth

substrate for lead salt epitaxial layers, is the best substrate suitable for lead salt lasers. The thermal conductivity of BaF_2 substrate (11.7 W/m K at 300 K) is six times higher than that of a lead salt substrate (1.8 W/m K at 300 K). Moreover, BaF_2 substrates are commercially available and thus less expensive than PbSnSe substrates. The lattice mismatch between BaF_2 and PbSe is only 0.6% at 300 K; therefore a successful lead salt epitaxial growth is obtained on BaF_2 substrates without producing any significant lattice strain. The ultimate goal of a lead salt laser fabricated on the [110]-oriented substrate is to achieve the high-temperature operation of mid-infrared lasers.

However, BaF_2 has a natural {111} cleavage plane, whereas the lead salt can be naturally cleaved along the {100} plane. The main challenge, therefore, lies in the formation of the cleaved facets on lead salt epilayers grown on a [110]-oriented BaF_2 substrate with a dissimilar cleavage plane. This necessitates the requirement of a novel bonding and cleaving mechanism for lead salt materials on BaF_2 substrates. The technology of transferring epitaxial layers together with removal of the growth substrate has already been developed for various material systems.[26] [27] [28] Despite successful transfer of lead salt epilayer on different substrates such as GaAs, [6] the limitation of high-temperature operation persists. This problem can be alleviated if one can use a substrate whose thermal conductivity is considerably higher than that of GaAs or lead salt. This is vastly important for the prospect of realizing mid-infrared optoelectronic devices with high output power because the loss in the form of Joule heating could be easily dissipated by the substrate.

A support membrane with high thermal-conductivity is urgently needed for this purpose, so, in recent, we proposed a novel bonding and cleaving mechanism which entails replacing a BaF_2 substrate with a copper heat sink. The thermal conductivity of the copper (401 W/m K at 300 K) is almost 34 times higher than that of BaF_2; this is

highly expected to improve the high-temperature emission characteristics for lead salt mid-infrared lasers significantly.

5.3.2 Experimental Procedure

5.3.2.1 Substrates Preparation

The first step towards the fabrication of [110]-oriented Pb-salt lasers on BaF_2 substrate is the development of surface preparation technology for [110]-oriented wafers for the epitaxial growth of IV-VI layers. Since (110) crystal facets are not the natural cleaving facets of BaF_2, {110} BaF_2 is obtained by cutting the crystal along [110]-orientation. Therefore, the surface of an unpolished substrate is so rough with surface defects and grooves. **Fig. 5.9** shows the SEM image of an unpolished {110} BaF_2 wafer, as bought from a commercial vendor.

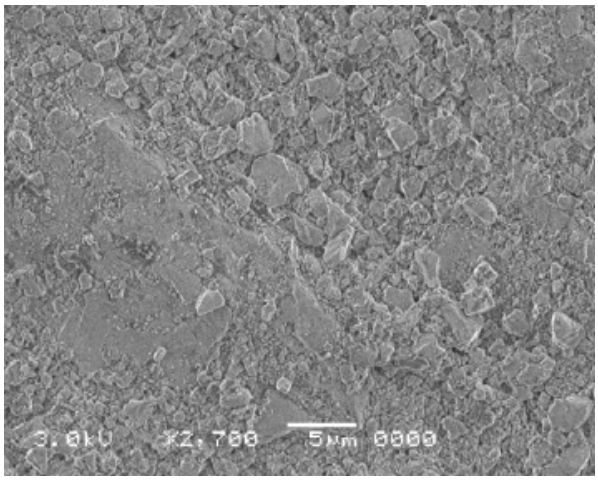

Fig. 5.9 SEM image of the surface of unpolished {110} BaF_2 wafer from a commercial vendor.

As we know, Polishing helps in achieving surface planarity, removes the surface roughness, and lowers the defect density on the surface. Epilayers grown on a polished substrate should have a much better quality and at the same time enables to be easily processed during the device fabrication therefore.

A novel chemical-mechanical-polishing (CMP) recipe was developed to make epi-ready [110]-oriented BaF_2 substrate for MBE growth. There were several challenges related to this process. Epi-ready BaF_2 substrates are not commercially available. Also up to date there is no report referable to polishing of [110]-oriented

BaF_2 wafers. Metal halides are not common materials for epitaxial growth; rather they have wide applications in IR windows. For these applications the surface flatness needed is not comparable to the flatness required for an epi-ready wafer. While developing a polishing recipe for {110} BaF_2 polishing, the biggest challenges was the extremely low Mohs' hardness value of BaF_2 crystal. Mohs' hardness is actually the physical property of a material that represents a materials resistance to scratching. And among all metal fluorides, BaF_2 has mush lower Mohs' hardness of 3 compared to diamond, which is the material available in nature having the maximum Mohs' hardness value of 10. Now all the abrasives and chemical slurries available in the market for CMP contain either Alumina (hardness: 9) or colloidal silica (hardness: 6 - 7) which are much harder than BaF_2. Therefore, commercially available slurry materials for CMP do not have the capacity to produce scratch-free surface of BaF_2, regardless of their particle size. In addition, most of the chemical polishing cloth was slightly harder and was found to scratch BaF_2. Therefore, a polishing method for BaF_2 that overcomes all these shortcomings needs to be developed. After a thorough research and rigorous experiments, a novel polishing recipe was developed by our research lab, which contains both mechanical and chemical material removal steps for BaF_2 wafer.

After a series of experiments, a novel polishing recipe was developed with three steps. The purpose of each step was described as following respectively: (1) reduction of surface roughness on back and front side of wafer with CMP-I (2) rough polishing with CMP-II (3) final chemical polishing with CMP-III. In the first step CMP-I is used as the polishing solution on a 1200 grit size SiC cloth till the substrate become transparent and blisters on the surface get removed. Nomarski image in **Fig. 5.10** shows the substrate surface after 17 minutes polishing with CMP-I recipe.

Once the substrate reaches the above stage, the next step is polishing with CMP-II until no scratches are visible under 50X magnification of the Nomarski Microscope. CMP-II is an alkaline solution containing high purity nano-abrasives. The cloth initially moistened by DI water and the polishing solution was added at a rate of 1.5 ml/min. The substrates were polished for 10 minutes and checked for scratches. After every run, the cloth was thoroughly flushed with DI water and the substrates were rinsed in DI water as well. Cleaning the cloth at regular interval with DI water is important as the silica particles in the polishing slurry solidify quickly in air-contact on the cloths thus causing deterioration of the cloth and the substrate surface. It can be seen in Fig. **5.11** that scratches become invisible at higher magnification (×50) of Nomarski Microscope after polishing 25 minutes with CMP-II.



Fig. 5.10 Nomarski image of substrate surface after 17 min polishing with CMP-I.

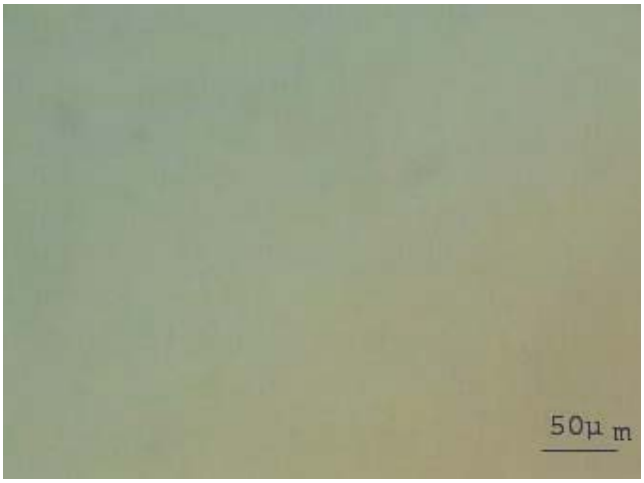

Fig. 5.11 Nomarski image of polished substrate surface after 25 minutes polishing with CMP-II.

The next stage involves final polishing using a purely chemical solution without any abrasive to attain a completely uniform surface without scratches under SEM observation. After polishing with the CMP-II, although a scratch-free surface was observed under Nomarski but the SEM images still showed light scratches and

roughness on the surface. **Fig. 5.12** shows the SEM image of the substrate after polishing with CMP-II for 25 minutes and before final polishing stage. It is observed from the above SEM that CMP-II was not sufficient to produce epi-ready surface. Therefore, final polishing was carried out using another fresh solution, CMP-III for 40 seconds. The cloth was initially moistened using the same solution and then the solution was added continuously at a rate of 1 ml/sec. **Fig. 5.13** shows the surface of the substrate without surface non-uniformity or any scratches after final polishing with this new solution. After all of the above polishing steps, we got an epi-ready BaF_2 substrate for laser structure growth.

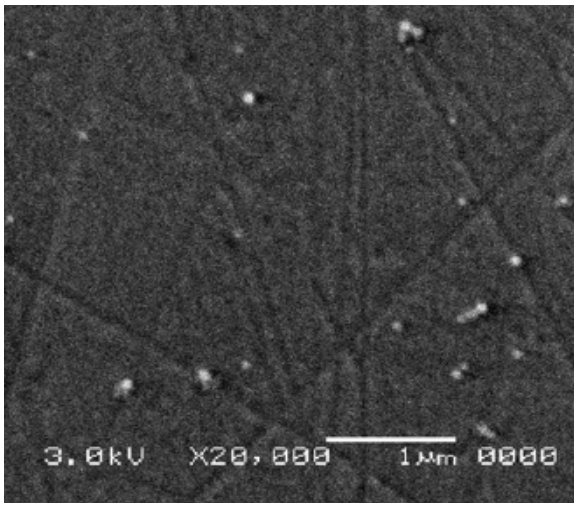

Fig 5.12 SEM image of the substrate surface polished with CMP-II.

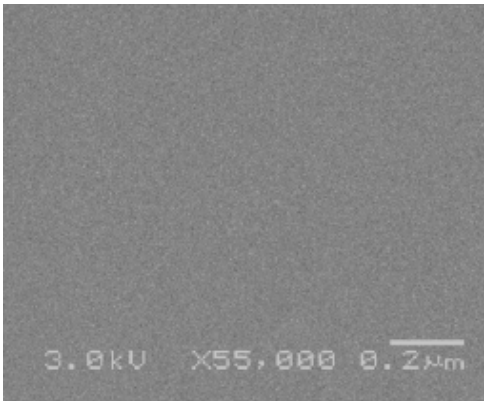

Fig. 5.13 SEM image of the substrate surface polished with CMP-III

5.3.2.2 MBE Growth

After polishing, the substrate was cleaned by acetone and proponal in ultrasonic bath and dried by using high-purity nitrogen gas. The substrate was inserted into the MBE chamber and out-gassed in buffer chamber at 200 ^{0}C for 4 hours. And then it was transferred to the main MBE chamber for structure growth, at this point, the second out-gassing was conducted at 500 ^{0}C for 30 minutes before growth. The

optically-pumped laser structure was consisted of a stack of PbSe/PbSrSe multiple quantum wells (MQWs), which was successfully epitaxially-grown on a polished [110]-oriented BaF_2 substrate by our MBE system.[29] The laser structure consisted of 13 pairs of PbSe/PbSrSe (20nm/30nm) and a top and bottom optical confinement layers of PbSrSe. During the MBE growth, a Se-to-PbSe beam flux ratio of 15% for PbSe and PbSrSe layers, a Sr-to-PbSe flux ratio of 3% for PbSrSe confinement layers and a ratio of 2.5% for PbSrSe barriers of multiple quantum well structures were maintained. The growth rate was controlled around 1.8 μm/hr, and the substrate temperature was held at 375 °C.

5.3.2.3 Processing after Growth

After the epilayer growth, the sample was cut along the surface to find [111]-oriented facets. The rectangular stripe patterns were formed on the laser samples by using a set of properly-designed masks, as shown in **Fig.5.14**. The stripe width in the mask varied between 20 μm and 50 μm, and the distance between the centers of two adjacent stripes varied from 200

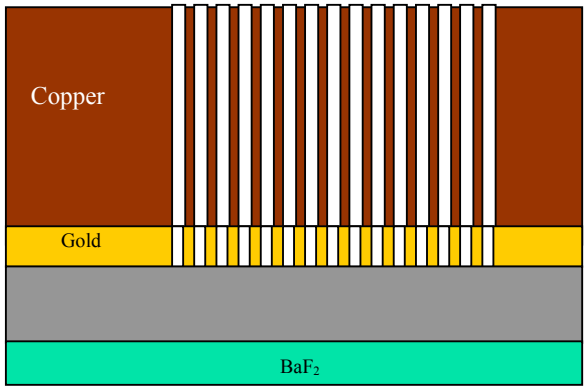

Fig. 5.14 Schematic of cross-section of copper pattern on the laser structure by electroplating

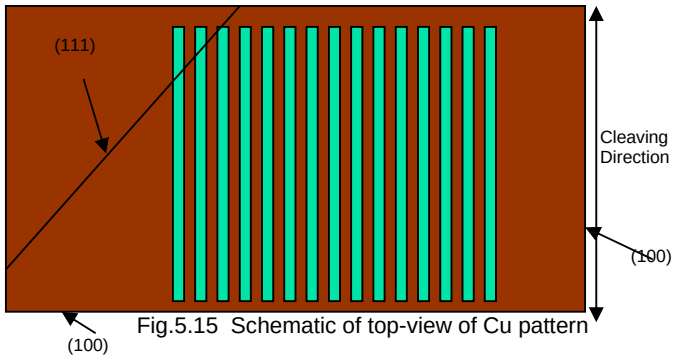

Fig.5.15 Schematic of top-view of Cu pattern

μm to 350 μm. In order to obtain [100] natural cleavage direction for PbSe crystal, the masks were placed on the sample surface with the rectangular stripe creating an angle of 54.7° with the [111]-orientation during the lithography processing as illustrated in **Fig. 5.15**. The lithography process was followed with gold electroplating (thickness ~1μm) on the striped laser patterns. Substrate (BaF_2) transfer was then accomplished by depositing copper on the gold-electroplated sample in order to achieve higher heat dissipation for continuous-wavelength (CW) operation of lasers. After the copper electroplating (thickness ~100μm), as illustrated in **Fig. 5.16**, the BaF_2 substrate was removed by thinning using CMP methods down to 50 μm and placing the entire sample in an acetic solution for purely chemical removal. When the substrate was fully removed, the laser sample was cleaned and then blown by high-purity nitrogen gas and reinserted into the MBE chamber for the

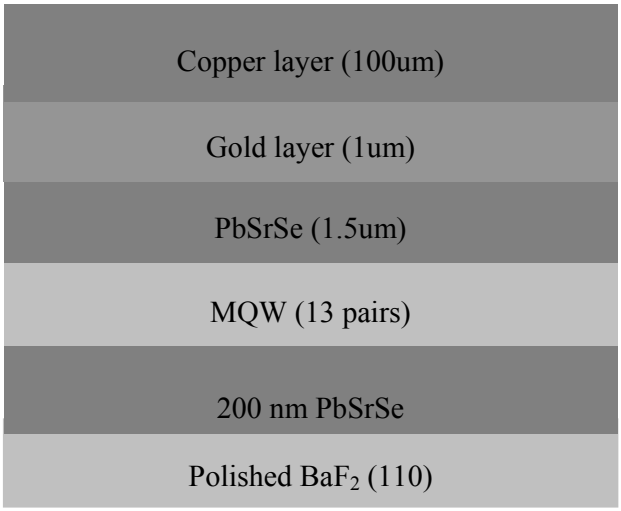

Fig. 5.16 Laser structure with gold and copper electroplating layers and BaF_2 substrate

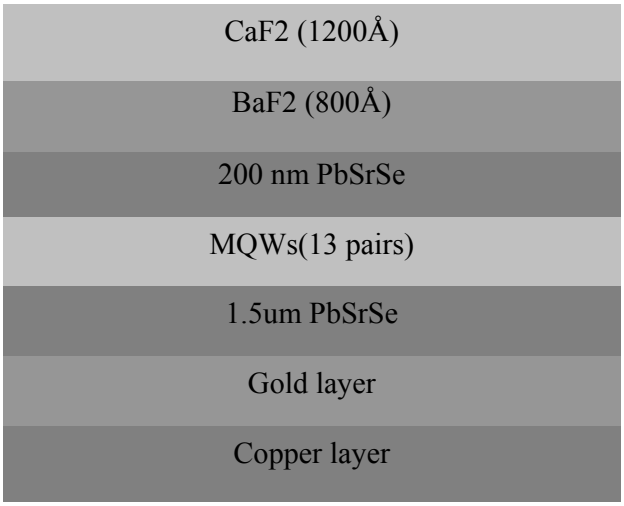

Fig. 5.17 Final laser structure with passivation and protection layers

second growth. Thin layers of BaF_2 (thickness ~ 800 Å) and CaF_2 (thickness ~ 1200 Å) were grown on top of the lead salt epilayers (initially covered by BaF_2 substrate) supported by the copper heat sink (see **Fig. 5.17**). BaF_2 and CaF_2 layers were grown with the purposes of providing surface passivation and protection.

5.3.3 Results and Discussion

As shown in **Fig. 5.18**, streaky reflection high-energy electron diffraction (RHEED) patterns were recorded from the epilayer soon after the first MBE growth of the epilayers on the BaF_2 substrate. Those patterns confirmed the two-dimensional nature of the lead salt epilayers grown on a [110]-oriented BaF_2 substrate. In order to study the influence of the processing steps on optical properties, pulsed photoluminescence (PL) was conducted using a 1064-nm neodymium: yttrium-aluminum-garnet (Nd: YAG) laser with a pulse-width τ_{pulse} of 30 ns and pulse repetition frequency of 10 Hz. For comparison, spontaneous emissions emanating from the sample were recorded at different processing stages. In **Fig. 5.19**, the black curve represents photoluminescence emissions from the backside of the laser sample initially grown in the MBE chamber; the red and blue curves in **Fig. 5.19** show photoluminescence emissions from the laser sample

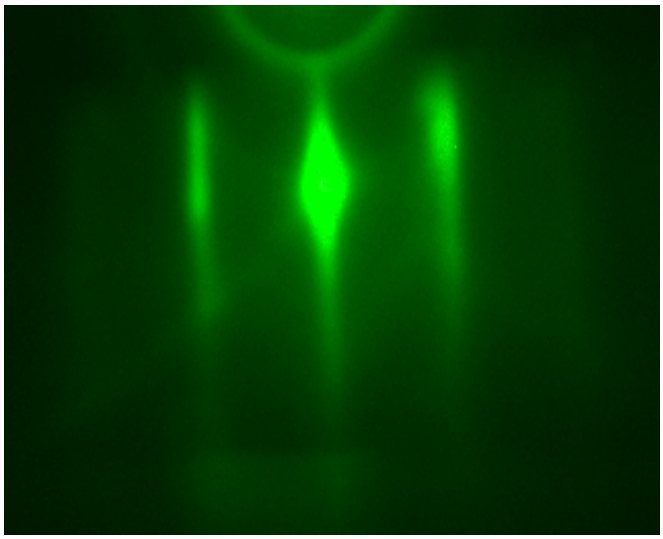

Fig.5.18 RHEED image in the [112] azimuth during growth of the PbSrSe layer at a temperature of 375^0C

after the copper electroplating and BaF_2 substrate removal, respectively. The linewidth of the photoluminescence intensity after the MBE growth was measured to be 146.56 cm^{-1}. After the copper electroplating and subsequent BaF_2 removal, the linewidths were calculated to be 177.42 cm^{-1} and 180.38 cm^{-1}, respectively. However,

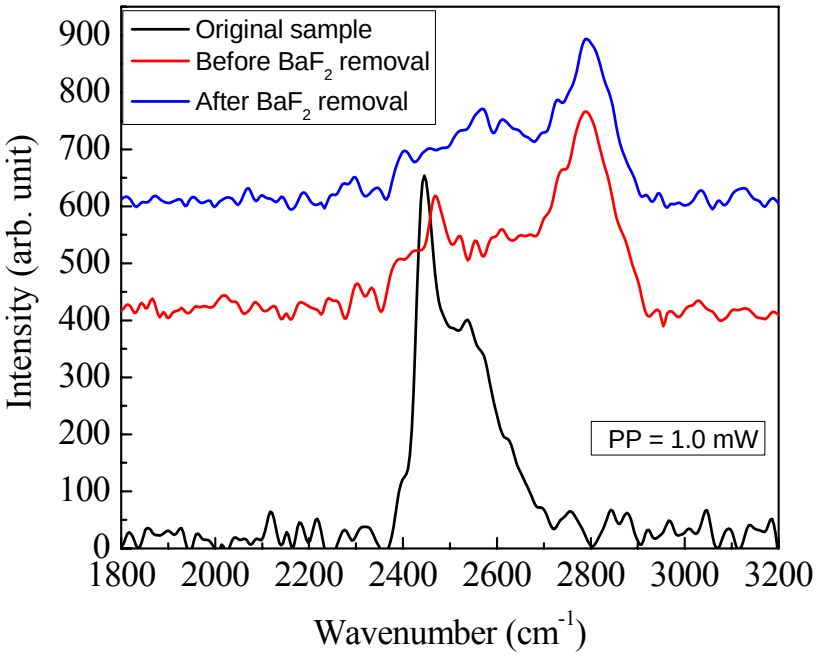

Fig. 5.19 Photoluminescence spectra at room temperature of laser sample right after growth, plating copper and removing BaF_2

the photoluminescence intensity in the two aforementioned cases reduced by a factor of 1.8 and 2.2 times respectively. Thus the entire spontaneous emission power, calculated by taking the area of the spontaneous emission into account, remained almost constant for all three cases. We assume that the initial stress release and redistribution might have caused the increase of the photoluminescence linewidth during metal electroplating and substrate removal. This together with interface traps generated during the sample processing was thought to be the cause of reduction of the photoluminescence intensity.[30] The formation of a cleaved facet along the [100]-

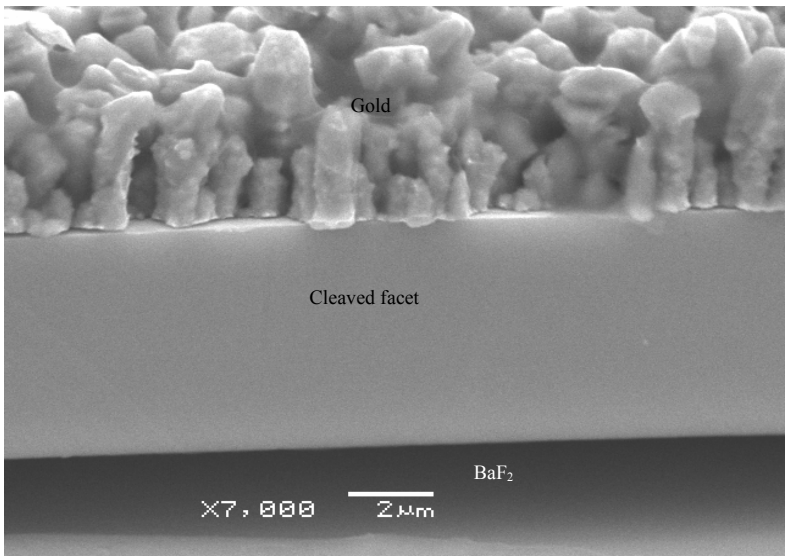

Fig. 5.20 SEM image of cleaved epilayer with gold and copper support layers

orientation on the laser structure, as shown in **Fig. 5.20**, was an indication of our successful growth and processing of the laser sample.

5.3.4 Summary of Transferring Technology

Using specially-designed masks and alignment tools, we successfully transferred a [110]-oriented Pb-salt laser structure grown on a BaF_2 substrate to a copper heat sink. Two parallel cleaved facets were formed to achieve laser oscillation. We expect that the laser performance will be significantly enhanced by using the copper heat sink in conjunction with the smooth {100} cleaved facets. The measurement on this laser sample is still ongoing and the results will be provided in the near future.

5.4 References

[1] I. Melngailis, *Appl. Phys. Lett.* **2**, 176 (1963)

[2] J. Phelan, A.R. Calawa, R.H. Rideker, R.J. Keyes, B. Lax, *Appl. Phys. Lett*. **5**, 75 (1964).

[3] J. F. Butler, A. R. Calawa, R. J. Phelan, T. C. Harman, A. J. Strauss, R. H.Rediker, *Appl. Phys. Lett*. **5**, 75 (1964).

[4] D. L. Patin, C. M. Trush, *Appl Phys. Lett.* **45**, 193 (1984).

[5] A. Joullie, P. Christol, A. N. Barnov, A. Vicet, Solid-State Mid-Infrared Laser Sources, edited by I. T. Sorokina, K.L. Vodopyanov, (Springer-Verlag, Berlin, Heidelberg, New York 2003).

[6] A.N. Baranov, T. N. Danilova, B. E. Dzhurtanov, A. N. Imenkov, S. G. Konnikov, A.M. Litvak, V. E. Umanskii, Yu. P. Yakovlev, *Phys. Lett.* **14**, 727 (1988).

[7] A. Joullie, P. Christol, A.N. Barnov and A. Vicet, Berlin, Germany: Springer-Verlag, **89** 1-59 (2003).

[8] C. L. Canedy, W. W. Bewley, J. R. Lindle, I. Vurgaftman, C.S. Kim, M. Kim, And J. R. Meyer *Appl. Phys. Lett*., **86**, 211105 (2005)

[9] M. Troccoli, D. Bour, S. Corzine, G. Höfler, A. Tandon, and D. Mars, D. J. Smith, L. Diehl and F. Capasso, *Appl Phys. Lett*., **85**, 5842 (2004).

[10] D.L. Partin , *IEEE Journal of Quantum Electronics*, **24**, 1716 (1988).

[11] Tacke, M. Philosophical Transactions of the Royal Society of London, Series A: Mathematical, Physical and Engineering Sciences, **359**, 547(2001).

[12] Z. Feit,M. McDonald, R. J. Woods, V. Archambault, and P. Mak, *Appl. Phys. Lett*. **68**, 738 (1996).

[13] U. P. Schiessl and J. Rohr, *Infrared Phys. Technol.* **40**, 325 (1999).

[14] Laser Focus World, Jan. **9** (1997).

[15] Hong H. Lee, *IEEE J. Quantum Electron*, **29**, 2619(1993)

[16] P. C. Findlay, C. R. Pidgeon, R. Kotitschke, A. Hollingworth, and B. N. Murdin, C. J. G. M. Langerak and A. F. G. van der Meer, C. M. Ciesla, J. Oswald and A. Homer, G. Springholz and G. Bauer, *Phys. Rev.* B **58**, 12908 (1998).

[17] J. R. Meyer, C. L. Felix, W. W. Bewley, I. Vurgaftman, E. H. Aifer, L. J. Olafsen, J. R. Lindle, C. A. Hoffman, M.-J. Yang, B. R. Bennett, B. V. Shanabrook, H. Lee, C. H. Lin, S. S. Pei, and R.H. Miles, *Appl. Phys. Lett.* **73**, 2857 (1998).

[18] I. S. Averyanov, N. P. Markina, F. P. Volkova, G. P. Pertsev, S. P. Chashchin, *Neorganicheskie Materialy* **4**, 825(1968).

[19] M. Tacke, *Infrared Phys. Technol.* **36**, 447 (1995).

[20] C. L. Canedy, W. W. Bewley, J. R. Lindle, I. Vurgaftman, C. S. Kim, M. Kim, and J. R. Meyer, *Appl. Phys. Lett.* **86**, 211105 (2005).

[21] M. Troccoli, D. Bour, S. Corzine, G. Höfler, A. Tandon, D. Mars, D.J. Smith, L. Diehl, and F. Capasso, *Appl. Phys. Lett.* **85**, 5842 (2004).

[22] Z. Shi, X. Lv, F. Zhao, A. Majumdar, D. Ray, R. Singh, and X. J. Yan, *Appl. Phys. Lett.* **85**, 2999 (2004).

[23] X. Lu and Z. Shi, *IEEE J. Quantum Electron.* **41**, 308 (2005).

[24] D. Ray, S. Bondili, S. Jain, D. Li, F. Zhao, A. Majumdar, Z. Guan, and Z. Shi, *IEEE Photon. Tech. Lett.* **18**, 373 (2006).

[25] S. Mukherjee, D. Li, D. Ray, F. Zhao, S. L. Elizondo, S. Jain, J. Ma, and Z. Shi, *IEEE Photon. Technol. Lett*. **20**, 629 (2008).

[26] E. Yablonovitch, T. Gmitter, J. P. Harbison, and R. Bhat, *Appl. Phys. Lett*. **51**, 2222 (1987).

[27] D. W. McAlister, P. J. McCann, H. Z. Wu, and X. M. Fang, *IEEE Photon. Technol. Lett.* **12**, 22 (2000).

[28] H. Z. Wu, X. M. Fang, R. Salas, D. McAlister, and P. J. McCann, *Thin Solid Films* **352**, 277 (1999).

[29] F. Zhao, X. Lv, J. Keay, D. Ray, R. Singh, A. Majumdar, X. Yan, and Z. Shi, *J. Cryst. Growth* **285**, 54 (2005).

[30] Michio Tajima, Haruhiko Yoshida, Shigeo Ibuka and Seigo Kishino, *Jpn. J. Appl. Phys*. **42**, L429 (2003).

Chapter Six

Summary and Future Work

6.1 Summary

The research described by this dissertation has focused on the IV-VI lead-salt semiconductors growth and characterization for mid-infrared device applications. Several novel approaches that have not been reported previously were developed in this dissertation. The ultimate goal is to develop a high-performance mid-infrared detector and lasers for civil and military application. Processing techniques and procedures, as well as theoretical design and calculations have been successfully developed, which could lead to high-temperature CW laser and high-sensitivity detector operation.

This dissertation includes six chapters. Chapter One introduced the primary properties of the IV-VI semiconductors and their applications. Chapter Two focused on the investigation of the growth defects in Pb-salt epilayers. In this chapter, the growth pits in IV-VI semiconductors were studied thoroughly in shape, size and density. Nomarski and SEM images were provided to verify the properties of the growth pits in order to deeply understand the origin of the growth defects in Pb-salt epilayers.[1] Chapter Three described the *in-situ* surface treatment procedure, which was carried out during MBE-grown PbSe on CaF_2/Si (111) heterostructure. The details of the experimental procedures were given step by step and supported by RHEED patterns. The promising results were listed in form of the improved electrical and optical performance of the epilayers.[2] Chapter Four discussed fabrication and characterization of a single element PbSnSe detector grown on Si(111) substrates. The details of the growth and processing were addressed based on structure, doping, etching, etc. Current-voltage curves were provided to verify the performance and properties of the P-N junctions and the issues related to the performance and fabrication were addressed too. Chapter Five presented the fabrication of the edge-emitting laser structure grown on a polished (110)-oriented

BaF_2 substrate. The details of fabricating procedures were addressed and fabrication issues have been discussed according to the intensity and linewidth of the photoluminescence (PL). By using electroplating technique, a metal base was formed in contact with epitaxial layer and was followed by a growth substrate removal for complete transfer of the epitaxial layer to the metal membrane.[3] Chapter Six detailed the future direction for this project and explains the issues needing further investigation and improvements.

6.2 Recommendations for Future Work

In this dissertation, a preliminary study on growth defects in IV-VI epilayers has been carried out, but most of details still need to be further investigated and verified. Besides the growth pits and etch pits, other defects related to material quality could be studied as well. Also the formation mechanism of each kind of defects could be studied and at the same time the ways of controlling the evolution of defects would be come out. The final purpose of this study is to reduce defects in Pb-salt epilayers.

The in-situ surface treatment method has been demonstrated in Chapter Three. Although the results are promising and encouraging, evidences are still required to support the experimental data. For instant, we have claimed that the growth has been conducted layer by layer and several single atomic layers have been formed, this is, however, pure speculation, which needs the experimental support by RHEED oscillation or other characterization methods.

Mid-infrared lasers and single element detectors have been fabricated in our research group, but their performances still need to be enhanced. Single element mid-infrared detectors grown on Si substrate have been tested on I-V characteristic, as mentioned in Chapter Four, in reverse bias, their leakage current is still too high

compared to their II-VI and III-V counterparts, so the material quality and fabrication techniques for IV-VI detectors have to be improved urgently in the near future.

6.3 Conclusion

Up to date, lead chalcogenides have been known for more than a century. Unfortunately, they have been left out of the mainstream research in recent years. The modern epitaxial technologies that allow high-quality alternative material growth and advanced device concepts have made a revitalization of IV-VI mid-IR optoelectronic devices. High-performance and –efficiency Pb-salt lasers and detectors have been made by several research groups in the world. Nevertheless, the challenges still exist, in particular, the material quality of IV-VI semiconductor needs to be further improved. At present, continuously reducing dislocations in Pb-salt epilayer is a key step towards successful fabrication of IV-VI mid-infrared optoelectronic devices on various substrates. Moreover, optimizing the fabrication technologies is also an essential way to high-performance device preparation.

Throughout this research, several novel processes have been developed. All the developed techniques are generic and can be applied to most of Pb-salt materials. However the challenges, which are not met yet and further experiments that are recommended in the previous section, present opportunities for ongoing research.

Conclusively, the work presented in this dissertation is promising and makes a step ahead towards the compact mid-infrared optoelectronic devices. Such devices will eventually lead to many applications such as high-efficiency CW tunable laser and fast-response high-detectivity FPA detector systems.

6.4 References

[1] J. Ma, D. Li, G. Bi, F. Zhao,S. Elizondo, S. Mukherjee and Z. Shi, *J. Electron. Mater*. **38** 325 (2009).

[2] D. Li, J. Ma, S. Mukherjee, B. Gang, F. Zhao, S. L. Elizondo and Z. Shi, *J. Crystal Growth*, **311**, 3395 (2009).

[3] D. Li, S. Mukherjee, J. Ma, G. Bi, D. Ray, F. Zhao, S. L. Elizondo, G. Yu and Z. Shi, *J. Electron. Mater.*, online first (2009).